Catalyst development for electro-catalysis of carbon dioxide reduction

二酸化炭素の電気化学還元触媒の開発

Wenhang Wang

王 文行

Supervisor: Prof. Noritatsu Tsubaki

Tsubaki Laboratory

Graduate School of Science and Engineering

University of Toyama

Preface

Carbon emissions have aroused tremendous environmental problems, such as global warming, ocean acidification, climate change, and so on. Carbon dioxide (CO_2) is the most important greenhouse gas. Its concentration of atmospheric exceeded 400 ppm from 2016, which added to concerns about the immense potential scale of economic, social, and ecological damages. Therefore, the development of strategies and technologies to effectively reduce CO_2 emissions has attracted great attention. The different proposed technologies follow one of two major approaches: to capture and geologically sequestrate CO_2, or to convert CO_2 into chemicals and fuels. The chemical conversion and utilization of CO_2 into high value−added chemicals and fuels are a more attractive and promising solution. Among all of the chemical conversion routes including thermal/electro/photo-catalytic strategies, the electrochemical CO_2 reduction reaction (CRR) into value−added chemical feedstocks offers a sustainable route toward carbon−neutral in the future due to its ambient operating temperature and pressure, and its effective control of the target product through adjustment of the applied potential. Especially, electricity can be generated from renewable energy sources such as solar and wind energies. It is reasonable to believe that the price of electricity by renewable energy is lower and lower with the continuous development of renewable energy technology in the future.

Many heterogeneous catalysts have been developed for the clean, efficient transformation of CO_2 to high value-added products to date, based on a multiple-electron transfer mechanism involving transfer of 2, 6, 8, or 12 electrons, such as carbon monoxide (CO), methane (CH_4), formate, and C_2 products (*i.e.*, ethylene and ethanol), that of them are the most important building block in chemical industry, and possess a large market. In general, the catalysts currently being employed are still not active enough and have insufficient catalytic selectivity and stability. This is attributed to that CO_2 is a thermodynamically stable molecule with low reactivity. CO_2 activation has to overcome a high barrier, and the chemical utilization of CO_2 constitutes a significant

challenge. The other hand, the reaction mechanisms are still under debate. So, these problems urge us to investigate the CO_2 conversion and develop high efficiency electrocatalyst.

Currently, copper is still the main metal that can effectively catalyze CRR to C_2 products, owing to the specific binding energy of *CO intermediate. Among all the copper−based catalysts, Cu_2O is considered optimal due to its better selectivity towards C−C coupling which is attributed to its controllable defects, morphology and so on. In Chapter 1, Cu_2O nanoparticles with rough surface and abundant oxygen vacancies were facilely prepared by using an ionic liquid, [Omim]Cl (1-octyl-3-methylimidazolium chloride), as a bifunctional structure-directing agent, where the $[Omim]^+$ played a role of surfactant to adjust the morphology of Cu_2O and the Cl^- facilitated the formation of oxygen vacancies by coordination with Cu^+. The obtained Cu_2O nanoparticles were further dispersed on the home-made graphite nanosheets to fabricate a composite catalyst. By adjusting the content of [Omim]Cl, the optimum catalyst of Cu_2O/ILGS-*400* performed the best performance with a faradic efficiency (FE) of 62.4% for C_2 products (ethylene and ethanol) with 0.1 M $KHCO_3$ as electrolyte at -1.15 V (*vs.* RHE) in an H-cell. To overcome the low current density of CRR in the H cell, a home-made flow cell was established to enhance the mass transport of CO_2. An excellent catalytic performance with high FE of C_2 (78.5 ± 2%) and commercial-level current density (123.1 mA cm^{-2}) at −1.1 V (*vs.* RHE) for 100 h in a flow cell. *In-situ* surface-enhanced Raman spectroscopy and density functional theory (DFT) computations proved the special structure of Cu_2O strengthened the adsorption of intermediates ($CO_2^{\bullet-}$, CO*) and the following C–C coupling reaction, thus remarkably promoting the formation of C_2 products. This work affords a novel strategy to synthesize metal oxide with controllable morphology and defects for electrochemical applications.

Among commodity chemicals, formate is noted for its nontoxicity, safety, transportability, and broad applications, which is also a hydrogen carrier for transportation. From CRR to formate is also a superior pathway, which has been investigated due to high selectivity. However, the double high index of current density

and FE in CRR is a great challenge. In Chapter 2, carburized indium oxide nanorods (In_2O_3-C) was synthesized by pyrolysis of MOFs precursor [MIL-68 (In)]. The electronic structure of In was regulated and the localization of negative charges was increased on the surface of In_2O_3-C catalyst, resulting in high FE of 97.2% at -1.0 V *vs.* RHE and above 90% in a wide potential range of 500 mV using the H cell. Furthermore, it reached a current density of -1.0 $A \cdot cm^{-2}$ in the flow cell for producing formate efficiently. The carbon atoms embedded into the In_2O_3 lattice were able to regulate the electronic structure of In and increased the localization of negative charges on the surface of In_2O_3, resulting in enhanced activity and selectivity simultaneously for CRR to formate. The whole reaction path from CO_2 to formate on In_2O_3-C was investigated by DFT computations, *in-situ* attenuated total reflection surface-enhanced infrared adsorption spectroscopy and 2D/3D surface-enhanced Raman spectroscopy. This work gives new light on developing high-performance CRR catalysts with high selectivity under large current density.

Therefore, two new electro-catalysts were designed, synthesized and applied to CRR, which exhibited the excellent performance about ethylene, ethanol, and formate. And a preliminary study is made with these catalysts in the ampere-level current state. The development of high efficiency electro-catalysts provided a new view in identifying the active sites and the pathways to the low carbon products for CRR.

Contents

Chapter 1

Joint Tuning the Morphology and Oxygen Vacancy of Cu_2O by Ionic Liquid Enables High-Efficient CO_2 Reduction to C_2 Products

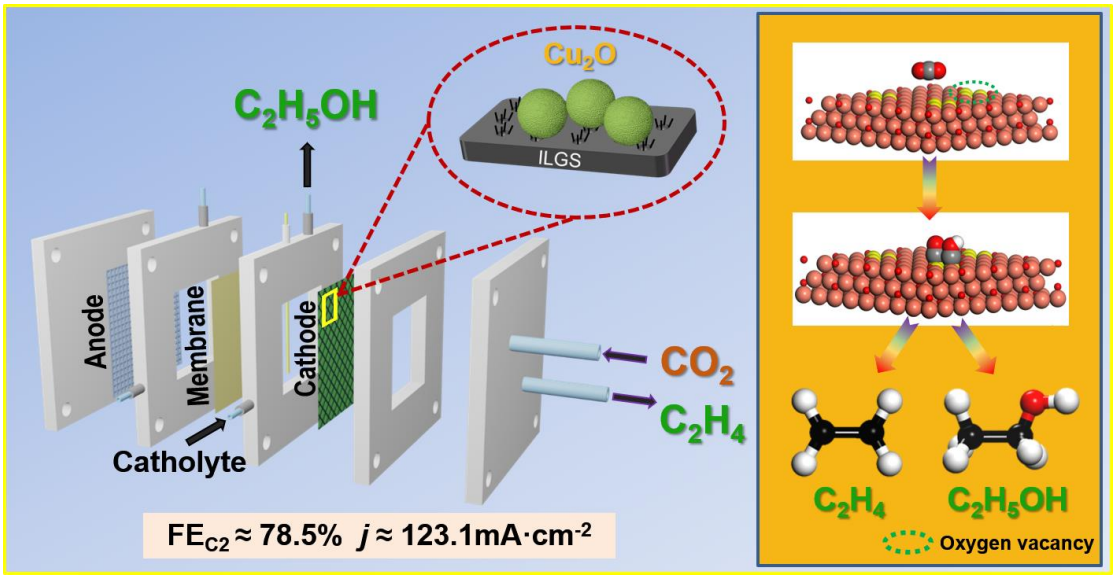

Ionic liquid assisted Cu_2O with rough surface and abundant oxygen vacancies boosts high-efficient CO_2 electroreduction to C_2 products.

Abstract

The electrochemical CO_2 reduction to multi-carbon products is a promising way for tackling carbon emissions and restoring renewable electricity, which still lacks of efficient electrocatalysts. In this Chapter, Cu_2O nanoparticles with rough surface and abundant oxygen vacancies were facilely prepared by using an ionic liquid, [Omim]Cl (1-octyl-3-methylimidazolium chloride), as a bifunctional structure-directing agent, where the $[Omim]^+$ played a role of surfactant to adjust the morphology of Cu_2O and the Cl^- facilitated the formation of oxygen vacancies by coordination with Cu^+. The obtained Cu_2O nanoparticles were further dispersed on the home-made graphite nanosheets to fabricate a composite catalyst, which showed an excellent catalytic performance with high faradaic efficiency of C_2 (78.5 ± 2%) and commercial-level current density (123.1 mA cm^{-2}) at −1.1 V *vs.* RHE for 100 h in a flow cell. *In situ* surface-enhanced Raman spectroscopy and density functional theory calculations proved the special structure of Cu_2O strengthened the adsorption of intermediates ($CO_2^{\bullet-}$, CO*) and the following C–C coupling reaction, thus remarkably promoting the formation of C_2 products. This work affords a novel strategy to synthesize metal oxide with controllable morphology and defects for electrochemical applications.

Keyword: CO_2 electroreduction; Ionic liquid; Cuprous oxide; Oxygen vacancy

1.1 Introduction

The carbon dioxide (CO_2) as an abundant and significant C_1 source has attracted widespread attention because of the resulted environmental deterioration problem from its excessive emissions [1-3]. The electrochemical CO_2 reduction reaction (CRR) is a clean and effective way for producing value-added chemicals or fuels, where electricity comes from solar or wind energy [4, 5]. Recent progress in CRR has been made to improve activity from CO_2 to C_1 and C_2 products such as carbon monoxide (CO) [6, 7], methane (CH_4) [8], formate[9, 10], ethylene (C_2H_4) [11] and ethanol (C_2H_5OH)[12, 13].

For the C_2 products, Cu-based materials have been evidenced unique electrocatalytic performances [14, 15]. Many strategies were developed to improve their performance towards C_2 products, including adjusting the morphology [16], alloying with other metals [17], doping with non-mental elements [18] and modifying with molecules [19]. Among them, oxide-derived copper (OD-Cu) stands out with its higher selectivity towards C_2 products, which is attributed to its controllable defects, morphology and so on [20].

Some recent works have been reported that the existence of halide ions (Cl^-, Br^- and so on) could improve oxygen vacancies concentration. Jin et al. reported a series of Ni/V composites via an *in-situ* growth strategy with NaCl as regulator. The concentration of oxygen vacancies increased due to the introduction of NaCl [21]. Chen et al. demonstrated that Br^- was able to boost and stabilize the oxygen vacancies on the (001) facet of Bi_2MoO_6 [22]. Lin et al. found that more defects (oxygen vacancies) of ZnO could be created by using a iodine-modified method [23]. All the above works have shown that the generation of oxygen vacancies on the surface of materials is feasible with halide ions. However, it is still lack of efficient methods to adjust the oxygen vacancies on OD-Cu for high-efficient electrochemical reduction of CO_2 to C_2 products.

The morphology also plays a key role on CRR performance. Therefore, several methods including hydrothermal, calcination, electrodeposition have been exploited to

control the morphology of OD-Cu catalysts, such as hydrothermal, calcination, electrodeposition [24, 25]. However, it is difficult to regulate the catalyst morphology and oxygen vacancy simultaneously. Ionic liquid (IL) is a kind of special compound consisting of the organic/inorganic cation and inorganic anion moieties. Meanwhile, the types of cations and anions in ILs can be flexibly designed to realize diverse properties such as tunable chemistry, hydrogen bond interactions, as well as good stability. Therefore, it has attracted widespread research interests to use ILs for regulating the morphology, composition and intermolecular interaction of various materials [26-28]. Inspired by above works, the halogen-containing ionic liquid should be possible realized to regulate the morphology and oxygen vacancy of OD-Cu systematically, which however has yet been reported.

In this work, a typical halogen-containing IL, 1-octyl-3-methylimidazolium chloride ([Omim]Cl), was used to tailor the morphology and oxygen vacancy of Cu_2O by a precipitation method at room temperature. With the assistance of $[Omim]^+$, a quasi-spherical Cu_2O with rough surface was obtained. Simultaneously, more oxygen vacancies were created on the surface of Cu_2O with more Cl^- surrounding Cu^+. Under the joint action of rough surface and oxygen vacancies, an excellent performance towards C_2 products was achieved in a flow cell. The correlated effects of morphology and oxygen vacancies in electrocatalytic CO_2 to C_2 on OD-Cu were also unveiled in this work.

1.2 Experiment

1.2.1 Materials

All chemicals and reagents were purchased from Sinopharm Chemical Reagent Co., Ltd. unless otherwise specified. Nafion N-117 membranes (0.180 mm thick, ≥0.90 meq/g exchange capacity) were provided from Alfa Aesar China Co., Ltd. High purity graphite rod (ø = 3 mm) was purchased from Beijing Crystal Dragon Carbon Technology Co., Ltd. 1-octyl-3-methylimidazolium chloride ([Omim]Cl, 99.0%) was

obtained from the Centre of Green Chemistry and Catalysis, LICP, CAS, P. R. China. The water in all experiments was purified by a Millipore system. All the gases used are high purity gases, such as high purity Ar (99.999%), high purity N_2 (99.999%) and high purity CO_2 (99.999%).

1.2.2 Catalysts Synthesis

In order to make the as-made Cu_2O disperse better, we firstly synthesized an ionic liquid functionalized graphite sheets (ILGS) as an inert carrier according to our previous method, which has been proved no activity for CRR [29]. Then, ILGS of 20 mg was dispersed into water of 20 mL under ultrasonic for 30 min. The suspension was sequentially added in 0.1 mol/L $CuCl_2$ of 6 mL and stirred for 30 min. After that, 0.6 mol/L NaOH of 9 mL was slowly added under continuous stirring for another 10 min to get solution A. Then, a certain volume of [Omim]Cl was added into solution A and stirred for 10 min, followed by adding 0.046 mol/L L-ascorbic acid of 25 mL and stirred for 2 h. Finally, the precipitate was collected by centrifugation and washed with water and ethanol. After drying under vacuum at 60 °C for 6 hours, the black powder was obtained and denoted as Cu_2O/ILGS-*x* (*x = 800*, *400*, *200*), where *x* represents the volume ratio of final solution to [Omim]Cl.

As a control sample, Cu_2O/ILGS was prepared without adding [Omim]Cl.

1.2.3 Materials Characterization

The crystal structure was investigated by an X-ray diffraction (XRD, X'Pert PRO MPD, Holland) with Cu Kα (40 kV, 40 mA, λ=1.5406 Å). Field emission scanning electron microscopy (FESEM, Hitachi S-4800, Japan) images and transmission electron microscopy (TEM, JEM-2010, 220 kV, Japan) images were captured to observe the morphology of the materials.

The elemental compositions and chemical bonding were analyzed by X-ray photoelectron spectroscopy (XPS, Thermo Scientific Escalab 250XI, America) with Al Kα radiation. The oxygen vacancies signal of materials were analyzed by electron

paramagnetic resonance (EPR, ENDOR spectrometer, JEOL JES FA300, Japan) at 25 °C. Fourier transformation infrared spectrum (FTIR) experiments were conducted on a Bruker Optics Tensor-27 FT-IR spectrometer.

Solid-state ^{13}C nuclear magnetic resonance spectroscopy (NMR, Bruker Avance III 400 MHz spectrometer, Switzerland) was recorded by a Bruker 7 mm double-resonance probe. Pulse sequence was CPTOSS. Magic-angle spinning (MAS) rate was 3 kHz. The ionic liquid analysis was analyzed by ^{13}C liquid nuclear magnetic resonance (NMR, Bruker Avance III 400 MHz spectrometer, Switzerland). CO_2 uptake isotherms were measured on a Micromeritics ASAP 2020 analyzer.

In-situ Raman measurements were tested by a Horiba LabRAM HR Evolution Raman microscope in a modified flow cell. The physical absorption properties of CO_2 were analyzed by the CO_2 uptake isotherms on a Micromeritics ASAP 2020 analyzer, America.

Zeta potential test was performed on a Malvern (Mastersizer 2000) system at 25 °C. The Brunner-Emmet-Teller (BET) specific surface area and pore properties were tested by nitrogen adsorption and desorption on a Micromeritics ASAP 2020 analyzer.

1.2.4 CO_2 Electrochemical Measurements

All electrochemical tests in an H-type electrolytic cell (H cell) and a flow cell, respectively, at room temperature were carried out on a CHI 760E electrochemical workstation (Shanghai CH Instruments Co., China).

In the H cell, the anode and cathode were separated by a Nafion 117 proton exchange membrane. Both compartments were filled with 0.1 M $KHCO_3$ aqueous solution of 40 mL as electrolyte. A L-type glassy-carbon (GC, ø = 12 mm) was coated with materials as working electrode, while an Ag/AgCl electrode (saturated KCl solution) and a platinum gauze (1×1 cm^2) were used as reference and counter electrode, respectively. The pH value of the CO_2 saturated electrolyte was 6.8. All potentials cited were referenced to the reversible hydrogen electrode (RHE) in this work. Before

electrochemical testing, the electrolyte was bubbled with N_2 for 30 min to exclude air in the solution. Then CO_2 was bubbled into the electrolyte in the cathode side for more than 30 min under stirring until saturated and the CO_2 gas flow was controlled at a steady stream (20 sccm) during the electrochemical measurements.

In the flow cell, the Fumasep FAA-3-PK-130 membrane was used as anion exchange membrane to separate the anodic and cathodic chamber. The gas diffusion electrode, Ag/AgCl electrode (saturated KCl solution) and Ni foam were used as working, reference and counter electrodes, respectively. During performance evaluations, anodic and cathodic chambers were circulated with electrolyte (1M KOH) at the rate of 20 sccm, respectively. A steady CO_2 stream (20 sccm) was fixed in gas chamber. The applied potentials were dealt with *iR* drop compensation.

For preparation of the H cell working electrode, the glassy carbon (GC) electrode was polished and thoroughly rinsed in water and ethanol, respectively, then was dried with wiper for lens. catalyst ink (materials of 5.0 mg in 5 % Nafion solution of 10 μL and acetone of 500 μL) of 100 μL dripped on the GC electrode and dried with N_2.

For preparation of the flow cell working electrode, the catalyst ink made by 10 mg catalysts, acetone of 1.0 mL and 5 % Nafion solution of 20 μL were mixed and sonicated for 20 min to get the catalyst ink. Then, the catalyst ink of 100 μL was dropped on polytetrafluoroethylene (PTFE) membrane (Fuel Cell Store) under vacuum condition. A gas diffusion electrode loading with ~1.0 mg cm^{-2} was obtained.

1.2.5 Products Analysis

The gas phase products in the cathodic side were online tested with a gas chromatograph (BFRL-3420A, China) using Ar as a carrier gas. The gas chromatograph was equipped with a thermal conductivity detector (TCD) to detect hydrogen and a flame ionization detector (FID) to detect hydrocarbons and CO. The liquid products were quantified by a high-performance liquid chromatograph (HPLC, LC-2030 Plus,

Shimadzu, Japan) with differential refraction detector (RID-20A). All products were quantitatively analyzed by external standard curve method.

The liquid products were further confirmed by ^{1}H NMR (Bruker Avance III 400 HD spectrometer) in deuteroxide. Two internal standards were used in NMR analysis. The Dimethyl sulfoxide (DMSO) was the reference for ethanol. And the phenol was used as the reference for formate. After reaction, catholyte of 1.0 mL was mixed with 100 mM DMSO of 50 μL and 200 mM phenol of 50 μL. Finally, the solution mixed with above solution of 300 μL and D_2O of 550 μL was used for ^{1}H NMR test.

The faradic efficiencies of all products were calculated according to Eq. 1:

$$FE = \frac{moles\ of\ product}{Q/nF} \times 100\% \quad \text{Eq. 1}$$

(Q: electric quantity; F: Avogadro constant; n: transferred electron number)

The energy conversion efficiencies (EE) of the half-cell were calculated according to Eq. 2 [13]:

$$EE = (1.23 - E_i) \times FE_i/(1.23 - E_{app}) \quad \text{Eq. 2}$$

where E_i represented the thermodynamic potential (*vs.* RHE) in CRR for product *i*. The value was 0.06 V for C_2H_4 and 0.08 V for C_2H_5OH. E_{app} was the applied potential (*vs.* RHE).

1.2.6 Computational Details

All the calculations were implemented through Vienna ab initio simulation package (VASP) with the projector augmented wave (PAW) method. In DFT calculation, the generalized gradient approximations (GGA) of Perdew-Burke-Ernzerhof (PBE) functional were applied. The cutoff energy was set as 400 eV. The Monkhorst-Pack meshes of 2×2×1 *k*-point sampling in the Brillouin zone were employed for all calculations. The self-consistent electronic step convergence criterion was 1×10^{-5} eV. When the optimized convergence criterion was met, the maximum remaining force on each atom was less than 0.02 eV/Å.

The adsorption energy was calculated as:

$$E_{ads} = E_{slab+adsorbent} - E_{slab} - E_{adsorbent} \quad \text{Eq. 3}$$

Where $E_{slab+adsorbent}$, E_{slab} and $E_{adsorbent}$ represent the total energies of the surface slab with adsorbent, the clean surface slab, and gas phase adsorbent, respectively.

The Gibbs free energy was calculated as:

$$\Delta G = \Delta E + \Delta G_{correction} \quad \text{Eq. 4}$$

$$\Delta G_{correction} = E_{ZPE} + U(T) + TS(T) + PV \quad \text{Eq. 5}$$

Where ΔE was the reaction energy based on DFT calculations and E_{ZPE}, U(T)+PV,TS(T) stand for the zero-point energy, the enthalpic temperature correction, and the entropy corrections. $\Delta G_{correction}$ were calculated by VASPKIT [30].

1.3 Results

1.3.1 Synthesis and Characterizations of Materials

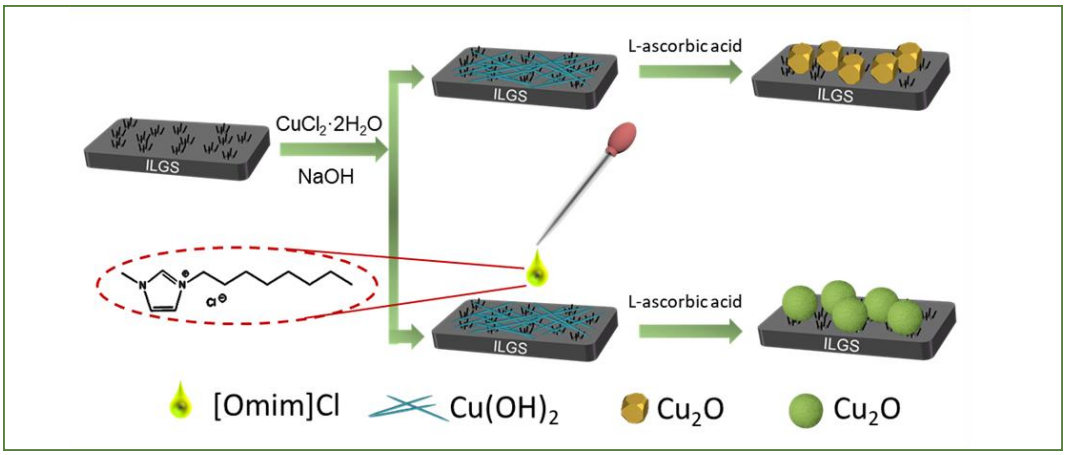

Fig. 1.1. The preparation of Cu_2O/ILGS-*x*.

The synthesis process of Cu_2O/ILGS composite material was schematically illustrated in Fig. 1.1. Firstly, the ionic liquid functionalized graphite sheets (ILGS) was synthesized according to our previous work (Fig. 1.2) [29, 31]. Then, $Cu(OH)_2$/ILGS (Fig. 1.3) precipitate was prepared by adding NaOH into $CuCl_2$ solution. After that, it was reduced to Cu_2O/ILGS-*x* by a certain content of [Omim]Cl and L-ascorbic acid (*x* = *800*, *400*, *200*, where *x* represents the volume ratio of final solution to [Omim]Cl).

Without the addition of [Omim]Cl, Cu_2O/ILGS was prepared as the control experiment. During the synthesis process, the color of solution changed with the amount of [Omim]Cl added (Fig. 1.4), reflecting its key role in tailoring the growth of Cu_2O crystals. The prepared samples were investigated by further characterizations.

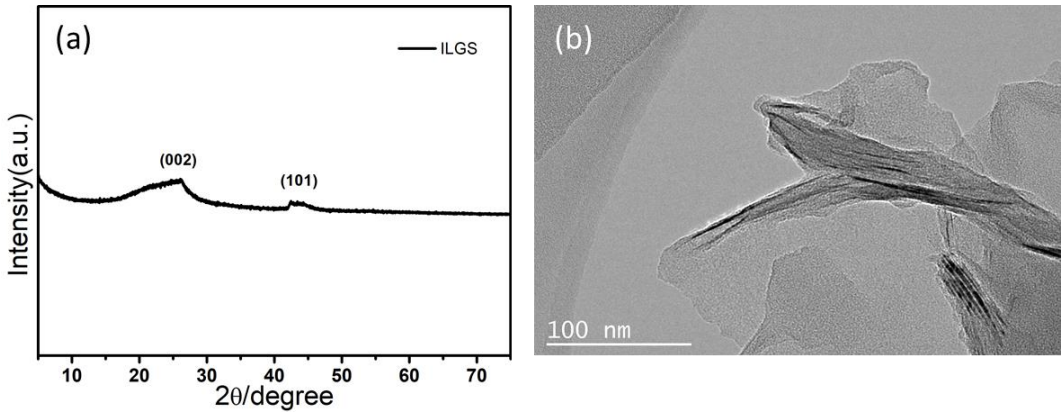

Fig. 1.2. (a) XRD pattern and (b) TEM image of ILGS.

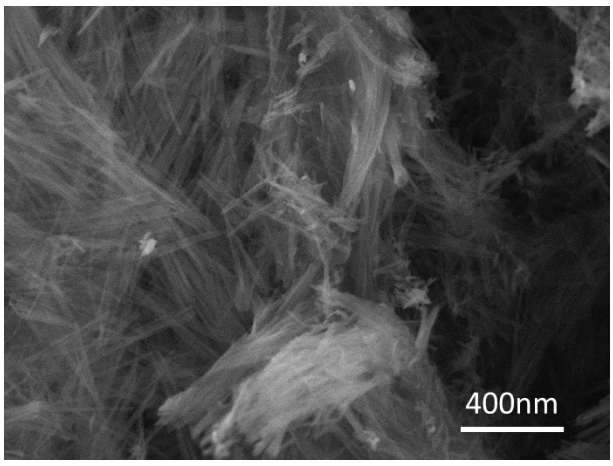

Fig. 1.3. SEM image of $Cu(OH)_2$/ILGS.

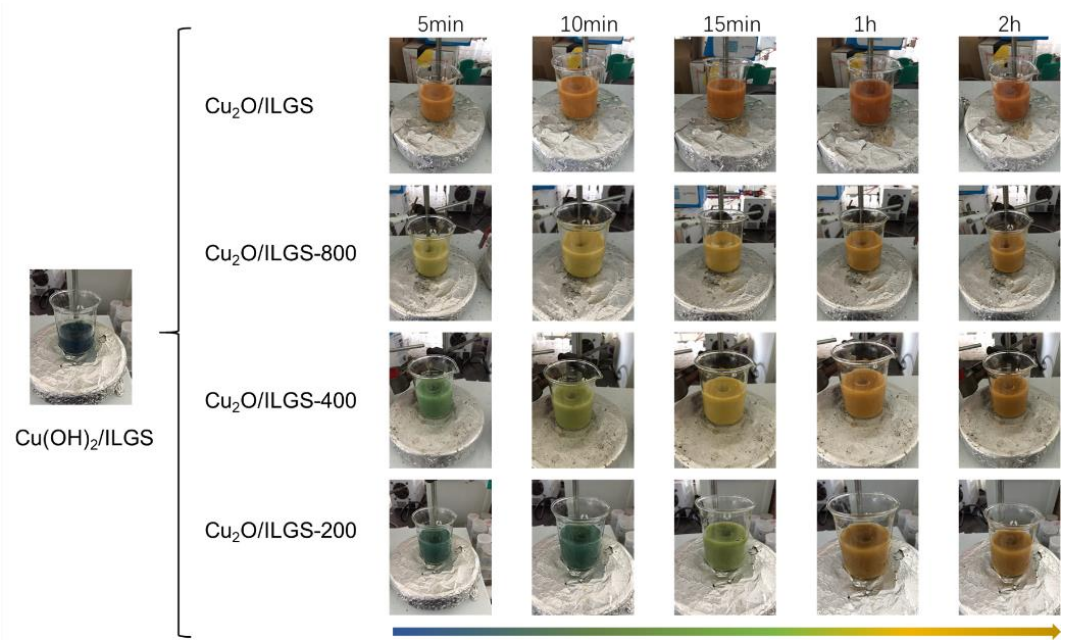

Fig. 1.4. Digital photos for the preparation of Cu_2O/ILGS-*x*.

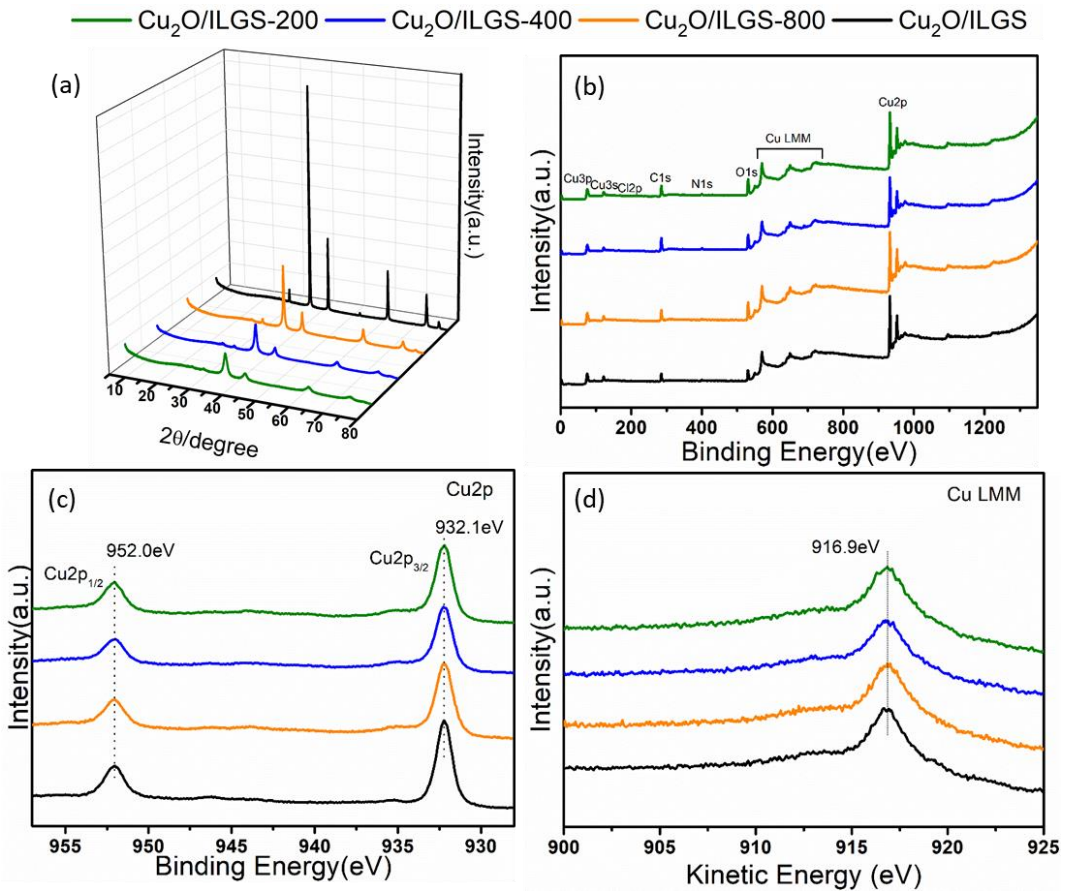

Fig. 1.5. (a) XRD patterns, (b) XPS spectra, (c) High-resolution Cu 2p spectra and (d) Cu LMM Auger spectra of Cu_2O/ILGS-*x*.

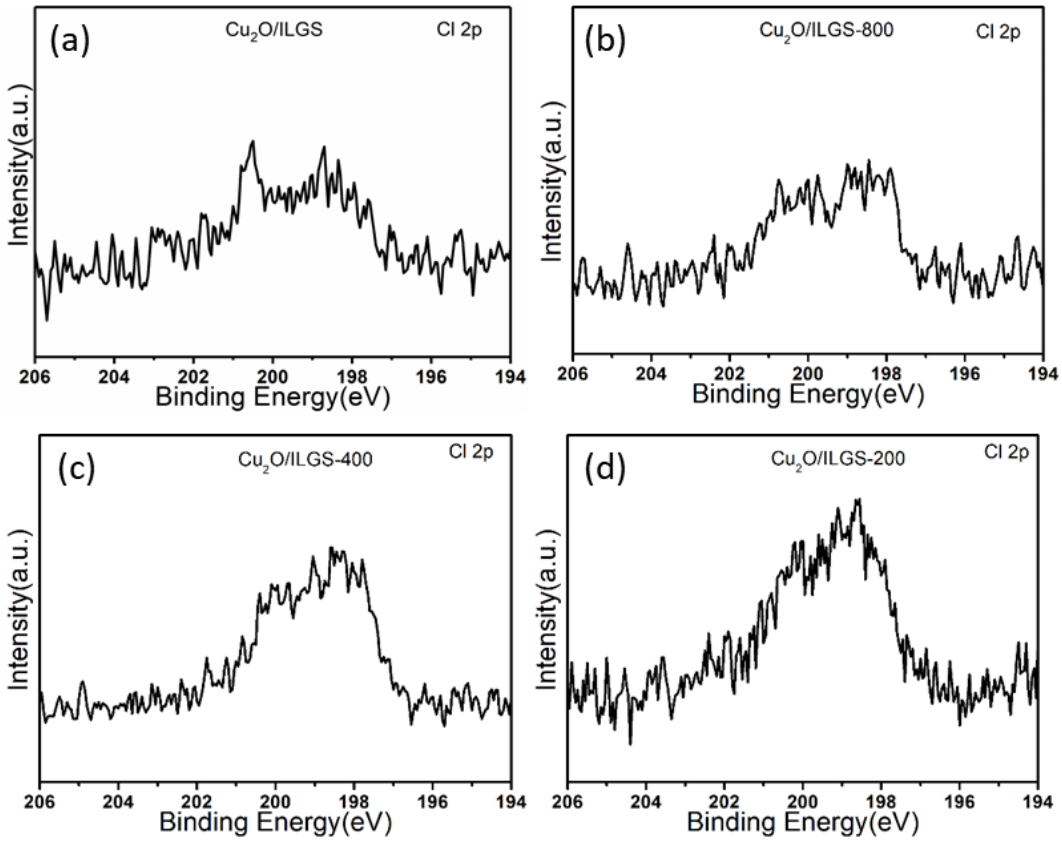

Fig. 1.6. (a-d) High-resolution Cl 2p spectra of Cu_2O/ILGS-*x* in XPS spectra.

The X-ray diffraction patterns (XRD) and X-ray photoelectron spectroscopy (XPS) spectra indicated that Cu_2O nanocrystals were successfully obtained and *in-situ* loaded on ILGS. The peaks at 26.2° and 44.4°were ascribed to the (002) and (101) plane of ILGS in Fig. 1.2a [31]. As depicted in Fig. 1.5a, a series of typical diffraction peaks at 29.6°, 36.5°, 42.4°, 52.6°, 61.5°, 73.7°, and 77.6° were respectively ascribed to the (110), (111), (200), (211), (220), (311), and (222) planes of Cu_2O (JCPDS No. 65-3288). All Cu_2O/ILGS-*x* samples have the same characteristic peaks without any impurity peaks in the XRD patterns. It was worth noting that the diffraction peaks of Cu_2O/ILGS-*800*, *400*, *200* were weaker than Cu_2O/ILGS, indicating that [Omim]Cl could weaken the crystallinity of Cu_2O. The XPS spectra were employed to study the surface composition and valence states of Cu_2O. As shown in Fig. 1.5b-d and Fig. 1.6, all Cu_2O/ILGS-*x* consisted of C, N, Cl, O, and Cu elements. In Fig. 1.5c, the characteristic peaks at 932.1 eV and 952.0 eV were ascribed to Cu $2p_{3/2}$ and Cu $2p_{1/2}$, respectively

[32]. The specific valence of Cu^{+} and Cu^{0} was further investigated by Cu LMM Auger spectra (Fig. 1.5d), and the kinetic energy around 916.9 eV confirmed the purity of Cu_2O without Cu^{0} exiting [33].

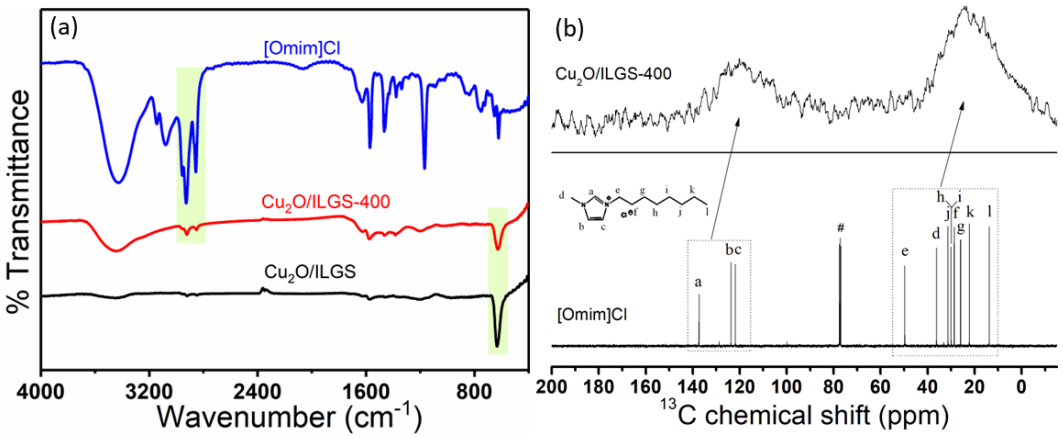

Fig. 1.7. (a) FTIR spectra of [Omim]Cl, Cu_2O/ILGS-400 and Cu_2O/ILGS. (b) Solid-state ^{13}C NMR spectra of Cu_2O/ILGS-400 and liquid-state ^{13}C NMR spectra of [Omim]Cl. #: $CDCl_3$.

The interaction of [Omim]Cl and Cu_2O nanoparticles were further investigated by FTIR, as shown in Fig. 1.7a. In Cu_2O/ILGS-*400* and [Omim]Cl, the bands from 2800 cm^{-1} to 3000 cm^{-1} revealed the presence of C-H stretching vibration of imidazolium ring. The broad wave between 3200 cm^{-1} and 3500 cm^{-1} belonged to the imidazolium group in ionic liquids [34, 35]. In contrast, Cu_2O/ILGS did not show obvious signal of C-H stretching. Furthermore, the ^{13}C NMR spectra of Cu_2O/ILGS-*400* (Fig. 1.7b) show a clear broadening and shifting of resonance peaks compared with [Omim]Cl, which was attributed to the interactions between [Omim]Cl and Cu_2O [36].

The morphologies of Cu_2O/ILGS-*x* were investigated by FESEM and TEM (Fig. 1.8 and Fig. 1.9). The Cu_2O in Cu_2O/ILGS was polyhedral with an average diameter of 182 nm, as shown in Fig. 1.8a and Fig. 1.9a. The inset intuitively exhibited the crystal structure of Cu_2O/ILGS with (100) plane mainly exposed. After the introduction of [Omim]Cl, the morphologies of Cu_2O in Cu_2O/ILGS-*800* (Fig. 1.9b), Cu_2O/ILGS-*400* (Fig. 1.8e and Fig. 1.9c) and Cu_2O/ILGS-*200* (Fig. 1.9d) changed to quasi-spherical

structure with an obviously rough surface, while the (100) crystal planes were inhibited due to the surfactant-like effects of $[Omim]^+$. The fine structure of Cu_2O/ILGS-*x* was revealed by typical HRTEM images. In Fig. 1.8b-d, the regular lattice structure of (200), (111) and (110) corresponding to the polyhedron Cu_2O with high crystallinity were confirmed, which was consistent with its SAED pattern. However, the SEAD of Cu_2O/ILGS-*400* showed weaker strength of dispersing diffraction rings than Cu_2O/ILGS, indicating that the crystallinity of Cu_2O was reduced with introduction of [Omim]Cl, which was consistent of XRD results. In Fig. 1.8f and g, abundant grain boundaries were created on Cu_2O/ILGS-*400* [37, 38]. These grain boundaries had more unsaturated Cu atoms, which was beneficial for the CRR to C_2 reaction [39]. In the end, SEM (Fig. 1.8h) and TEM (Fig. 1.10) EDS element mapping images of Cu_2O/ILGS-*400* showed all the elements in the materials as made were uniformly distributed.

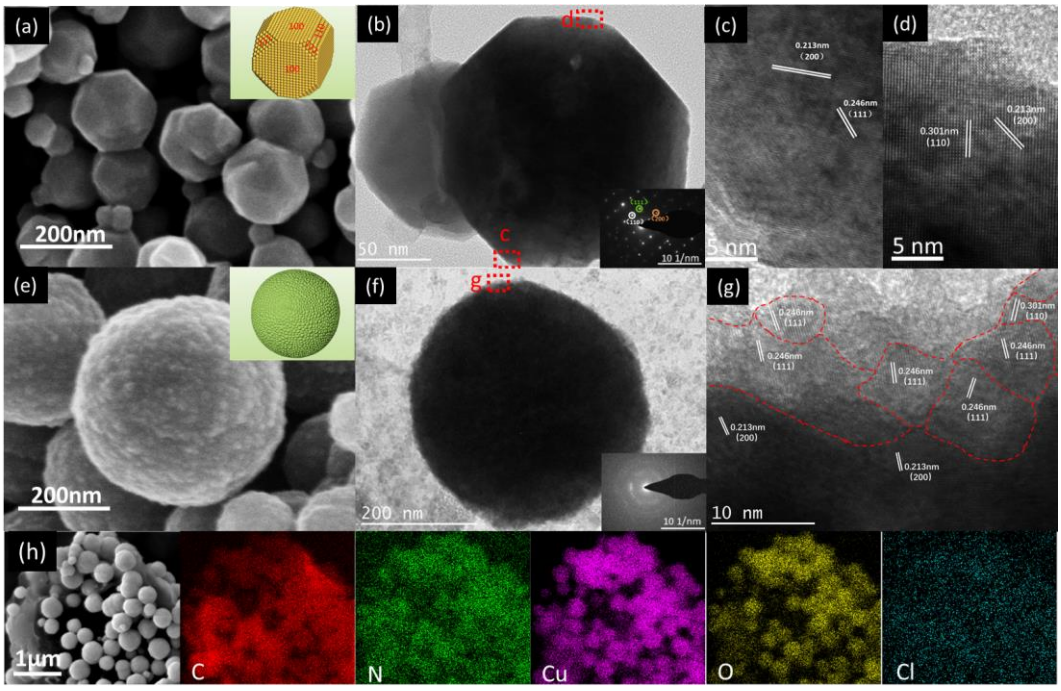

Fig. 1.8. (a) SEM images (inset shows crystal structure simulation diagram), (b) TEM image (inset shows the corresponding SAED pattern), (c, d) HRTEM image of Cu_2O/ILGS. (e) SEM images (inset shows crystal structure simulation diagram), (f) TEM image (inset shows the corresponding SAED pattern), (g) HRTEM image and (h) SEM elemental mapping images of Cu_2O/ILGS-*400*.

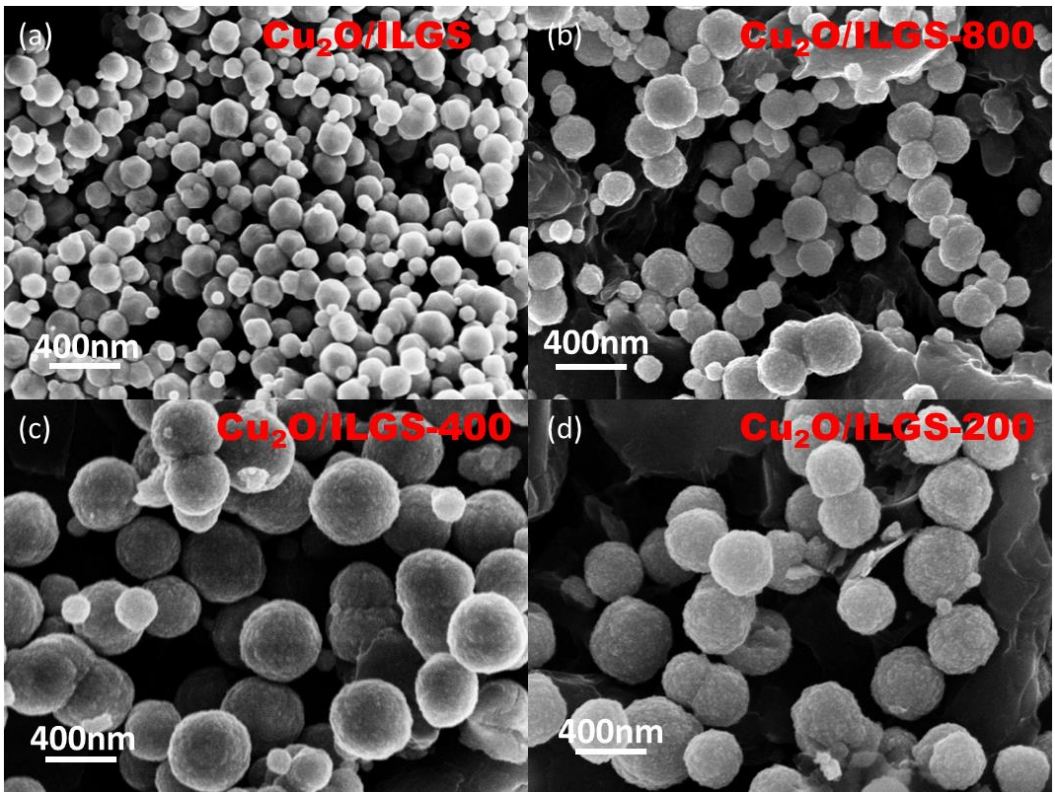

Fig. 1.9. SEM images of pristine (a) Cu_2O/ILGS, (b) Cu_2O/ILGS-*800*, (c) Cu_2O/ILGS-*400*, (d) Cu_2O/ILGS-*200*.

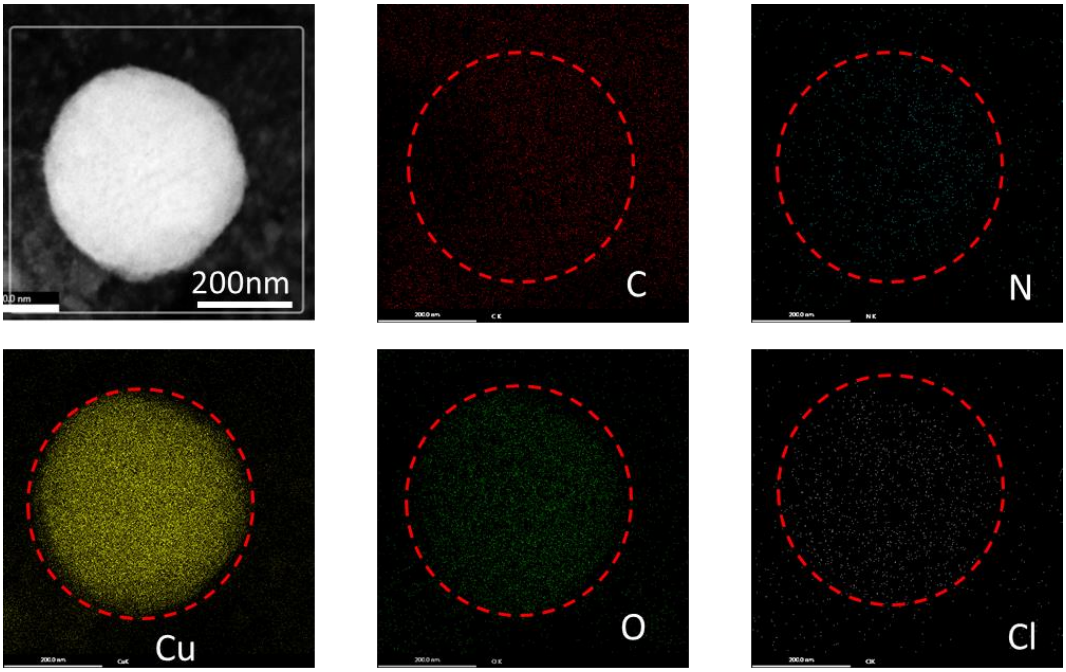

Fig. 1.10. TEM elemental mapping images of Cu_2O/ILGS-*400*.

The morphology control mechanism of Cu_2O was agreed with the surfactant effect [40]. During the growth of Cu_2O, $[Omim]^+$ reduced the surface energy of materials and inhibited the growth of larger crystal planes, thus facilitating the formation of quasi-spherical morphology with rough surface. N_2 physisorption was applied to determine the specific surface areas and porosity of Cu_2O/ILGS-*x* catalysts, as shown in Fig. 1.11 and Table 1.1. Cu_2O/ILGS had a minimal surface area (2.7 $m^2 \cdot g^{-1}$), indicating the Cu_2O synthesized without ionic liquid assisting had no porous structure. In contrast, a type IV pattern with obvious hysteresis loop was clearly observed in Cu_2O/ILGS-*x*, proving the mesoporous structure was formed in Cu_2O with ionic liquid assisting. However, too much ionic liquid leaded to the collapse of Cu_2O, which made Cu_2O/ILGS-*200* (55.4 $m^2 \cdot g^{-1}$) have a relatively smaller surface area than Cu_2O/ILGS-*400* (63.9 $m^2 \cdot g^{-1}$).

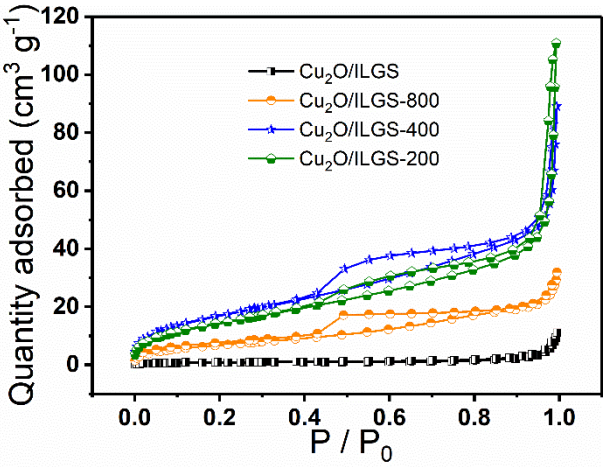

Fig. 1.11. Typical N_2 adsorption-desorption isotherms of Cu_2O/ILGS-*x*.

Table 1.1. Summary of surface area and pore volume of the samples.

Sample	S_{BET} ($m^2 \cdot g^{-1}$)	S_{BET}^{Micro} ($m^2 \cdot g^{-1}$)	S_{BET}^{Meso} ($m^2 \cdot g^{-1}$)	**V** ($cm^3 \cdot g^{-1}$)
Cu_2O/ILGS	2.7	0.2	2.5	0.0163
Cu_2O/ILGS-*800*	25.5	6.2	19.3	0.0442
Cu_2O/ILGS-*400*	63.9	11.6	52.3	0.125
Cu_2O/ILGS-*200*	55.4	9.3	46.1	0.161

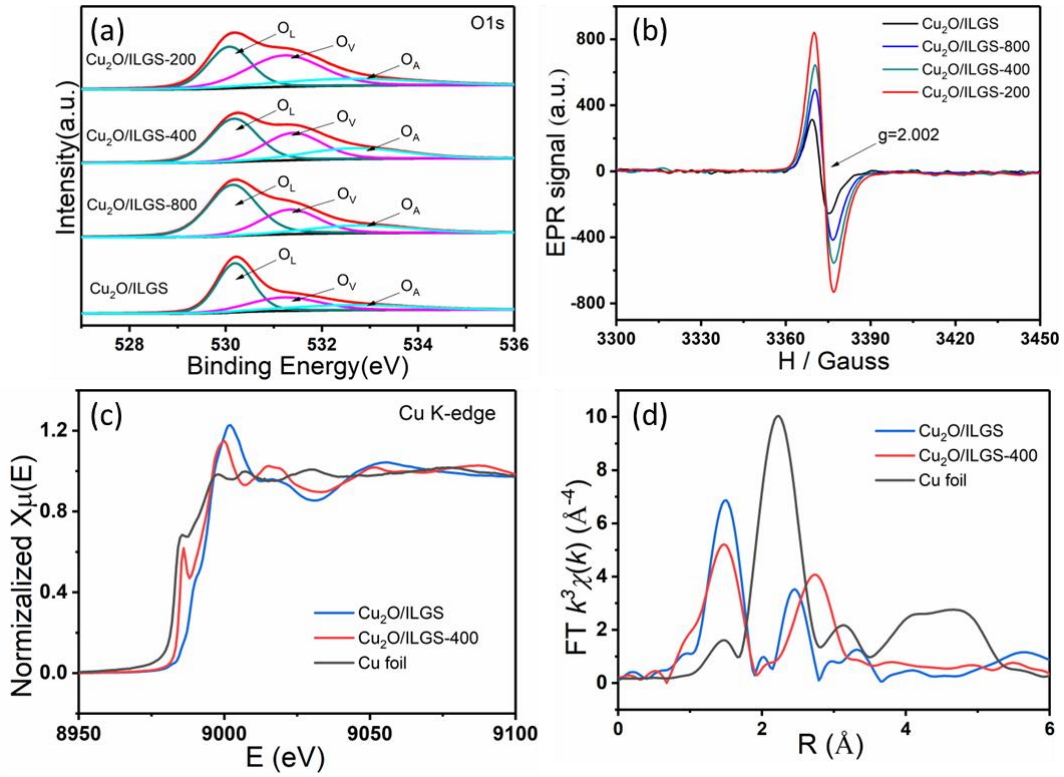

Fig. 1.12. (a) O 1s XPS core level spectra of as-synthesized Cu_2O/ILGS-*x*. O_L, O_V and O_A correspond to oxygen lattice, oxygen vacancy, and oxygen adsorbed, respectively. (b) Room-temperature EPR spectra of the samples. (c) XANES spectra at the Cu K-edge for different catalysts. (d) The corresponding Fourier transforms FT($k^3\chi(k)$) of different catalysts.

Table 1.2. The fitting results of O 1s XPS spectra of Cu_2O/ILGS-*x*.

Samples	**O_L**	**O_V**	**O_A**
Cu_2O/ILGS	91.8%	4.9%	3.3%
Cu_2O/ILGS-800	54.6%	29.5%	15.9%
Cu_2O/ILGS-400	43.3%	33.7%	23.0%
Cu_2O/ILGS-200	34.8%	45.7%	19.5%

Apart from the morphology, the oxygen vacancies in Cu_2O were significantly enhanced with the introduction of [Omim]Cl, which was proved by XPS and EPR results. According to the O 1s of XPS spectra in Fig. 1.12a, three peaks at the binding

energies of 530.1, 531.3, and 532.9 eV were attributed to the oxygen lattice (O_L) of Cu_2O, oxygen associated with an oxygen vacancy environment (O_V), and the ambient oxygen adsorbed (O_A) on the surface of nanoparticles arising from hydroxyl [41]. As listed in Table 1.2, the content of V_O on Cu_2O/ILGS-*800*, Cu_2O/ILGS-*400*, and Cu_2O/ILGS-*200* samples were 29.5%, 33.7%, and 45.7%, respectively. All of them were higher than Cu_2O/ILGS (4.9%), proving the introduction of Cl^- by [Omim]Cl resulted in abundant V_O [42]. The existence of oxygen vacancies was further identified by EPR spectra. As shown in Fig. 1.12b, all Cu_2O/ILGS-*x* possessed similar electron paramagnetic resonance signal at g = 2.002, which was derived from the electrons captured by oxygen vacancy [43]. The intensity of EPR for Cu_2O/ILGS-*x* samples follows the order: Cu_2O/ILGS-*200* > Cu_2O/ILGS-*400* > Cu_2O/ILGS-*800* > Cu_2O/ILGS, which indicates that the content of oxygen vacancies increased monotonously with the increasing addition of [Omim]Cl.

X-ray absorption near-edge structure (XANES) and extended X-ray absorption fine structure (EXAFS) characterizations obtained the detailed structural information of catalysts. As shown in Fig. 1.12c, the Cu K-edge XANES spectra showed that the near-edge absorption energy of Cu_2O/ILGS-*400* was between that of Cu foil and Cu_2O/ILGS, suggesting that the oxidation of the Cu atom was below +1 [44]. The EXAFS was shown in Fig. 1.12d, Cu_2O/ILGS-*400* exhibited two major peaks about 1.9 Å and 3.0 Å, which can be attributed to the Cu-O and Cu-Cu coordination, respectively. The fitting data of coordination number of Cu-O was 1.5 (Table 1.3 and Fig. 1.13), which was smaller than Cu_2O/ILGS (2.7). The Cu K-edge Wavelet transform-EXAFS (with high resolution in both k and R space) was carried out in Fig. 1.14a-c. The WT contour plot of Cu_2O/ILGS-*400* exhibited one intensity maximum at about 6.1 $Å^{-1}$, which was in between Cu_2O/ILGS (5.9 $Å^{-1}$) and Cu foil (8.8 $Å^{-1}$). This was due to the absence of oxygen atoms around the copper forming oxygen vacancies, which was consistent with the results of EPR and XPS. It can be concluded that Cl^- of [Omim]Cl will lead to more oxygen vacancies.

Table 1.3. Structural parameters of different catalysts extracted from the EXAFS fitting.

Sample	Path	CN	R(Å)	σ^2(×10^{-3}Å^2)	ΔE_0(eV)	R factor
Cu_2O/ILGS-*400*	Cu-O	1.5	1.86	0.6	8.5	0.016
	Cu-Cu	10.3	3.02	17.9		
Cu_2O/ILGS	Cu-O	2.7	1.94	1.8	-0.6	0.017
	Cu-Cu	8.6	2.97	18.8		

[a] C*N*: coordination numbers; *R*: bond distance; σ^2: Debye-Waller factors; ΔE_0: the inner potential correction. *R* factor: goodness of fit. S_0^2, 0.85, was obtained from the experimental EXAFS fit of Cu foil reference by fixing CN as the known crystallographic value and was fixed to all the samples.

[b] Fitting range: 2.1 ≤ k (/Å) ≤ 11 and 1.2 ≤ R (Å) ≤ 2.7, Fitting range: 2.1≤ k (/Å) ≤ 11 and 1 .2≤ R (Å) ≤ 2.65.

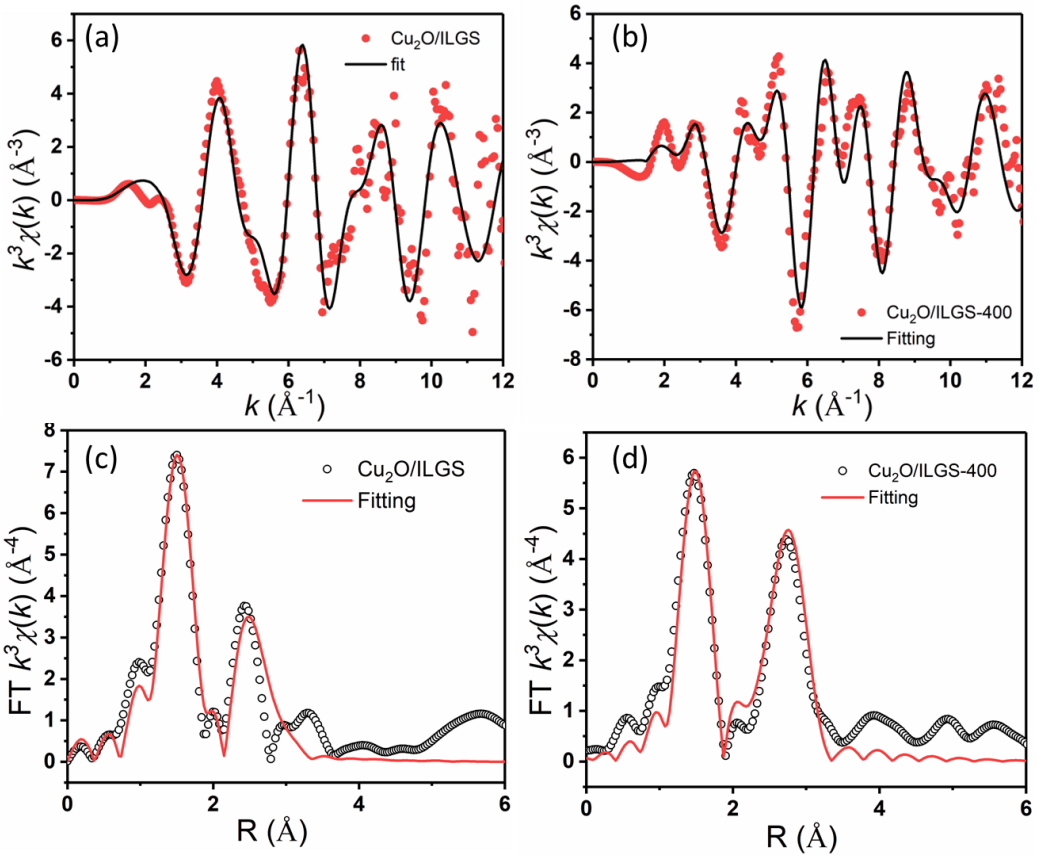

Fig. 1.13. The EXAFS data fitting results of Cu_2O/ILGS and Cu_2O/ILGS-400.

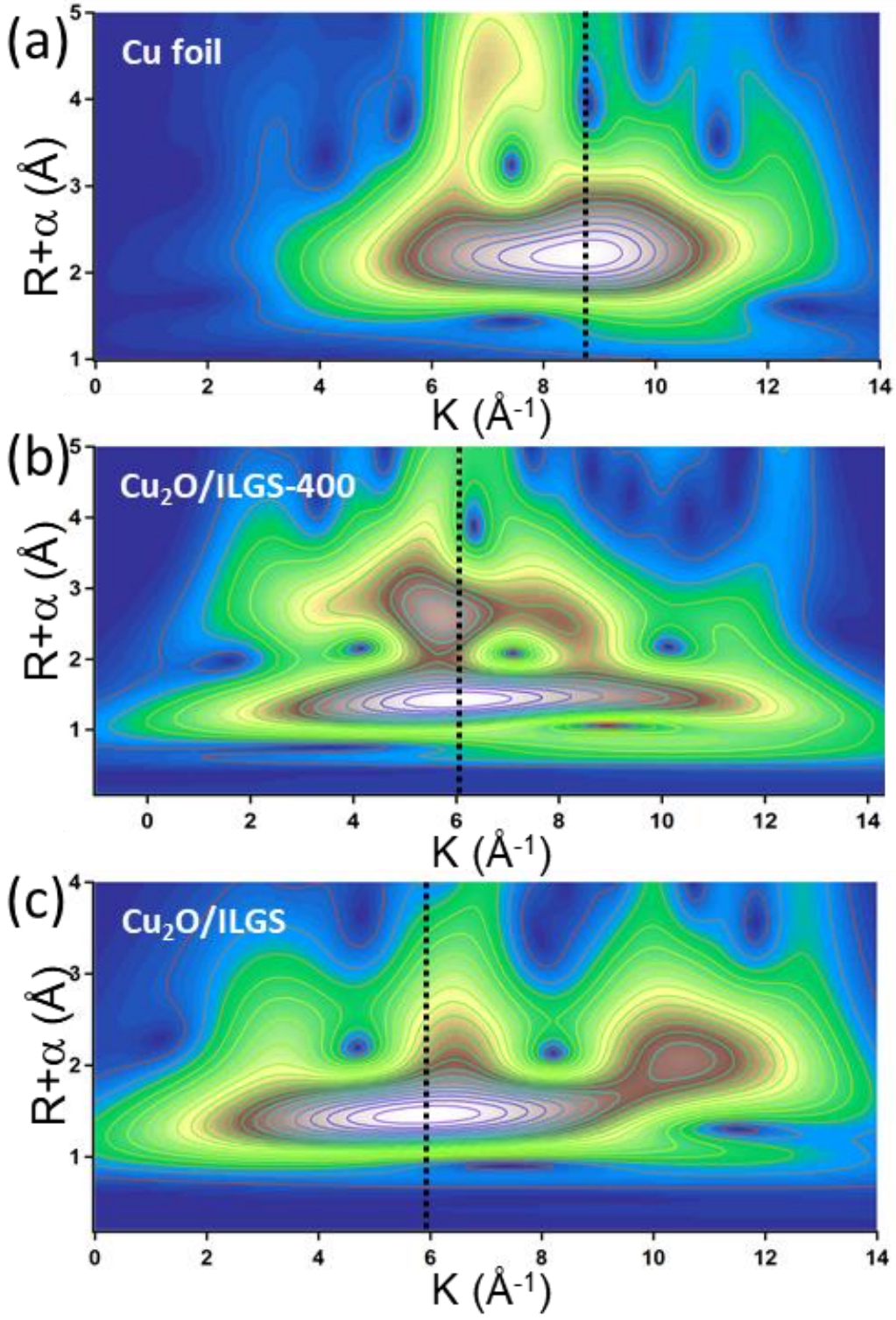

Fig. 1.14. (a-c) Cu K-edge Wavelet transform -EXAFS contour plots of Cu foil, Cu_2O/ILGS-400 and Cu_2O/ILGS.

The formation mechanism of oxygen vacancies in Cu_2O was further explained by a double electric layer model. It is well known that the positive charge on the surface of Cu_2O nanoparticles (Fig. 1.15 verified by Zeta potential) can adsorb anionic in the solutions due to the electrostatic attraction. On the other hand, the Cl^- was absorbed on the surface of Cu_2O, which occupied the position of oxygen to induce oxygen vacancies [45]. When [Omim]Cl was added, the anions and cations form a three-dimensional network by hydrogen bonds [46]. As a result, $[Omim]^+$ was able to stabilize and raise the concentration of Cl^- around the surface of Cu_2O. Consequently, more oxygen vacancies were obtained due to the stabilizing effects of Cl^- on Cu^+ [16]. On the contrary, the Cl^- of Cu_2O/ILGS surface moves freely in the solution, which cannot be maintained to create more oxygen vacancies. It can be concluded that the formation of abundant oxygen vacancies on the rough surface of Cu_2O were attributed to the synergy effects of the anion and cation of [Omim]Cl [47], which may possess excellent catalytic performance towards CRR to C_2 products.

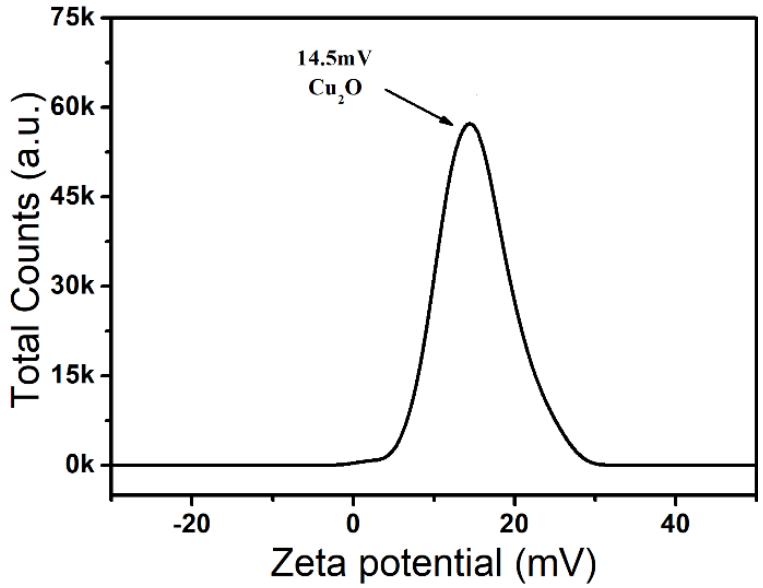

Fig. 1.15. Zeta Potential of the Cu_2O.

1.3.2 Electrocatalytic Performance of CRR in the H Cell

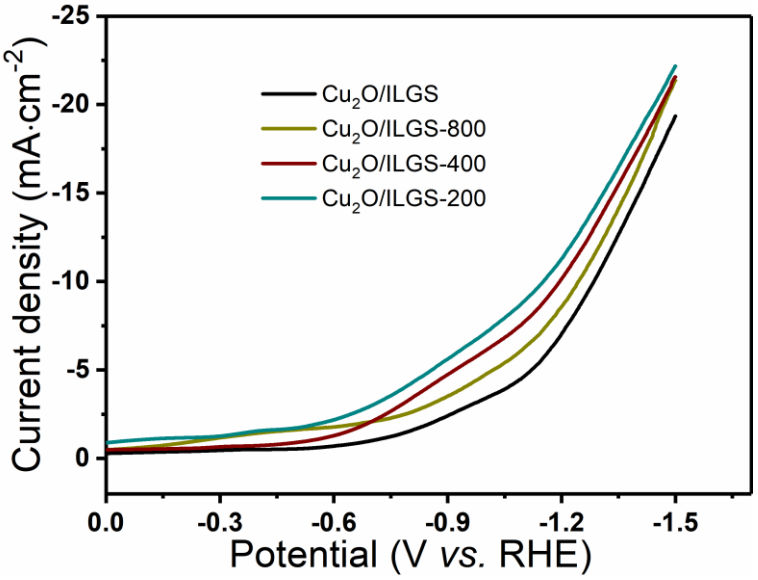

Fig. 1.16. LSV curves over Cu_2O/ILGS-*x* in H cell.

The CO_2 electrocatalysis reduction activities of all Cu_2O/ILGS-*x* samples were first investigated using a typical H-type cell with 0.1 M $KHCO_3$ as electrolyte. As shown in Fig. 1.16, the linear sweep voltammetry (LSV) of Cu_2O/ILGS-*x* were tested with applied potential from 0 V to -1.5 V (*vs.* RHE). The current densities of Cu_2O/ILGS-*x* samples were higher than Cu_2O/ILGS, reflecting a positive electrochemical activity of Cu_2O/ILGS-*x*. As shown in Fig. 1.17, various products including C_2H_4, C_2H_5OH, CH_4, CO, formate and H_2 were detected on all the as made catalysts as made with total FE of ca. 100%. The liquid products, C_2H_5OH and formate, were confirmed by ^1H NMR in Fig. 1.18. For C_2 products, all the catalysts showed the best performance at −1.15 V (*vs.* RHE). Typically, the FE of C_2 over Cu_2O/ILGS-*400* was the highest, which was 62.4% with a current density of 11.7 mA cm^{-2}, including 36.7% of C_2H_4 and 25.7% of C_2H_5OH (Fig. 1.19 and Fig. 1.17). The outstanding catalytic performance of Cu_2O/ILGS-*400* among all the samples was attributed to the combination effects of abundant oxygen vacancies and highest surface area on Cu_2O. This was consistent to the results of EPR and N_2 physisorption.

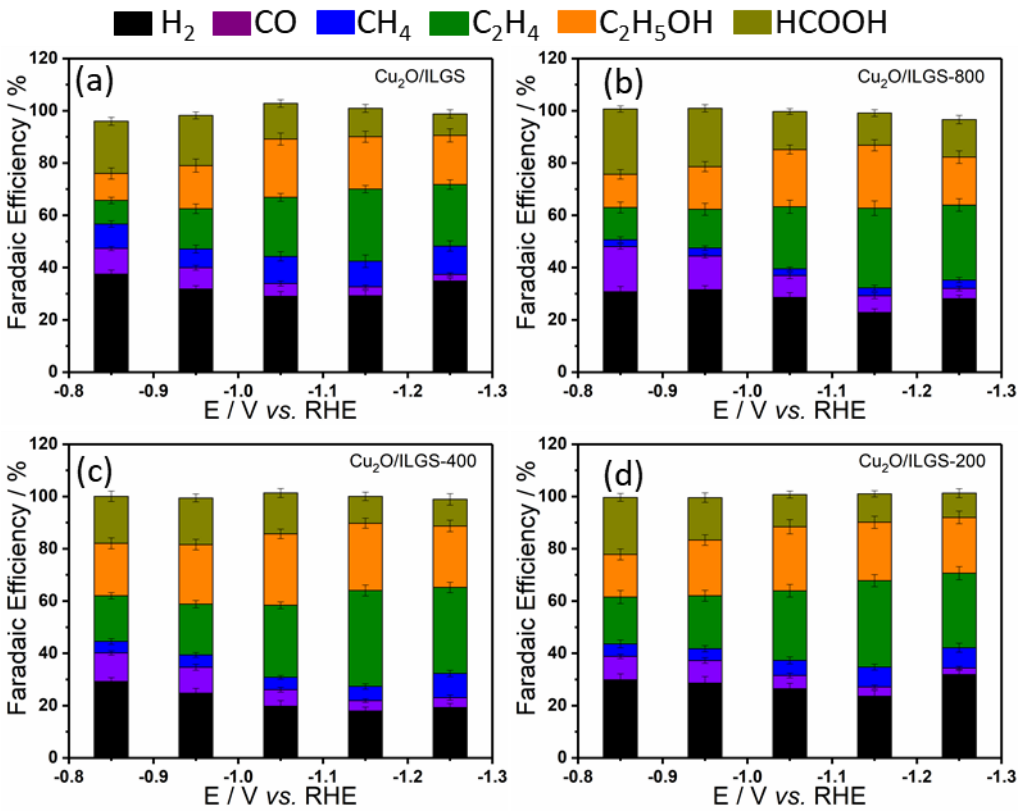

Fig. 1.17. FE for products over (a) Cu_2O/ILGS, (b) Cu_2O/ILGS-*800*, (c) Cu_2O/ILGS-*400*, (d) Cu_2O/ILGS-*200* at different potentials.

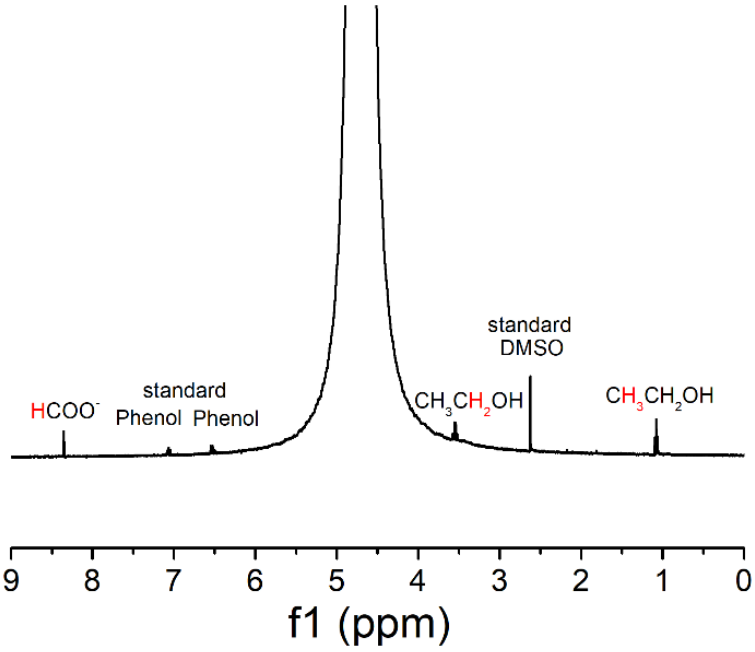

Fig. 1.18. A typical ^{1}H NMR spectrum of liquid products after electrolysis with the Cu_2O/ILGS-*400* catalyst.

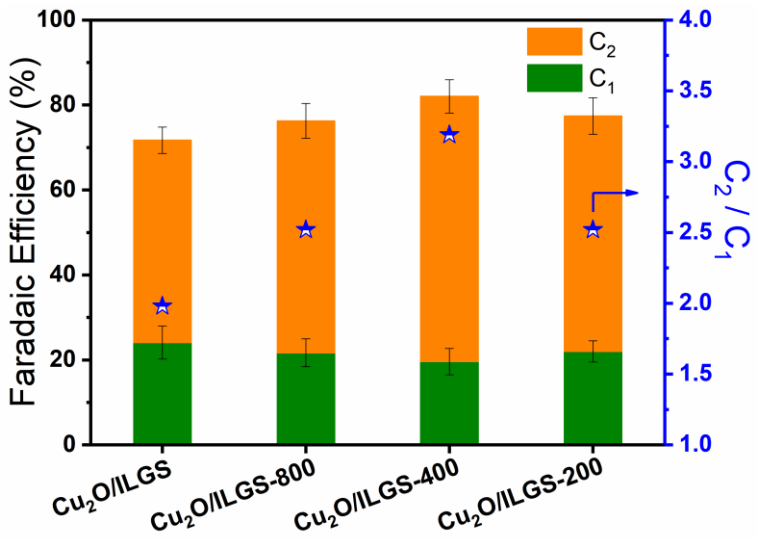

Fig. 1.19. Faradaic efficiency of C_1 and C_2 at −1.15 V (*vs.* RHE).

As a control experiment, the catalytic performance of Cu_2O/ILGS was investigated by directly adding [Omim]Cl into 0.1 M $KHCO_3$ electrolyte (Fig. 1.20). It was found that C_2 products was not improved, indicating the good catalytic performance of Cu_2O/ILGS-*400* comes from Cu_2O rather than the ionic liquid on the surface of electrocatalyst. Furthermore, we also compared the effects of different ionic liquids with different length of cationic chain and anion species on the catalytic performance of Cu_2O, such as [Emim]Cl, [C_{16}mim]Cl and [Omim]Br. As shown in Fig. 1.21, the CRR performance of Cu_2O/ILGS-*y* (where y represents the kind of ionic liquids) was tested at -1.15 V (*vs.* RHE). With no exception, all the samples did not show any better C_2 selectivity than Cu_2O/ILGS-*400*, indicating [Omim]Cl, with specific chain length and anion, has unique characteristics in controllable morphology and defects of Cu_2O. By comparing with the data of other Cu-based catalysts reported in Table 1.4, this work had relatively high FE for C_2 products in H-cell. At last, the stability of Cu_2O/ILGS-*400* was tested at −1.15 V (*vs.* RHE) for 15 h (Fig. 1.22), proving the current density and selectivity of C_2 are both stable during the entire period.

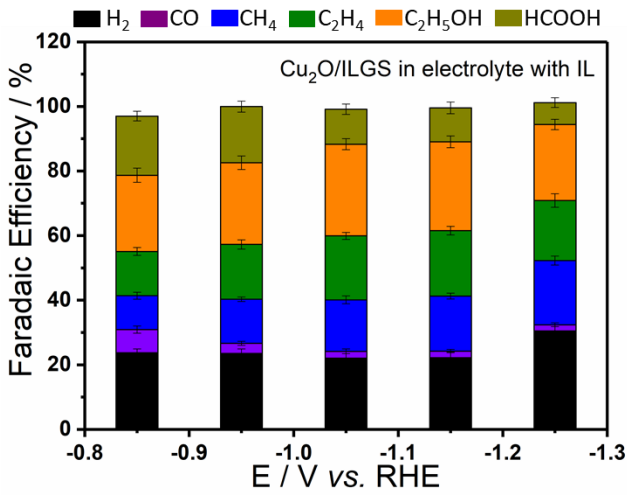

Fig. 1.20. FE for products over Cu_2O/ILGS at different potentials in 0.1M $KHCO_3$ with [Omim]Cl as an additive.

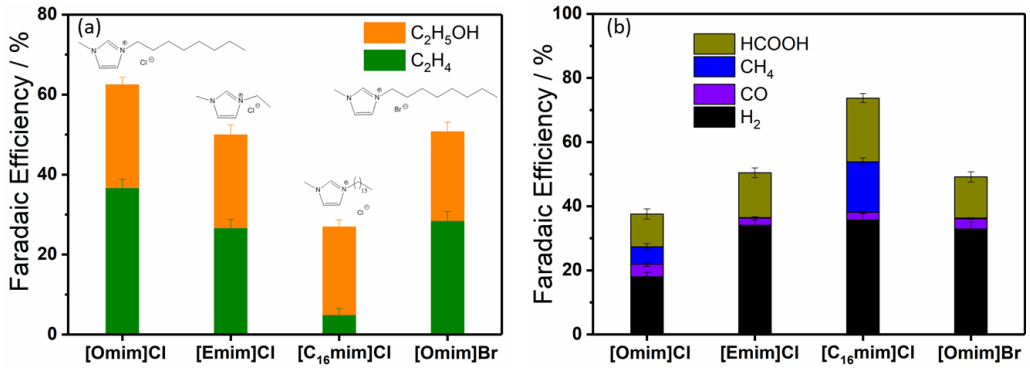

Fig. 1.21. FE of (a) C_2 and (b) other products over Cu_2O/ILGS with different ionic liquid in the H cell at −1.15 V (*vs.* RHE).

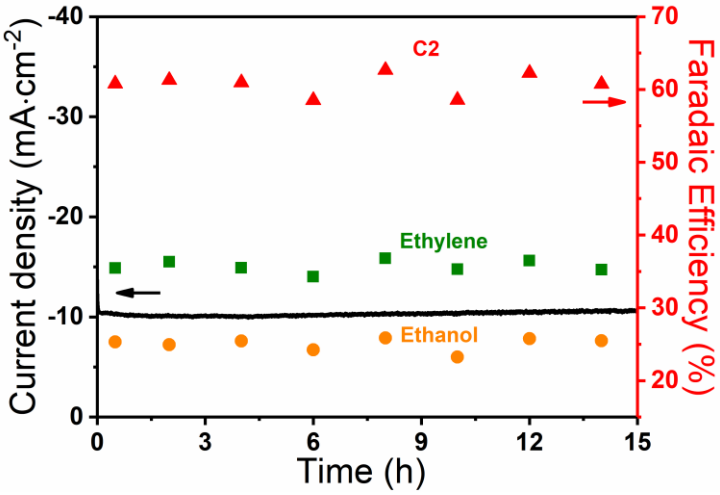

Fig. 1.22. Stability test of Cu_2O/ILGS-*400* at −1.15 V (*vs.* RHE).

Table 1.4. Overview of Cu based catalysts for reduction of CO_2 to C_2 products.

Electrocatalyst	Potential (V *vs.* RHE)	Electrolyte	FE_{C2+} (%)	*j* (mA cm^{-2})	Reference
Cu_2O/ILGS-*400*	**-1.15**	**0.1M $KHCO_3$**	**62.4**	**11.0**	**This work**
Polycrystalline Cu	-1.09	0.1M $KHCO_3$[#]	**81.2**	1.0	ACS Cent. Sci. 2017, 3, 853-859
Polycrystalline Cu	-1.41 -1.44	0.1M $KHCO_3$ 0.1M KCl	**30.1** **69.7**	5.0	J. Chem. Soc. Faraday Trans. 1989, 85, 2309-2326
Polycrystalline Cu	-1.05	0.1M $KHCO_3$	**35.7**	7.0	Energy Environ. Sci. 2012, 5, 7050-7059
Electrochemically cycled Cu	-1	0.1M $CsHCO_3$	**70.6**	13.0	J. Phys. Chem. 2017, C 121, 14191-14203
Prim-shaped Cu	-1.1	0.1M $KHCO_3$	**27.8**	28.6	ACS Catal. 2018, 8, 531-535
Cu nanocubes	-1.1	0.1M $KHCO_3$	**41.1**	5.6	Angew. Chem. Int. Ed. 2016, 55, 5789-5792
KF cycled Cu foil	-1	0.1 M $KHCO_3$[*]	**24.2**	6.5	ChemElectroChem. 2016, 3, 1012-1019
CuO-10	-0.95	0.1M $KHCO_3$	**48.0**	31.5	Nat. Commun. 2018, 9, 925
Cu_2O on Cu	-0.99	0.1M $KHCO_3$	**50.6**	35.0	ACS Catal. 2015, 5, 2814-2821
Cl-Cu_2O-Cu	-1.6	0.1M KCl	**54.7**	6.0	Angew. Chem. Int. Ed. 2015, 54, 14701-14705
Cu_4Zn	-1.05	0.1M $KHCO_3$	**33.2**	8.2	ACS Catal. 2016, 6, 8239-8247
Cu_2O derived Cu	-1	0.1M $KHCO_3$	**48.5**	N.A.	J. Phys. Chem. C 2015, 119, 26875-26882
Cu–Cu_2O/Cu	-0.4	0.1M KCl	**80.0**	11.5	Nat Commun, 2019, 10, 3851
Cu_3N-derived Cu nanowires	-1	0.1M $KHCO_3$	**86.0**	50.6	ChemElectroChem 2019, 6, 2393-2397
n-CuNS	-1.18	0.1M K_2SO_4	**83.2**	58.8	J. Am. Chem. Soc. 2020, 142, 13606-13613
Cu/C-0.4	-0.7	0.1M $KHCO_3$	**91.0**	1.2	Nat Energy, 2020, 5, 623-632

#: 0.1M $KHCO_3$ with 10 mM N-tolylpyridinium chloride.

*: 0.1 M $KHCO_3$ with 4m M KX.

1.3.3 Electrocatalytic Performance of CRR in the Flow Cell

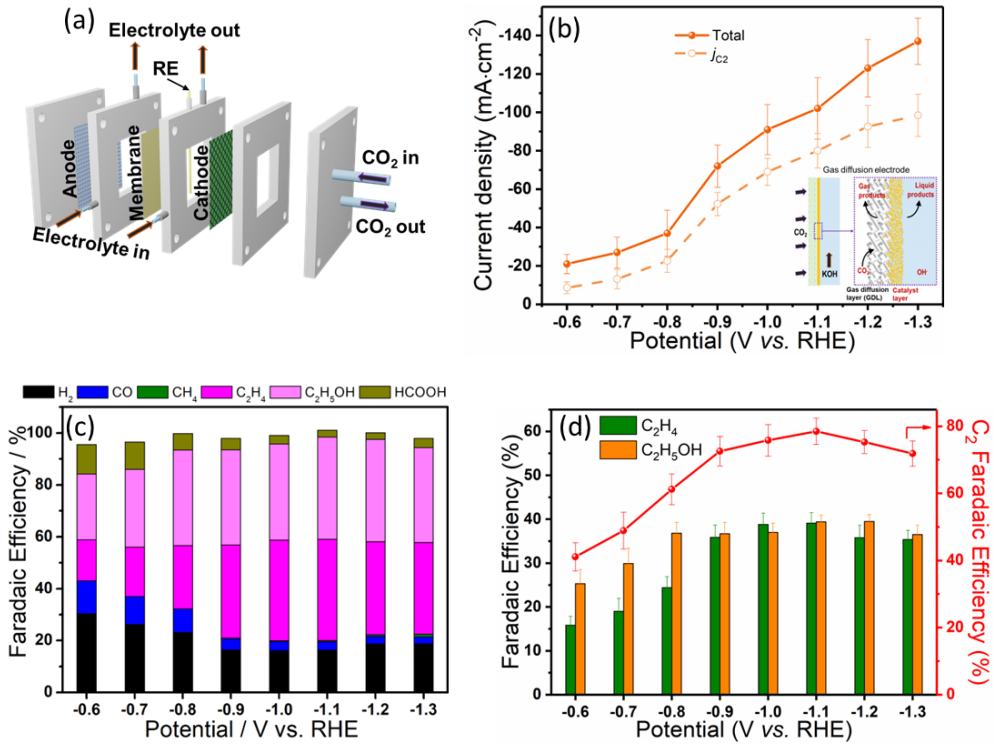

Fig. 1.23. (a) The architecture of the flow cell. (b) The total current densities and partial current densities of C_2 products on Cu_2O/ILGS-*400* in a flow cell. (Inset shows the gas diffusion electrode in electroreduction CO_2). (c) FE of products over Cu_2O/ILGS-*400* in the flow cell at different potentials. (d) FE of C_2 over Cu_2O/ILGS-*400* in a flow cell.

To overcome the low current density of CRR in the H cell, a home-made flow cell was established to enhance the mass transport of CO_2. As shown in Fig. 1.23a, the flow cell system consists of a gas diffusion electrode (GDE), an anion exchange membrane and a Ni foam electrode. As shown in Fig. 1.23b, the gas diffusion layer promotes CO_2 diffusing a short distance to the catalyst surface. At the same time, the current density and partial current density of C_2 products over Cu_2O/ILGS-*400* were significantly improved compared to the H cell. Besides, the FE of CH_4, CO, formate and H_2 obviously decreased obviously and the CH_4 was almost disappeared (Fig. 1.23c). As depicted in Fig. 1.23d, the FE_{C2} on Cu_2O/ILGS-*400* was recorded from -0.6 V to -1.3

V (*vs.* RHE). The total FE_{C2} reached 78.5% (39.1% of FE_{C2H4} and 39.4% of FE_{C2H5OH}) with 123.1 mA cm^{-2} at -1.1V (*vs.* RHE) and the half-cell energy conversion efficiency (EE) of C_2 reached 39.1% (Fig. 1.24). During CO_2 electrolysis stability test, the current density and FE_{C2} were maintained up to 100 h at -1.1 V (*vs.* RHE), as shown in Fig. 1.25. The Cu_2O/ILGS-*400* behaved a comparable performance in flow cell with the best results reported in other works as listed in Table 1.5.

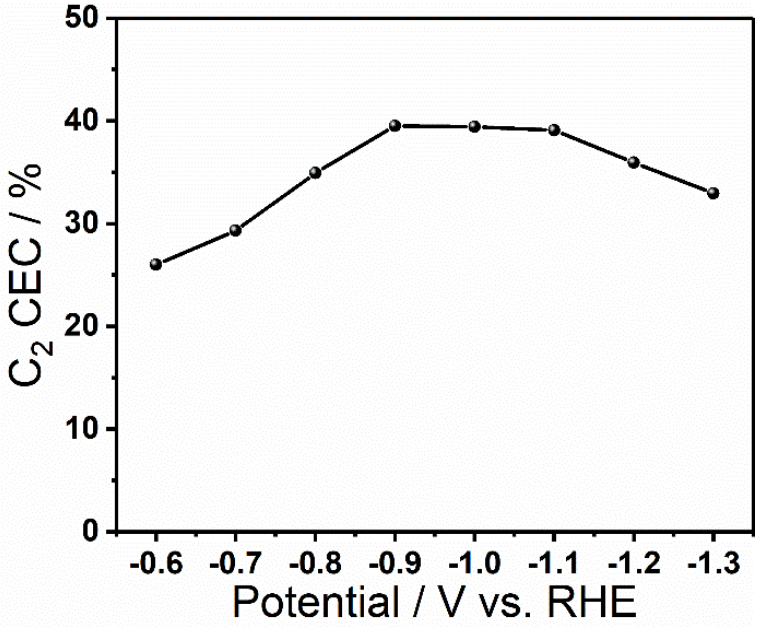

Fig. 1.24. EE of C_2 products over Cu_2O/ILGS-*400* in the flow cell at different potentials.

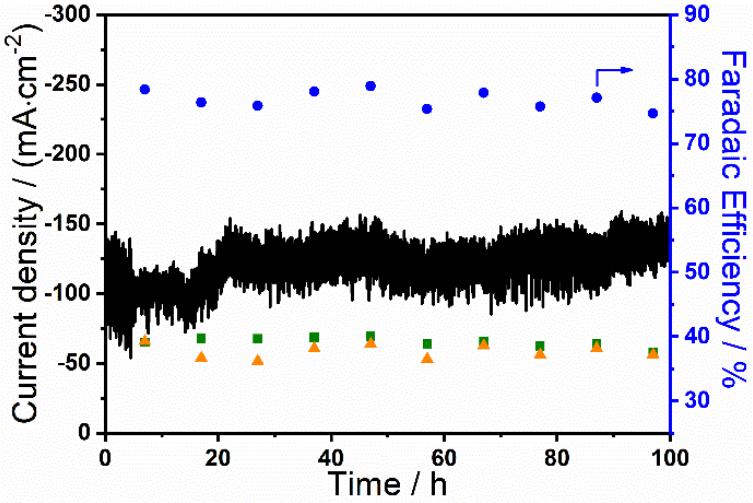

Fig. 1.25. Stability test of Cu_2O/ILGS-*400* at -1.1 V (*vs.* RHE) and the faradaic efficiency for the C_2 products.

Table 1.5. Overview of Cu based catalysts for reduction of CO_2 to C_2 products in the flow cell.

Electrocatalyst	Potential (V *vs.* RHE)	Electrolyte	FE_{C2+} (%)	j_{C2+} (mA cm^{-2})	References
Cu_2O/ILGS-*400*	**-1.1**	**1 M KOH**	**78.5**	**96.6**	**This work**
HKUST-1 derived Cu clusters	-1.07	1 M KOH	45.0	118.0	J. Am. Chem. Soc. 2018, 140, 11378-11386
Electrodeposited Cu_2O	-0.8	1 M KOH	67.0	123.0	ChemElectroChem 2019, 6, 3928-3932
Copper nanodendrites*	-1.4	0.1 M KBr	57.0	96.9	Adv. Energy Mater. 2017, 1602114
OD-Cu gauze	-0.6	1 M KOH	40.0	120.0	J. Mater. Chem. A, 2019, 7, 26285-26292
CuO nanowire derivates	-1.3	1 M KOH	70.0	141.0	J. Mater. Chem. A, 2020, 8, 12418-12423
U-$NCuO_2$	-1.01	1 M $KHCO_3$	59.0	177.0	Angew. Chem. Int. Ed. 2020, 59, 17974-17983
Cu_4O_3	-0.64	0.5 M Cs_2SO_4	60.0	180.0	Adv. Energy Mater. 2019, 9, 1901228
Cu_2O nanoparticles	-0.87	1 M $KHCO_3$	75.5	226.0	Joule 2020, 4, 1104-1120
CuO/ZnO	-0.68	1 M KOH	48.6	97.0	Angew. Chem. Int. Ed. 2019, 58, 15036-15040
CuAg wire	-0.7	1 M KOH	85.0	255.0	J. Am. Chem. Soc. 2018, 140, 5791-5797
CuSn-DAT	-0.8	1 M KOH	79.6	179.0	ACS Catal. 2020, 10, 672-682
Ce(OH)x/Cu/PTFE	-0.7	1 M KOH	76.4	229.2	Nat Commun, 2019, 10, 5814
FeTPP[Cl]/Cu	-0.82	1 M $KHCO_3$	78.6	236.7	Nat Catal, 2020, 3, 75-82
N-C/Cu	-0.68	1 M KOH	93.0	156.0	Nat Energy, 2020, 5, 478-486
F−Cu	-0.89	0.75 M KOH	80.0	1600.0	Nat Catal, 2020, 3, 478-487

After CO_2 electroreduction, the spent Cu_2O/ILGS-*400* was analyzed by SEM and XPS. As shown in Fig. 1.26, the quasi-spherical nanoparticles were maintained, indicating that the morphology of Cu_2O was stable during the CO_2 electroreduction. With further explored from the Cu 2p XPS (Fig. 1.27a) and Auger Cu LMM spectra (Fig. 1.27b), it can be seen that Cu^+ was still the main component after electrocatalysis process. In addition, the *in-situ* surface-enhanced Raman spectra for Cu_2O/ILGS-*400*

were tested at the working conditions with the 785 nm laser (Fig. 1.28) [48, 49]. The Cu^+ signal has no obvious decreases from 5 to 30 min, indicating Cu^+ can be maintained during the reaction. The high-resolution spectra of N 1s and Cl 2p in the XPS of spent catalyst were detected (Fig. 1.27c and d). It was confirmed that the ionic liquid still remains on the surface of catalyst after CO_2 reduction reaction. Therefore, the carbon source of products will not be distracted by the ionic liquid on catalysts during CRR.

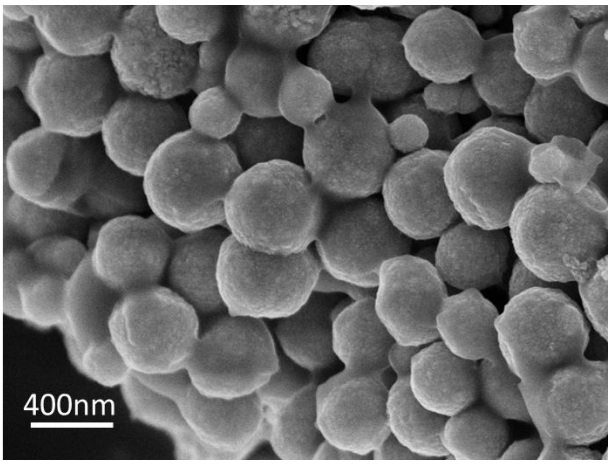

Fig. 1.26. SEM image of Cu_2O/ILGS-*400* after CO_2 electroreduction.

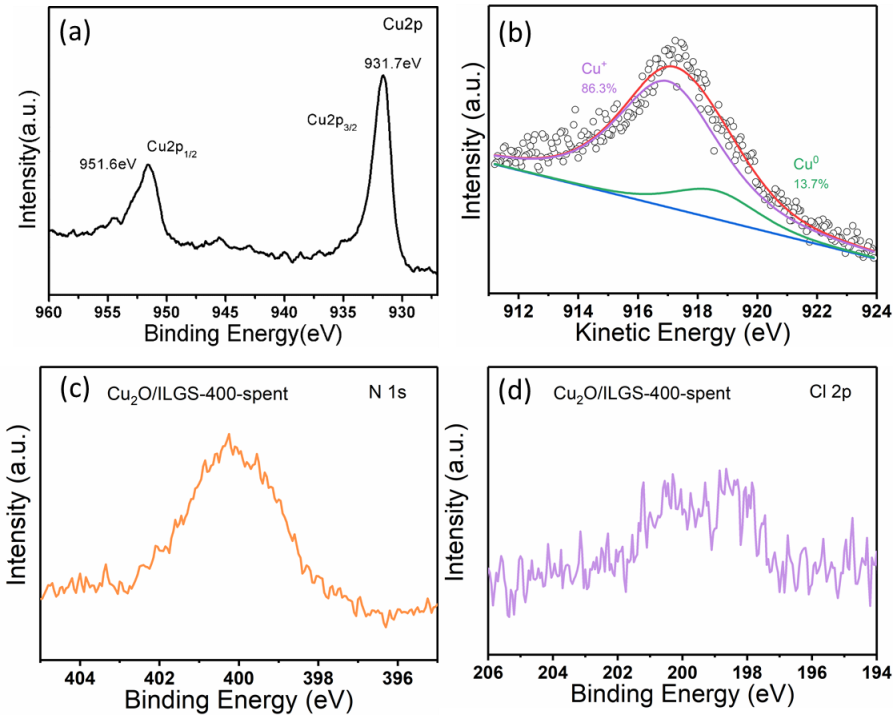

Fig. 1.27. (a) High-resolution Cu 2p spectrum, (b) Cu LMM Auger spectrum, (c) N 1s and (d) Cl 2p of Cu_2O/ILGS-*400* after CO_2 electroreduction.

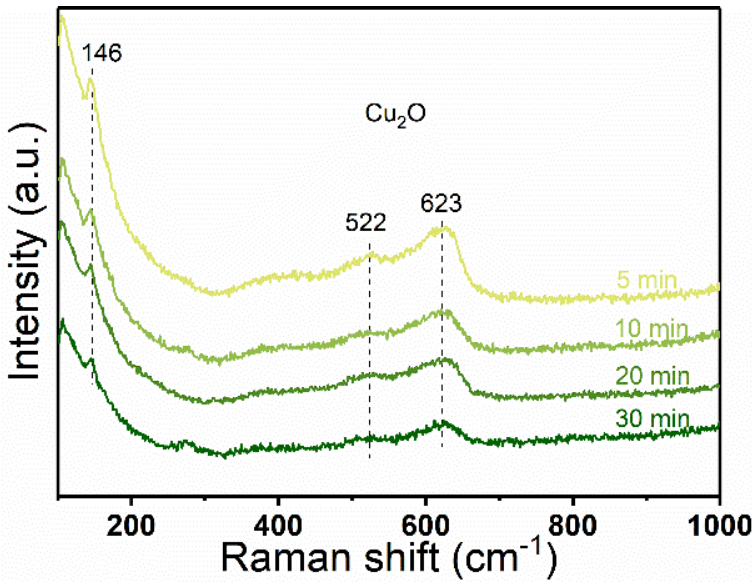

Fig. 1.28. The *in-situ* surface-enhanced Raman spectra for Cu_2O/ILGS-*400* as a function of reaction time at -1.15V *vs.* RHE in 1 M KOH with the 785 nm laser.

1.3.4 Discussion of Electrocatalysis Mechanism

The activity and selectivity of CRR were further discussed as follows. Firstly, the electrochemically active surface area of Cu_2O/ILGS-*x* was analyzed by single-sweep polarography (Fig. 1.29). It can be seen that Cu_2O/ILGS-*400* had the largest electrochemical active surface area among all the catalysts according to the measured double-layer capacitance, proving more catalytic active sites on Cu_2O/ILGS-*400*. Then, the CO_2 capture capacity of Cu_2O/ILGS-*400* and Cu_2O/ILGS was compared in Fig. 1.30a. Obviously, the former material had a much higher CO_2 adsorption capacity, which was further converted to $CO_2^{\bullet-}$ moieties, the first step of CRR [50]. With regards to this, the capacity of binding affinity of $CO_2^{\bullet-}$ was simulate by the overpotential of adsorption SO_4^{2-} on different materials (Fig. 1.30b) [51]. Compared with Cu_2O/ILGS, Cu_2O/ILGS-*400* showed a smaller overpotential of SO_4^{2-} adsorption, meaning a stronger binding of $CO_2^{\bullet-}$ intermediates. These $CO_2^{\bullet-}$ intermediates will be hydrogenated to CO*, the key intermediate to C_2 products [52]. It is generally agreed that strong adsorption of CO* is conducive to the formation of C_2 products [53].

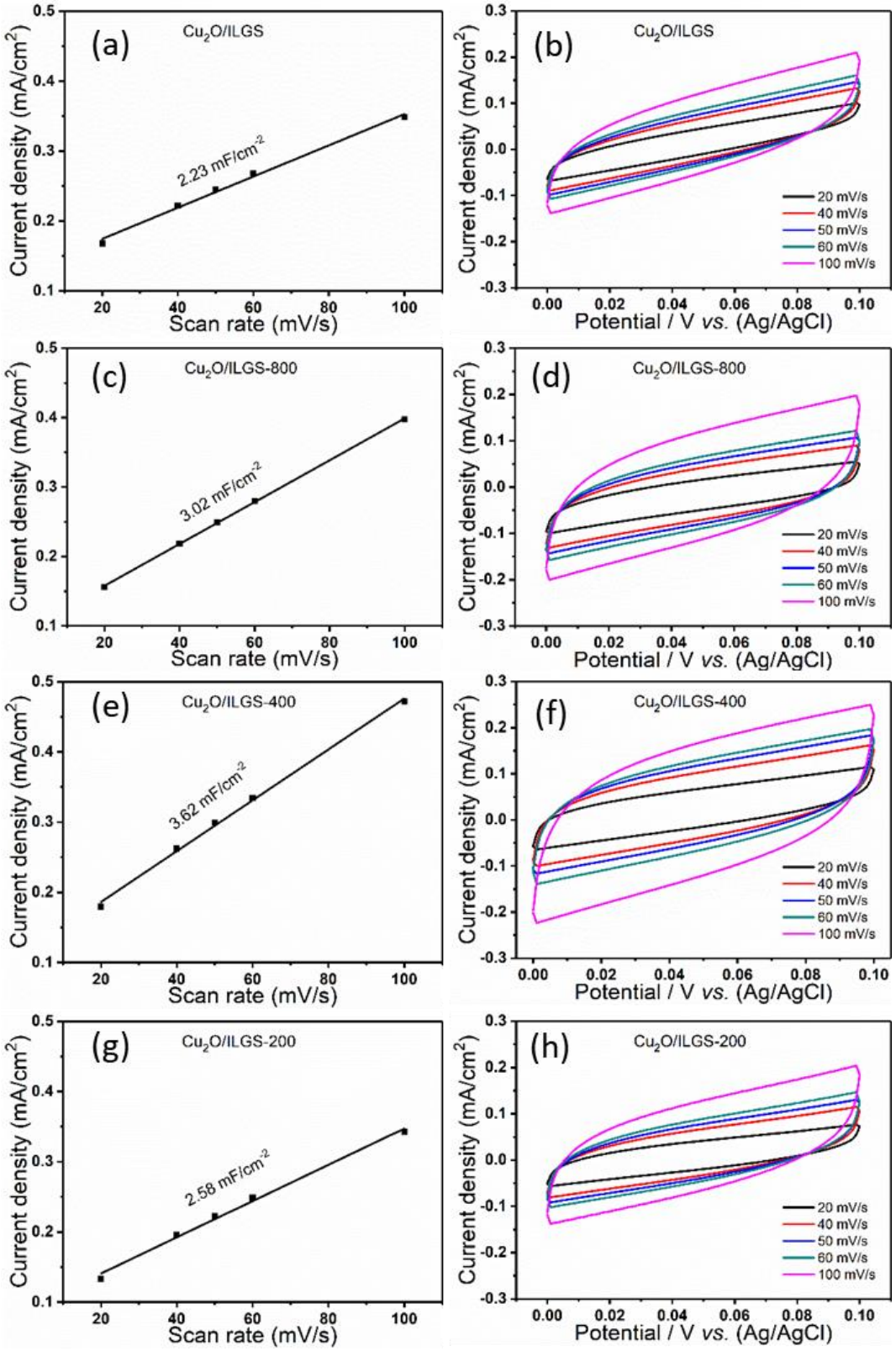

Fig. 1.29. The charging current density differences plotted against the scan rates (a, c, e, g) and the corresponding cyclic voltammetry at different scan rates of Cu_2O/ILGS-*x* (b, d, f, h).

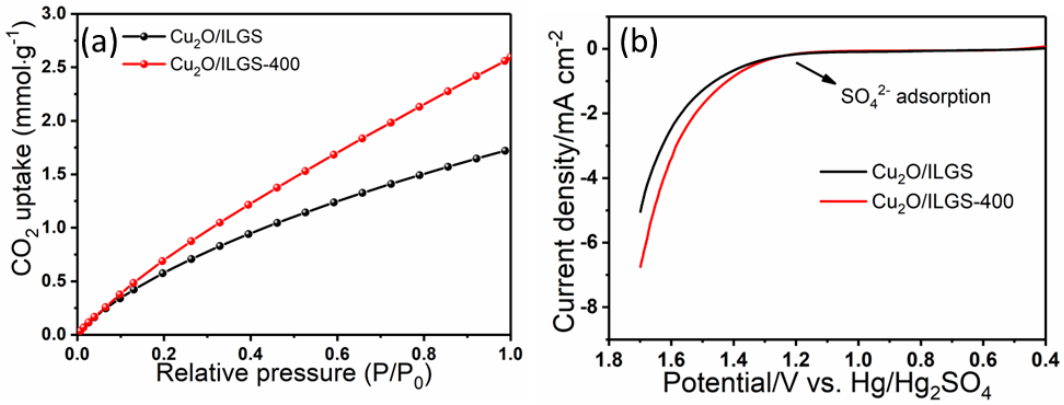

Fig. 1.30. (a) CO_2 uptake isotherms of Cu_2O/ILGS-*x* at 298.15K. (b) Adsorption of sulfate on Cu_2O/ILGS-*x* with a 0.1 M sulfuric acid solution by LSVs. Data were collected by a platinum mesh as the counter electrode, and an Hg/Hg_2SO_4 as the reference electrode; sulfate adsorption scans were performed between 0.4 V and 1.7 V *vs.* Hg/Hg_2SO_4, scan rate was 10 mV s^{-1}. The catalyst loading was 1 ± 0.1 mg cm^{-2}.

The *in-situ* surface enhanced Raman spectroscopy (SERS) was studied to explore the surface species on Cu_2O/ILGS, Cu_2O/ILGS-*400* during the reaction to reveal the interactions between Cu species and the reaction intermediates. The presence of adsorbed *CO peak was detected at 2065 cm^{-1} in Raman spectra (Fig. 1.31a and b) [54, 55]. The intensity of *CO peak in Cu_2O/ILGS-*400* was stronger than Cu_2O/ILGS, which was consistent with the results in the performance (Fig. 1.32). In addition, the adsorbed CO_2 peak at 530 cm^{-1} was also obvious. It is believed that Cu_2O/ILGS-*400* is outstanding for the adsorption of $*CO_2$ and *CO. Meanwhile, the adsorption energies (ΔE_{ads}) of CO* on the oxygen vacancies Cu_2O (111) surface (Cu_2O-O_V) and pure Cu_2O (111) surface structures were also evaluated by DFT calculation. As shown in Fig. 1.33 and Table 1.6, the ΔE_{ads} of CO* on Cu_2O-O_V (-1.56 eV) was much higher than Cu_2O (-1.31 eV), suggesting a stronger adsorption of CO* on Cu_2O-O_V, which is consistent with SERS results.

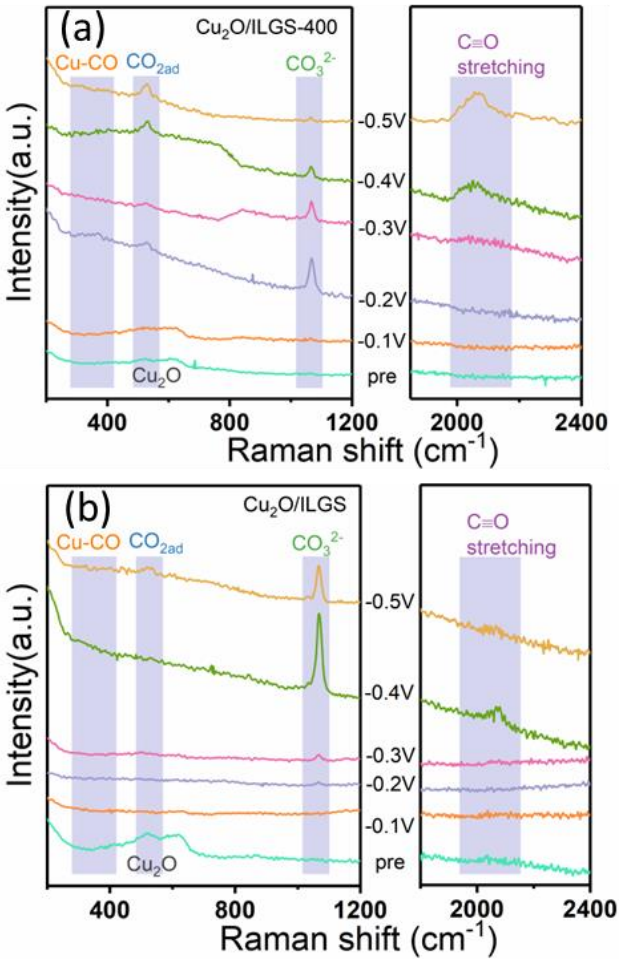

Fig. 1.31. The *in-situ* surface-enhanced Raman spectra for (a) Cu_2O/ILGS-*400* and (b) Cu_2O/ILGS at various potentials (*vs.* RHE) during CRR.

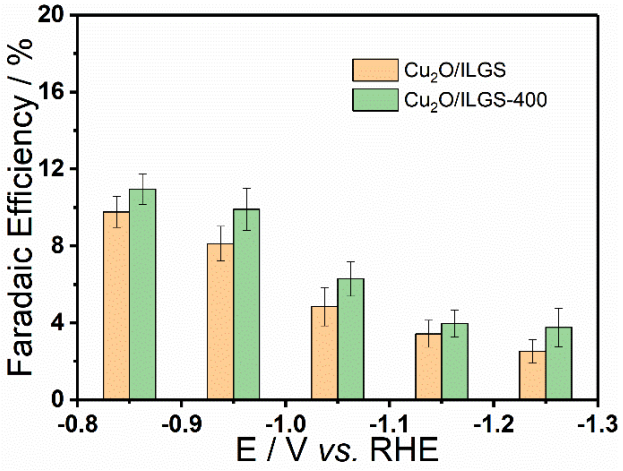

Fig. 1.32 The comparison for the faradaic efficiency of CO on Cu_2O/ILGS and Cu_2O/ILGS-*400* at various applied potentials.

Fig. 1.33. CO* on the catalyst surfaces (The circle in the center of yellow copper atoms represents the oxygen vacancy).

Table 1.6. The calculated energetic data for catalyst surfaces and the adsorption energies (ΔE_{ads}) of CRR intermediates (*CO).

Model	$E_{slab+adsorption}$ /eV	E_{slab} /eV	E_{ads} /eV
Oxygen vacancy	-567.16606	-550.80079	-1.564077
No oxygen vacancy	-573.0157	-556.89959	-1.314917

In detail, the elementary reactions of CO_2-to-C_2 was further explored by DFT method. Previous reports revealed that the reaction of dimer CO* intermediates hydrogenated to OC-COH* was the key step for the formation of C_2 products [16]. Herein, we proposed a simplified model of reaction way from CO_2 to C_2 (Fig. 1.34). The reaction of $2CO^* + H^+ \rightarrow OC\text{-}COH^*$ was chosen as the elementary step, which was calculated on Cu_2O-O_V and Cu_2O respectively (Fig. 1.35, Table 1.7). For Cu_2O-O_V, the Gibbs free energy of OC-COH* formation was 1.36 eV, which is much lower than that on Cu_2O (3.38 eV). This suggested that C_2 was favorably generated on the surface of Cu_2O-O_V, which was consistent well with the experimental results. To sum up, due to the abundant oxygen vacancies on Cu_2O-O_V, the surface coverage of CO* on copper was increased to speed up the reaction of $2CO^* + H^+ \rightarrow OC\text{-}COH^*$, resulting in the highest selectivity C_2 production on Cu_2O/ILGS-*400*.

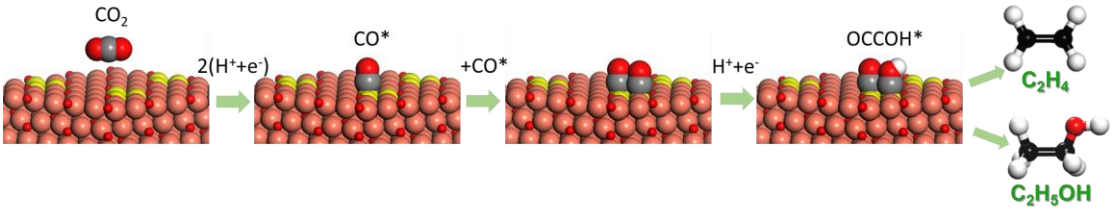

Fig. 1.34. The key reaction pathways for CO_2 to C_2.

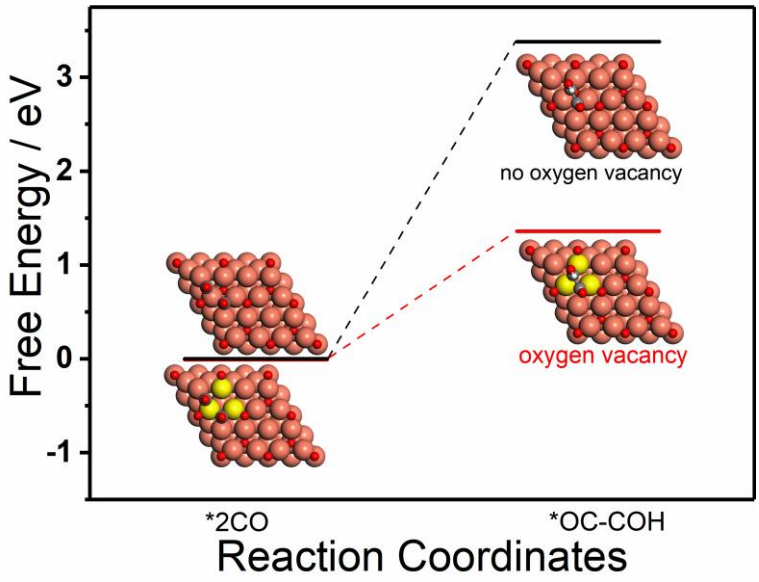

Fig. 1.35. The free energy differences of OC-COH* formation and the optimized adsorption structures of CO* and OC-COH* on Cu_2O-O_V and Cu_2O.

Table 1.7. The calculated energetic data for all the surface species.

Model	**Adsorbate**	**E_{DFT}/eV**	**$\Delta G_{correction}$/eV**	**Gibbs free energy/eV**
Oxygen vacancy	*2CO	-582.50484	0.24323	-582.26161
Oxygen vacancy	*OC-COH	-584.95858	0.65495	-584.30363
No oxygen vacancy	*2CO	-590.75427	0.27355	-590.48072
No oxygen vacancy	*OC-COH	-591.13018	0.62520	-590.50498

1.4 Conclusion

In summary, the quasi-spherical Cu_2O with rough surface and abundant oxygen vacancies were simply prepared by a wet chemical method in assistant with [Omim]Cl assisting. On the one hand, $[Omim]^+$ played a key role as like-surfactant in inhibiting the growth of crystal planes, thus getting a special quasi-spherical morphology of Cu_2O with rough surfaces. On the other hand, due to the hydrogen bonding between $[Omim]^+$ and Cl^-, more Cl^- were adsorbed on the surface of Cu_2O, thus promoting the formation of oxygen vacancies by coordinating with Cu^+. Under the synergistic effects of $[Omim]^+$ and Cl^-, the novel quasi-spherical Cu_2O with abundant oxygen vacancies were prepared and *in-situ* dispersed on a home-made graphite nanosheets to form a series of Cu_2O/ILGS-*x* composites, which behaved excellent catalytic performance towards CO_2 electroreduction to C_2 products. By adjusting the content of [Omim]Cl, the optimum catalyst of Cu_2O/ILGS-*400* performed the best performance with a faradic efficiency of 62.4% for C_2 products at -1.15 V (*vs.* RHE) in an H-cell with 0.1 M $KHCO_3$ as electrolyte. By using 1 M KOH as electrolyte in a flow cell, the faradic efficiency of C_2 products was raised to 78.5% ± 2% with current density of 123.1 mA cm^{-2} at −1.1 V (*vs.* RHE). In a long durability test for 100 hours, the catalytic performance of C_2 had no obvious degradation. *In situ* surface-enhanced Raman spectroscopy and density functional theory calculations proved the special structure of Cu_2O strengthened the adsorption of intermediates ($CO_2^{\bullet-}$, CO*) and the following C–C coupling reaction, thus remarkably promoting the formation of C_2 products. This work may open a new horizon towards controllable synthesis of metal oxides using ionic liquids as bifunctional structure-directing agent for CO_2 reduction and other electrocatalysis process.

References

[1] M. He, Y. Sun, B. Han, Green carbon science: scientific basis for integrating carbon resource processing, utilization, and recycling, *Angew. Chem. Int. Ed.*, **2013**, *52*, 9620-

9633.

[2] M.B. Ross, P. De Luna, Y. Li, C.-T. Dinh, D. Kim, P. Yang, E.H. Sargent, Designing materials for electrochemical carbon dioxide recycling, *Nat. Catal.*, **2019**, *2*, 648-658.

[3] A. Mustafa, B.G. Lougou, Y. Shuai, Z. Wang, H. Tan, Current technology development for CO_2 utilization into solar fuels and chemicals: A review, *J. Energy Chem.*, **2020**, *49*, 96-123.

[4] X. Wang, Z. Wang, F.P. García de Arquer, C.-T. Dinh, A. Ozden, Y.C. Li, D.-H. Nam, J. Li, Y.-S. Liu, J. Wicks, Z. Chen, M. Chi, B. Chen, Y. Wang, J. Tam, J.Y. Howe, A. Proppe, P. Todorović, F. Li, T.-T. Zhuang, C.M. Gabardo, A.R. Kirmani, C. McCallum, S.-F. Hung, Y. Lum, M. Luo, Y. Min, A. Xu, C.P. O'Brien, B. Stephen, B. Sun, A.H. Ip, L.J. Richter, S.O. Kelley, D. Sinton, E.H. Sargent, Efficient electrically powered CO_2-to-ethanol via suppression of deoxygenation, *Nature Energy*, **2020**, *5*, 478-486.

[5] O.S. Bushuyev, P. De Luna, C.T. Dinh, L. Tao, G. Saur, J. van de Lagemaat, S.O. Kelley, E.H. Sargent, What should we make with CO_2 and how can we make it?, *Joule*, **2018**, *2*, 825-832.

[6] C. Chen, X. Sun, X. Yan, Y. Wu, H. Liu, Q. Zhu, B.B.A. Bediako, B. Han, Boosting CO_2 electroreduction on N,P-Co-doped carbon aerogels, *Angew. Chem. Int. Ed.*, **2020**, *59*, 11123-11129.

[7] Q. Gong, P. Ding, M. Xu, X. Zhu, M. Wang, J. Deng, Q. Ma, N. Han, Y. Zhu, J. Lu, Z. Feng, Y. Li, W. Zhou, Y. Li, Structural defects on converted bismuth oxide nanotubes enable highly active electrocatalysis of carbon dioxide reduction, *Nat. Commun.*, **2019**, *10*, 2807.

[8] X. Sun, X. Kang, Q. Zhu, J. Ma, G. Yang, Z. Liu, B. Han, Very highly efficient reduction of CO_2 to CH_4 using metal-free N-doped carbon electrodes, *Chem. Sci.*, **2016**, *7*, 2883-2887.

[9] H. Ning, D. Guo, X. Wang, Z. Tan, W. Wang, Z. Yang, L. Li, Q. Zhao, J. Hao, M. Wu, Efficient CO_2 electroreduction over N-doped hieratically porous carbon derived from petroleum pitch, *J. Energy Chem.*, **2021**, *56*, 113-120.

[10] W. Ma, M. Xie, S. Xie, L. Wei, Y. Cai, Q. Zhang, Y. Wang, Nickel and indium core-shell co-catalysts loaded silicon nanowire arrays for efficient photoelectrocatalytic reduction of CO_2 to formate, *J. Energy Chem.*, **2021**, *54*, 422-428.

[11] B. Zhang, J. Zhang, M. Hua, Q. Wan, Z. Su, X. Tan, L. Liu, F. Zhang, G. Chen, D. Tan, X. Cheng, B. Han, L. Zheng, G. Mo, Highly electrocatalytic ethylene production from CO_2 on nanodefective Cu nanosheets, *J. Am. Chem. Soc.*, **2020**, *142*, 13606-13613.

[12] P. Iyengar, M.J. Kolb, J.R. Pankhurst, F. Calle-Vallejo, R. Buonsanti, Elucidating the facet-dependent selectivity for CO_2 electroreduction to ethanol of Cu–Ag tandem catalysts, *ACS Catal.*, **2021**, *11*, 4456-4463.

[13] W. Ma, S. Xie, T. Liu, Q. Fan, J. Ye, F. Sun, Z. Jiang, Q. Zhang, J. Cheng, Y. Wang, Electrocatalytic reduction of CO_2 to ethylene and ethanol through hydrogen–assisted C–C coupling over fluorine-modified copper, *Nat. Catal.*, **2020**, *3*, 478-487.

[14] Z. Gu, H. Shen, L. Shang, X. Lv, L. Qian, G. Zheng, Nanostructured copper-based electrocatalysts for CO_2 reduction, *Small Methods*, **2018**, *2*, 1800121.

[15] H. Li, T. Liu, P. Wei, L. Lin, D. Gao, G. Wang, X. Bao, High-rate CO_2 electroreduction to C_{2+} products over a copper-copper iodide catalyst, *Angew. Chem. Int. Ed.*, **2021**, *133*, 14450-14454.

[16] P. De Luna, R. Quintero-Bermudez, C.-T. Dinh, M.B. Ross, O.S. Bushuyev, P. Todorović, T. Regier, S.O. Kelley, P. Yang, E.H. Sargent, Catalyst electro-redeposition controls morphology and oxidation state for selective carbon dioxide reduction, *Nat. Catal.*, **2018**, *1*, 103-110.

[17] C. Kim, F. Dionigi, V. Beermann, X. Wang, T. Moller, P. Strasser, Alloy nanocatalysts for the electrochemical oxygen reduction (ORR) and the direct electrochemical carbon dioxide reduction reaction (CO_2 RR), *Adv. Mater.*, **2019**, *31*, 1805617.

[18] Y. Zhou, F. Che, M. Liu, C. Zou, Z. Liang, P. De Luna, H. Yuan, J. Li, Z. Wang, H. Xie, H. Li, P. Chen, E. Bladt, R. Quintero-Bermudez, T.K. Sham, S. Bals, J. Hofkens, D. Sinton, G. Chen, E.H. Sargent, Dopant-induced electron localization drives CO_2

reduction to C_2 hydrocarbons, *Nat. Chem.*, **2018**, *10*, 974-980.

[19] F. Li, A. Thevenon, A. Rosas-Hernandez, Z. Wang, Y. Li, C.M. Gabardo, A. Ozden, C.T. Dinh, J. Li, Y. Wang, J.P. Edwards, Y. Xu, C. McCallum, L. Tao, Z.Q. Liang, M. Luo, X. Wang, H. Li, C.P. O'Brien, C.S. Tan, D.H. Nam, R. Quintero-Bermudez, T.T. Zhuang, Y.C. Li, Z. Han, R.D. Britt, D. Sinton, T. Agapie, J.C. Peters, E.H. Sargent, Molecular tuning of CO_2-to-ethylene conversion, *Nature*, **2020**, *577*, 509-513.

[20] J. Kim, W. Choi, J.W. Park, C. Kim, M. Kim, H. Song, Branched copper oxide nanoparticles induce highly selective ethylene production by electrochemical carbon dioxide reduction, *J. Am. Chem. Soc.*, **2019**, *141*, 6986-6994.

[21] G. Wang, Z. Jin, T. Zhao, Oxygen-vacancy-rich hydrated bimetallic chloride for supercapacitor cathode with remarkable enhanced performance, *Int. J. Energ. Res.*, **2020**, *45*, 2899-2911.

[22] S. Wang, X. Ding, N. Yang, G. Zhan, X. Zhang, G. Dong, L. Zhang, H. Chen, Insight into the effect of bromine on facet-dependent surface oxygen vacancies construction and stabilization of Bi_2MoO_6 for efficient photocatalytic NO removal, *Appl. Catal. B: Environ.*, **2020**, *265*, 118585.

[23] Y. Jin, J. Long, X. Ma, T. Zhou, Z. Zhang, H. Lin, J. Long, X. Wang, Synthesis of caged iodine-modified ZnO nanomaterials and study on their visible light photocatalytic antibacterial properties, *Appl. Catal. B: Environ.*, **2019**, *256*, 117873.

[24] X. Han, F. Liao, Y. Zhang, Z. Yuan, H. Chen, C. Xu, Rapid and template-free synthesis of Cu_2O truncated octahedra using glucose as green reducing agent, *Mater. Lett.*, **2018**, *210*, 31-34.

[25] L. Yu, G. Li, X. Zhang, X. Ba, G. Shi, Y. Li, P.K. Wong, J.C. Yu, Y. Yu, Enhanced activity and stability of carbon-decorated cuprous oxide mesoporous nanorods for CO_2 reduction in artificial photosynthesis, *ACS Catal.*, **2016**, *6*, 6444-6454.

[26] P. Migowski, G. Machado, S.R. Texeira, M.C. Alves, J. Morais, A. Traverse, J. Dupont, Synthesis and characterization of nickel nanoparticles dispersed in imidazolium ionic liquids, *Phys. Chem. Chem. Phys.*, **2007**, *9*, 4814-4821.

[27] N. Liu, F. Luo, H. Wu, Y. Liu, C. Zhang, J. Chen, One-step ionic-liquid-assisted electrochemical synthesis of ionic-liquid-functionalized graphene sheets directly from graphite, *Adv. Funct. Mater.*, **2008**, *18*, 1518-1525.

[28] Y.N. Chouryal, R.K. Sharma, D. Acharjee, T. Ganguly, A. Pandey, P. Ghosh, Influence of ionic liquids and concentration of red phosphorous on luminescent Cu_3P nanocrystals, *J. Chem. Sci.*, **2019**, *131*, 93.

[29] H. Ning, W. Wang, Q. Mao, S. Zheng, Z. Yang, Q. Zhao, M. Wu, Catalytic electroreduction of CO_2 to C_2H_4 using Cu_2O supported on 1-Octyl-3-methylimidazole functionalized graphite sheets, *Acta Phys. -Chim. Sin.*, **2018**, *34*, 938-944.

[30] V. Wang, N. Xu, J.-C. Liu, G. Tang, W.-T. Geng, VASPKIT: A user-friendly interface facilitating high-throughput computing and analysis using VASP code, *Comput. Phys. Commun.*, **2021**, *267*, 108033.

[31] W. Wang, H. Ning, Z. Yang, Z. Feng, J. Wang, X. Wang, Q. Mao, W. Wu, Q. Zhao, H. Hu, Y. Song, M. Wu, Interface-induced controllable synthesis of Cu_2O nanocubes for electroreduction CO_2 to C_2H_4, *Electrochim. Acta*, **2019**, *306*, 360-365.

[32] W. Geng, W. Li, L. Liu, J. Liu, L. Liu, X. Kong, Facile assembly of Cu-Cu_2O/N-reduced graphene oxide nanocomposites for efficient synthesis of 2-methylfuran, *Fuel*, **2020**, *259*, 116267.

[33] S.Y. Lee, H. Jung, N.K. Kim, H.S. Oh, B.K. Min, Y.J. Hwang, Mixed copper states in anodized Cu electrocatalyst for stable and selective ethylene production from CO_2 reduction, *J. Am. Chem. Soc.*, **2018**, *140*, 8681-8689.

[34] R.R. Gandhi, S. Senthil, R. Rajappan, K. Ramesh, M. Sundrarajan, [BMIM]BF_4, [EMIM]BF_4 and [BMIM]PF_6 ionic liquids assisted synthesis of MgO nanoparticles: controlled size, much morphology and antibacterial properties, *J. Bionanosci.*, **2015**, *9*, 28-34.

[35] L. Yung, H. Ma, X. Wang, K. Yoon, R. Wang, B.S. Hsiao, B. Chu, Fabrication of thin-film nanofibrous composite membranes by interfacial polymerization using ionic liquids as additives, *J. Membrane Sci.*, **2010**, *365*, 52-58.

[36] Z. Cao, J.S. Derrick, J. Xu, R. Gao, M. Gong, E.M. Nichols, P.T. Smith, X. Liu, X. Wen, C. Coperet, C.J. Chang, Chelating N-heterocyclic carbene ligands enable tuning of electrocatalytic CO_2 reduction to formate and carbon monoxide: surface organometallic chemistry, *Angew. Chem. Int. Ed.*, **2018**, *57*, 4981-4985.

[37] S.H. Ye, X.J. He, L.X. Ding, Z.W. Pan, Y.X. Tong, M. Wu, G.R. Li, Cu_2O template synthesis of high-performance PtCu alloy yolk-shell cube catalysts for direct methanol fuel cells, *Chem. Commun.*, **2014**, *50*, 12337-12340.

[38] G. Yan, Y. Lian, Y. Gu, C. Yang, H. Sun, Q. Mu, Q. Li, W. Zhu, X. Zheng, M. Chen, J. Zhu, Z. Deng, Y. Peng, Phase and morphology transformation of MnO_2 induced by ionic liquids toward efficient water oxidation, *ACS Catal.*, **2018**, 10137-10147.

[39] S. Ye, J. Wang, J. Hu, Z. Chen, L. Zheng, Y. Fu, Y. Lei, X. Ren, C. He, Q. Zhang, J. Liu, Electrochemical construction of low-crystalline CoOOH nanosheets with short-range ordered grains to improve oxygen evolution activity, *ACS Catal.*, **2021**, *11*, 6104-6112.

[40] X. Kang, X. Sun, B. Han, Synthesis of functional nanomaterials in ionic liquids, *Adv. Mater.*, **2016**, *28*, 1011-1030.

[41] M. Singh, D. Jampaiah, A.E. Kandjani, Y.M. Sabri, E. Della Gaspera, P. Reineck, M. Judd, J. Langley, N. Cox, J. van Embden, E.L.H. Mayes, B.C. Gibson, S.K. Bhargava, R. Ramanathan, V. Bansal, Oxygen-deficient photostable Cu_2O for enhanced visible light photocatalytic activity, *Nanoscale*, **2018**, *10*, 6039-6050.

[42] R. Yang, X. Lu, X. Huang, Z. Chen, X. Zhang, M. Xu, Q. Song, L. Zhu, Bi-component Cu_2O–CuCl composites with tunable oxygen vacancies and enhanced photocatalytic properties, *Appl. Catal. B: Environ.*, **2015**, *170-171*, 225-232.

[43] L. Lu, X. Xu, J. Yan, F.N. Shi, Y. Huo, Oxygen vacancy rich Cu_2O based composite material with nitrogen doped carbon as matrix for photocatalytic H_2 production and organic pollutant removal, *Dalton T.*, **2018**, *47*, 2031-2038.

[44] W. Guo, S. Liu, X. Tan, R. Wu, X. Yan, C. Chen, Q. Zhu, L. Zheng, J. Ma, J. Zhang, Y. Huang, X. Sun, B. Han, Highly efficient CO_2 electroreduction to methanol through

atomically dispersed Sn coupled with defective CuO catalysts, *Angew. Chem. Int. Ed.*, **2021**, *60*, 21979-21987.

[45] D. Gustinčič, A. Kokalj, DFT study of azole corrosion inhibitors on Cu_2O model of oxidized copper surfaces: I. molecule-surface and Cl-surface bonding, *Metals*, **2018**, *8*, 310.

[46] Engelbert Redel, Ralf Thomann, C. Janiak, First correlation of nanoparticle size-dependent formation with the ionic liquid anion molecular volume, *Inorg. Chem.*, **2008**, *47*, 14−16.

[47] J. Sun, N. Guo, Z. Shao, K. Huang, Y. Li, F. He, Q. Wang, A facile strategy to construct amorphous spinel-based electrocatalysts with massive oxygen vacancies using ionic liquid dopant, *Adv. Energy Mater.*, **2018**, *8*, 1800980.

[48] P.P. Yang, X.L. Zhang, F.Y. Gao, Y.R. Zheng, Z.Z. Niu, X. Yu, R. Liu, Z.Z. Wu, S. Qin, L.P. Chi, Y. Duan, T. Ma, X.S. Zheng, J.F. Zhu, H.J. Wang, M.R. Gao, S.H. Yu, Protecting copper oxidation state via intermediate confinement for selective CO_2 electroreduction to C_{2+} fuels, *J. Am. Chem. Soc.*, **2020**, *142*, 6400-6408.

[49] M. Balkanski, M.A. Nusimovici, J. Reydellet, First order Raman spectrum of Cu_2O, *Solid State Commun.*, **1969**, *7*, 815-818.

[50] Y. Huo, X. Peng, X. Liu, H. Li, J. Luo, High selectivity toward C_2H_4 production over Cu particles supported by butterfly-wing-derived carbon frameworks, *ACS Appl. Mater. Inter.*, **2018**, *10*, 12618-12625.

[51] D. Yang, Q. Zhu, X. Sun, C. Chen, L. Lu, W. Guo, Z. Liu, B. Han, Nanoporous Cu/Ni oxide composites: efficient catalysts for electrochemical reduction of CO_2 in aqueous electrolytes, *Green Chem.*, **2018**, *20*, 3705-3710.

[52] Z. Gu, N. Yang, P. Han, M. Kuang, B. Mei, Z. Jiang, J. Zhong, L. Li, G. Zheng, Oxygen vacancy tuning toward efficient electrocatalytic CO_2 reduction to C_2H_4, *Small Methods*, **2018**, *3*, 1800449.

[53] C. Chen, X. Yan, S. Liu, Y. Wu, Q. Wan, X. Sun, Q. Zhu, H. Liu, J. Ma, L. Zheng, H. Wu, B. Han, Highly efficient electroreduction of CO_2 to C_{2+} alcohols on

heterogeneous dual active sites, *Angew. Chem. Int. Ed.*, **2020**, *59*, 16459-16464.

[54] X. Yan, C. Chen, Y. Wu, S. Liu, Y. Chen, R. Feng, J. Zhang, B. Han, Efficient electroreduction of CO_2 to C_{2+} products on CeO_2 modified CuO, *Chem. Sci.*, **2021**, *12*, 6638-6645.

[55] C. Chen, X. Yan, Y. Wu, S. Liu, X. Sun, Q. Zhu, R. Feng, T. Wu, Q. Qian, H. Liu, L. Zheng, J. Zhang, B. Han, The *in situ* study of surface species and structures of oxide-derived copper catalysts for electrochemical CO_2 reduction, *Chem. Sci.*, **2021**, *12*, 5938-5943.

Chapter 2

Carburized In_2O_3 nanorods endow CO_2 electroreduction to formate at 1 A cm^{-2}

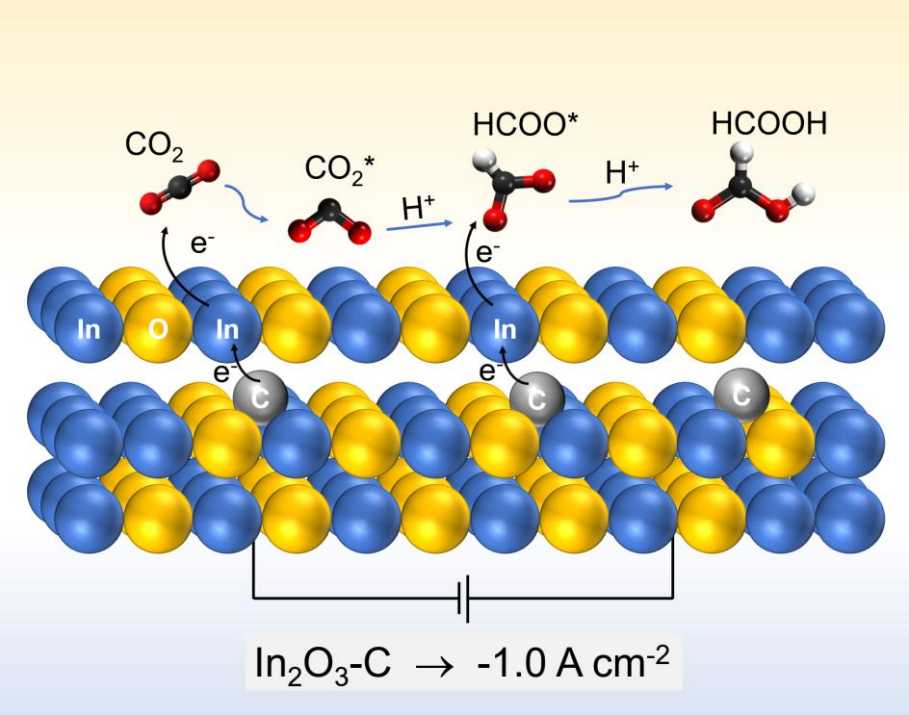

A high faradaic efficiency above 80% toward CO_2-to-formate was achieved at -1 A cm^{-2} on the carburized In_2O_3 nanorods, where the carbon atoms penetrated into the sublayer of In_2O_3 increased the electron density of In and facilitate the exposure of active sites simultaneously.

Abstract

The double high index of current density and Faradaic efficiency in carbon dioxide electroreduction is a great challenge. In this Chapter, we synthesized carburized indium oxide nanorods (In_2O_3-C) by pyrolysis of MOFs precursor [MIL-68 (In)]. The electronic structure of In was regulated and the localization of negative charges was increased on the surface of In_2O_3-C catalyst, resulting in high Faradaic efficiency of 97.2% at -1.0 V *vs.* RHE and above 90% in a wide potential range of 500 mV. Furthermore, it reached a current density of -1.0 $A \cdot cm^{-2}$ in the flow cell for producing formate efficiently. The complete reaction path from CO_2 to formate on In_2O_3-C was in-situ investigated by attenuated total reflection surface-enhanced infrared adsorption spectroscopy and 2D/3D surface-enhanced Raman spectroscopy.

Keyword: Interstitial carbon; In_2O_3; CO_2 electroreduction; Formate; Metal-carbon interaction

2.1 Introduction

Electrochemical reduction of CO_2 (CRR) to valuable chemicals and fuels, powered by renewable electricity, is an attractive strategy for human sustainable development [1, 2]. Among commodity chemicals, formate is noted for its nontoxicity, safety, transportability, and broad applications, which is also a hydrogen carrier for transportation [3-6]. Nowadays, developing highly activity electrocatalysts is an urgent but full of challenge issue for the real application of CRR.

Recently published works have proposed that Indium-based catalysts have good selectivity toward formate [7, 8]. When the porous In_2O_3 nanobelts were supported on reduced graphene oxide as a catalyst for CRR, a faradaic efficiency (FE) of 84.6% at −1.2 V *vs.* RHE can be achieved at room temperature [9]. A crystalline-In/amorphous-In_2O_{3-x} heterostructure was also reported with an FE of ~89.2% toward formate [10]. Assistant with the defects strategy, a high FE of up to 93% was obtained on the indium/indium oxide [11]. Beyond the FE, the current density is also a desirable factor for CRR to formate, maintaining the high selectivity as well. However, most partial current densities of formate in previous studies were less than 200 mA cm^{-2}, which is insufficient to meet basic industrial demands [12]. The electrocatalysts that operate at high current densities will reduce the capital costs and further decrease the capital contribution to the industrial prospect [13].

One of the promising ways to improve the activity of metal catalysts is by regulating their electronic structures, such as heteroatom doping with nonmetallic elements [14-16]. For example, the pyridinic-N could coordinate with copper to enrich the electron density on the catalytic interface, leading to a clear improvement of performance for CRR to C_2 products [17]. The electronic structure of Fe in iron-nickel selenide nanosheets can be regulated by P doping, which enhanced the conductivity of the electrocatalyst, and optimized the adsorption of oxygen-containing intermediates, thus reducing the kinetic barrier [18]. In addition, sulfur doping can lead to electronic delocalization of Bi, and help achieve high current density and faradaic efficiency of

formate in CRR [19]. The carbon atom's versatility is widely applied in the preparation of metal materials such as stainless steel and cast iron [20-23]. However, studies on fine-tuning the electronic structure of metal electrocatalysts for CRR by carbon doping have rarely been reported so far. A comprehensive understanding of the C doping effect on CRR activity is also lacking.

For the first time, we synthesized the carburized In_2O_3 nanorods (In_2O_3-C) by pyrolysis of MIL-68 (In). The carbon atoms were applied to increase the electron density of In atom and rebalancing the conductivity and activity of In_2O_3 for CRR to formate. In addition, the *in-situ* attenuated total reflection infrared adsorption spectroscopy (ATR-SEIRAS), *in-situ* surface-enhanced Raman spectroscopy (SERS), and density functional theory calculations (DFT) were combined to track and clarify the whole reaction mechanism from CO_2 to formate.

2.2 Experiment

2.2.1 Materials

All chemicals (AR) were used as received without further purification. $In(NO_3)_3 \cdot xH_2O$ (99.99%), 1,4-benzene dicarboxylic acid (H_2BDC, 99%), N, N-dimethyl formamide (DMF) was obtained by Aladdin. Ethanol, KOH, and $KHCO_3$ were used by Sinopharm Chemical Reagent Co., Ltd. The water in all experiments was purified by a Millipore system. The high purity Ar (99.999%), high purity N_2 (99.999%), and high purity CO_2 (99.999%) were used.

2.2.2 Preparation of In_2O_3-C Nanorods

$In(NO_3)_3 \cdot xH_2O$ of 1.36 mmol and H_2BDC of 1.20 mmol dissolved into DMF of 5 mL. Then, the above solution was heated at 100 °C for 24 h in a Teflon-lined stainless-steel autoclave. The products [MIL-68(In) Nanorods] were obtained by centrifugation and washed with ethanol several times and then dried at 80 °C for 12h.

The MIL-68(In) nanorods were the first vacuum dried at 150 °C for 2 h. And then, they were heated at 500 °C (a ramping rate of 5 °C min^{-1}) for 2 h in a tube furnace in

an Ar atmosphere and calcined at 500 °C (a heating rate of 5 °C min^{-1}) for 2 h in the air within a muffle furnace to obtain In_2O_3-C (carbon-doped).

2.2.3 Preparation of In_2O_3

The In_2O_3, as a control sample, was synthesized by the calcination method. In_2O_3 was synthesized with $In(NO_3)_3 \cdot xH_2O$ directly calcined at 500 °C for 3 h with a heating rate of 5 °C min^{-1} within a muffle furnace.

2.2.4 Characterization Methods

The crystal structure of materials was detected by X-ray diffraction (XRD, X'Pert PRO MPD) with Cu Kα (40 kV, 40 mA, λ = 1.5406 Å). Binding energy was performed on X-ray photoelectron spectroscopy (XPS, Thermo Scientific Escalab 250XI) with Al Kα radiation. Morphologies were analyzed by scanning electron microscopy (SEM, Hitachi S-4800) and transmission electron microscopy (TEM, JEM-2010).

The *in-situ* surface-enhanced Raman spectroscopy (SERS) measurements were tested by a Renishaw inVia Qontor Raman microscope in a modified flow cell. The carbon paper loading electrocatalyst as a working electrode was assembled in an *in-situ* reaction cell with a carbon rod as a counter electrode, Ag/AgCl electrode as a reference electrode, and 1 M KOH solution as electrolytes.

The *in-situ* attenuated total reflection surface-enhanced infrared adsorption spectroscopy (ATR-SEIRAS) spectra were using an FT-IR spectrometer (Nicolet iS50, Thermo Scientific) equipped with an MCT-A detector. A hemicylindrical Si prism deposited with Au film was used as an electrode substrate. The catalysts ink of 20 μL, prepared using a mixture that electrocatalysts of 5 mg, ethanol of 0.95 mL, and Nafion solution of 50 μL, was dropped onto the surface central area of a hemicylindrical Si prism. The Si prism was assembled in a spectro-electrochemical cell with Pt wire as a counter electrode, Ag/AgCl electrode as a reference electrode, and 0.5 M $KHCO_3$ solution as electrolytes. All spectrum was collected at a resolution of 4 cm^{-1} and each single-beam spectrum was an average of 200 scans. An Autolab PGSTAT 204 electrochemical workstation was used for potential control.

2.2.5 CO_2 Electrochemical Measurements

All electrochemical measurements were carried out using a three-electrode system on a CHI 760E electrochemical workstation (Shanghai CH Instruments Co., China). The H cell system consists of the anode, the cathode, and a Nafion 117 proton exchange membrane. Both sides were filled with 0.1 M $KHCO_3$ aqueous solution of 40 mL as electrolytes. Then CO_2 was bubbled into the electrolyte on the cathode side for more than 30 min under stirring until saturated and the CO_2 gas flow was controlled at a steady stream (20 sccm) during the electrochemical measurements. The pH value of the CO_2-saturated electrolyte was 6.8. All potentials cited were referenced to the reversible hydrogen electrode (RHE) in this work. An L-type glassy-carbon (GC, ø = 12 mm) loading electrocatalyst was used as a working electrode with an Ag/AgCl electrode (saturated KCl solution) as a reference electrode and a platinum gauze (1 × 1 cm^2) as the counter electrode. Before electrochemical testing, the electrolyte was bubbled with N_2 for 30 min to exclude air in the solution. For the preparation of the working electrode, the GC electrode was polished and thoroughly rinsed in water and ethanol and dried with a wiper for the lens. Materials of 5 mg dispersed into ethanol of 500 μL with 5 % Nafion solution of 10 μL. Catalyst ink of 100 μL dripped on the GC electrode and dried with N_2 at room temperature.

In the flow cell, the gas diffusion electrode, Ag/AgCl electrode, and Ni foam were used as working, reference, and counter electrodes, respectively. The anodic and cathodic chambers were separated by an anion exchange membrane (the Fumasep FAA-3-PK-130 membrane). During performance evaluations, both sides were circulated with 1 M KOH aqueous solution as an electrolyte at the rate of 20 sccm. A steady CO_2 stream (20 sccm) was fixed in the gas chamber (1 cm × 1 cm). The applied potentials were presented with iR drop compensation. For the preparation of the flow cell working electrode, catalysts of 10 mg, ethanol of 1 mL, and 5 % Nafion solution of 20 μL were mixed and sonicated for 20 min to get the catalyst ink. Then, the catalyst ink of 100 μL was dropped on carbon paper (AvCarb P75t, Fuel Cell Store). A gas diffusion electrode loading with ~ 1.0 mg cm^{-2} was obtained.

The faradic efficiencies of all products were calculated according to Eq. 1:

$$FE = \frac{moles\ of\ product}{Q/nF} \times 100\% \quad \text{Eq. 1}$$

(Q: electric quantity; F: Avogadro constant; n: transferred electron number)

The energy conversion efficiencies (EE) of the half-cell were calculated according to Eq. 2:

$$EE = (1.23 - E_i) \times FE_i/(1.23 - E_{app}) \quad \text{Eq. 2}$$

where 1.23 represented the standard half-reaction potentials for anodic oxygen evolution reaction (OER, 1.23 V *vs.* RHE), E_i represented the thermodynamic potential (*vs.* RHE) in CRR for the product *i*. The value was -0.2 V for the formate, E_{app} was the applied potential (*vs.* RHE).

2.2.6 Computational Method

We have employed the Vienna Ab Initio Package (VASP) [24, 25] to perform all the density functional theory (DFT) calculations within the generalized gradient approximation (GGA) using the PBE [26] formulation. We have chosen the projected augmented wave (PAW) potentials [27, 28] to describe the ionic cores and take valence electrons into account using a plane-wave basis set with a kinetic energy cutoff of 400 eV. Partial occupancies of the Kohn−Sham orbitals were allowed using the Gaussian smearing method and a width of 0.05 eV. The electronic energy was considered self-consistent when the energy change was smaller than 10^{-5} eV. A geometry optimization was considered convergent when the force change was smaller than 0.02 eV/Å. Grimme's DFT-D3 methodology [29] was used to describe the dispersion interactions.

The equilibrium lattice constant of cubic In_2O_3 unit cell was optimized, when using a 2×2×2 Monkhorst-Pack k-point grid for Brillouin zone sampling, to be a=10.238 Å. We then use it to construct an In_2O_3(111) surface model (model 1) with *p*(1×1) periodicity in the x and y directions and one and half stoichiometric layers in the z-direction separated by a vacuum layer in the depth of 15 Å in order to separate the surface slab from its periodic duplicates. Model 1 comprises of 48 In and 72 O atoms. Model 2 was built by placing a C atom at one interstitial site of sublayer. Model 3 was

built by replacing one O atom on the outmost layer with one C atom. During structural optimizations, the gamma point in the Brillouin zone was used for k-point sampling, and the bottom stoichiometric layer was fixed while the rest were allowed to relax.

The adsorption energy (E_{ads}) of adsorbate A was defined as (Eq. 3)

$$E_{ads} = E_{A/surf} - E_{surf} - E_{A(g)} \quad \text{Eq. 3}$$

where $E_{A/surf}$, E_{surf}, and $E_{A(g)}$ are the energy of adsorbate A adsorbed on the surface, the energy of clean surface, and the energy of isolated A molecule in a cubic periodic box with a side length of 20 Å and a 1×1×1 Monkhorst-Pack k-point grid for Brillouin zone sampling, respectively.

The free energy of a gas phase molecule or an adsorbate on the surface was calculated by the equation $G = E - ZPE - TS$, where E is the total energy, ZPE is the zero-point energy, T is the temperature in kelvin (298.15 K is set here), and S is the entropy.

Finally, transition states for elementary reaction steps were determined by the nudged elastic band (NEB) method[30]. In the NEB method, the path between the reactant and product is discretized into a series of structural images.

2.3 Results

2.3.1 Synthesis and Characterizations of Materials

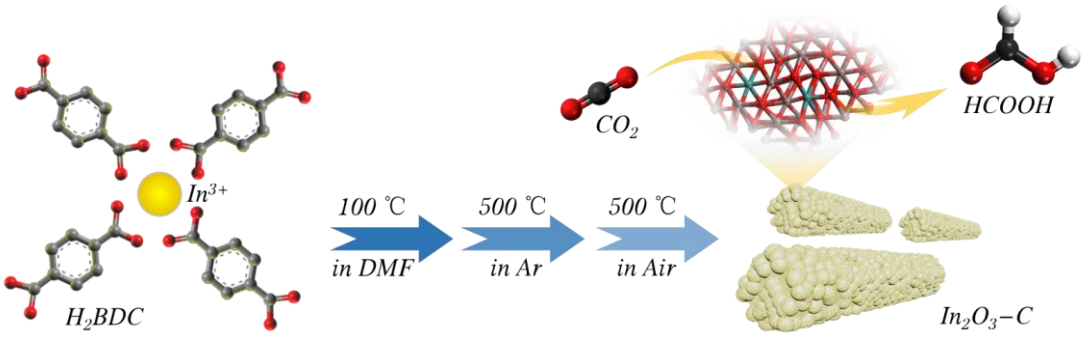

Fig. 2.1. Schematic illustration for the synthesis of In_2O_3-C Catalysts.

The synthesized process of In_2O_3-C was schematically exhibited in Fig. 2.1. The In_2O_3 nanorods with interstitial carbon were obtained through two steps of heat treatment with MOF precursor [MIL-68(In)] at 500 ^oC under different atmospheres (Ar and air atmosphere). The In_2O_3-C nanorods were composed of numbers of small nanoparticles with a size of ca. 38 nm (Fig. 2.2 a and b). The 0.302 nm lattice spacing in the high-resolution transmission electron microscope (HRTEM) image confirmed the exposure of the In_2O_3(222) plane (Fig. 2.2c). The HADDF-STEM and corresponding elemental mapping of energy dispersive X-ray spectroscopy (EDS) indicate the evenly distributed elements of In, O, and C (Fig. 2.3) in In_2O_3-C.

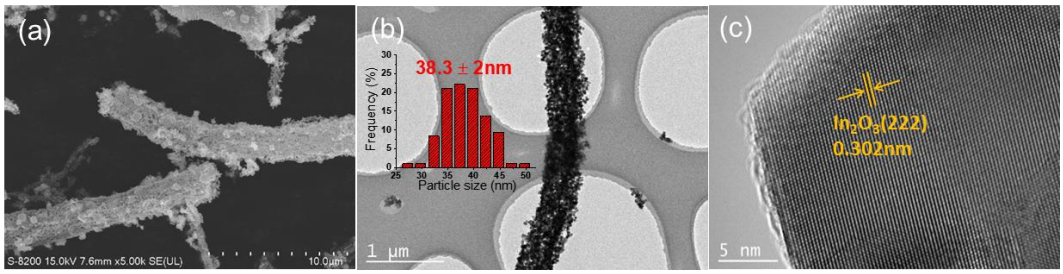

Fig. 2.2. (a) SEM and (b, c) TEM images of In_2O_3-C catalysts.

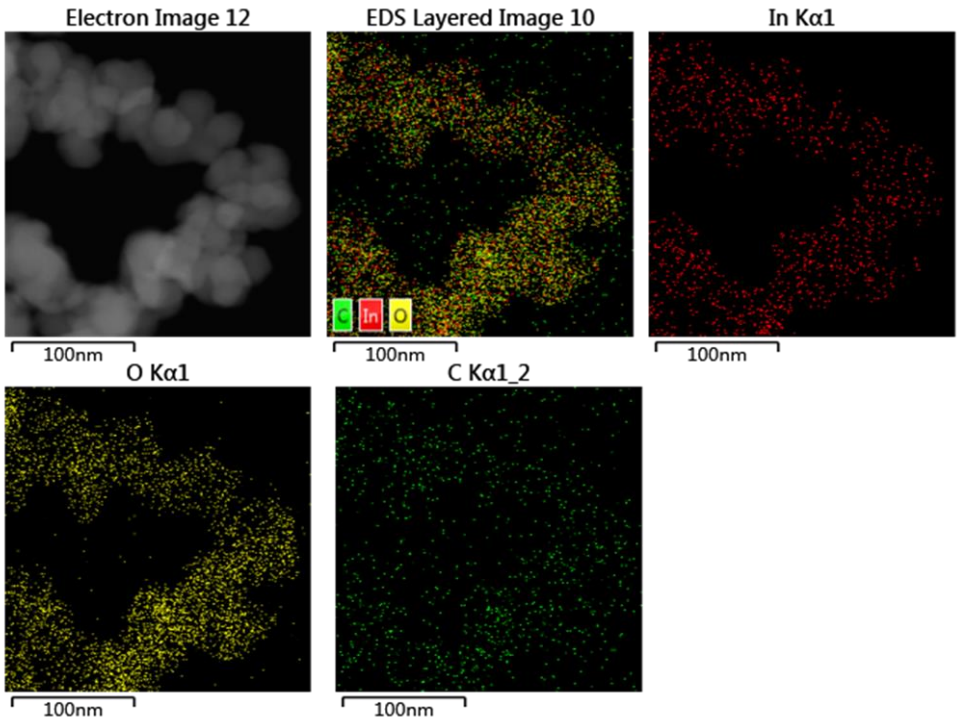

Fig. 2.3. HADDF-STEM image and corresponding EDS elemental mapping of In_2O_3-C.

The X-ray powder diffraction (XRD), X-ray photoelectron spectra (XPS), Raman, and NMR methods were performed to investigate the fine structure of In_2O_3-C. As shown in Fig. 2.4a, the In_2O_3-C and In_2O_3 were both checked with In_2O_3 (PDF#89-4595). The characteristic peak at 30.71° is ascribed to In_2O_3(222) in the In_2O_3, which shifts to 30.59° in the In_2O_3-C (Fig. 2.4b), suggesting an obvious lattice spacing expansion of In_2O_3 after carbon doping [13]. The In_2O_3-C had an obvious carbon signal in solid-NMR (Fig. 2.5a) and Raman spectrum (Fig. 2.5b), demonstrating the carbon atoms were successfully infiltrated to the lattice of In_2O_3. For further confirmation, we adopted a 3D Raman spectra deep scanning of In_2O_3-C in a certain area (the illustration showed a section of the area). The G peak (at 1588 cm^{-1}) of carbon was captured as the beacon and the color change reveals the intensity of the G peak. As depicted in Fig. 2.6a, the 3D Raman spectra scanning image proved the evenly distributed carbon atoms on the catalyst. By analyzing the data of XPS in Fig. 2.6b, the In 3d peak at 444.1 eV (In $3d_{3/2}$) and 451.7 eV (In $3d_{5/2}$) of In_2O_3-C has a negative shift of 0.17 eV compared to In_2O_3, indicating the electron density of In atoms was enriched due to the electron donor effect of carbon atom [31-33]. As a control sample, the pristine In_2O_3 was prepared by direct pyrolysis of indium nitrite salt. As shown in Fig. 2.7, the lattice space of In_2O_3(222) is 0.296 nm, narrower than that of In_2O_3-C, indicating a surface lattice expansion of In_2O_3-C due to carbon doping.

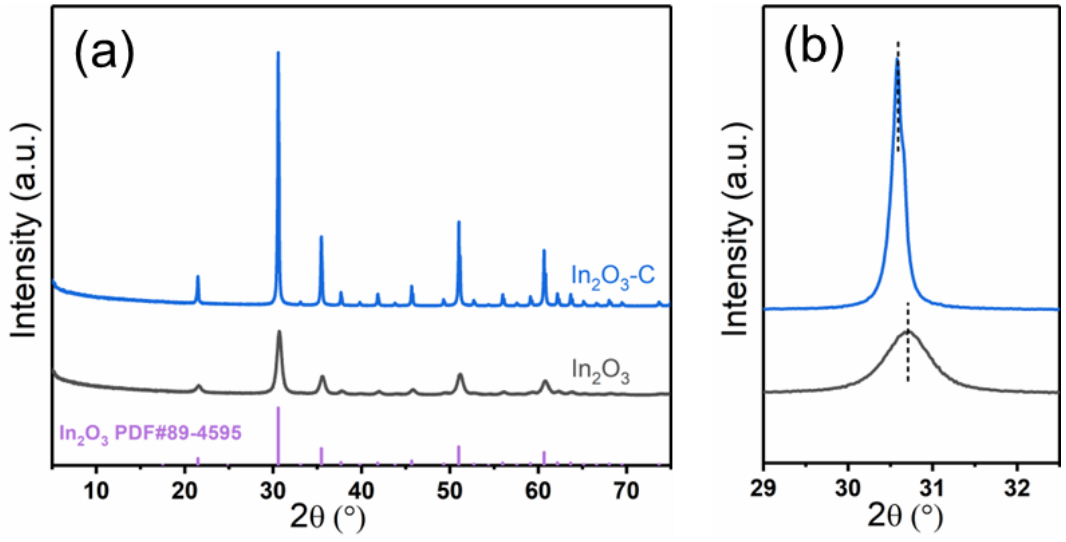

Fig. 2.4. XRD patterns of In_2O_3-C and In_2O_3.

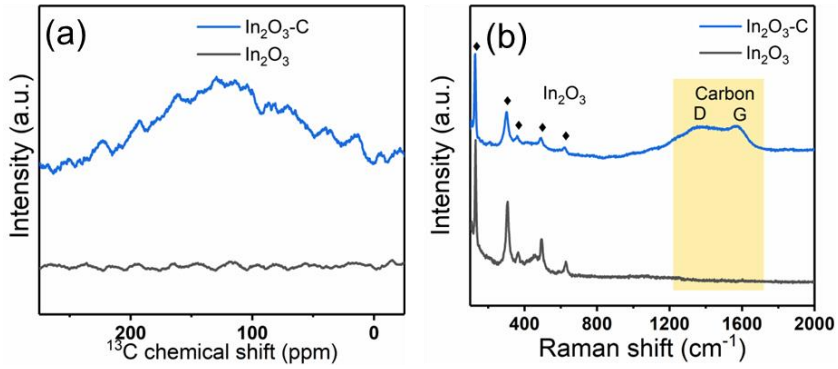

Fig. 2.5. (a) Solid NMR spectra and (b) Raman spectra of In_2O_3-C and In_2O_3.

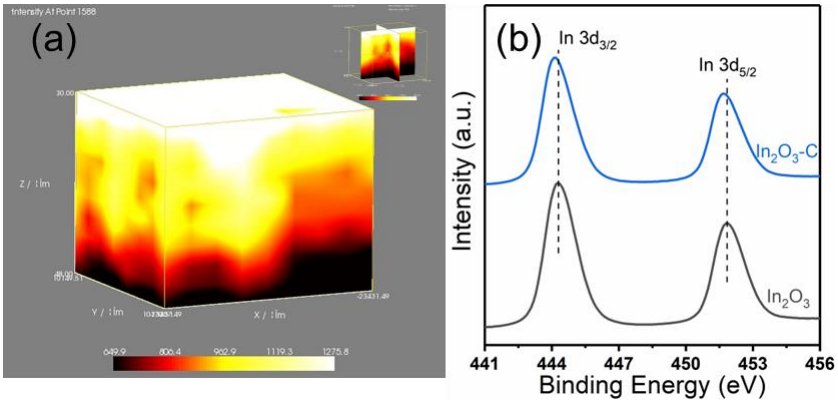

Fig. 2.6. (a) 3D Raman images of deep scanning spectra in In_2O_3-C; (b) In 3d XPS spectra of In_2O_3-C and In_2O_3.

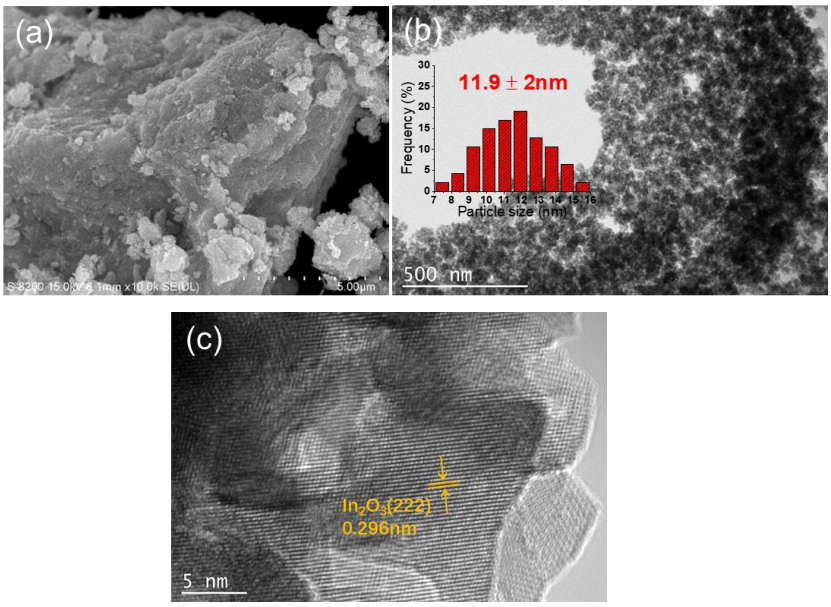

Fig. 2.7. (a) SEM and (b, c) TEM images of In_2O_3.

2.3.2 Electrocatalytic Performance of CRR in the H Cell

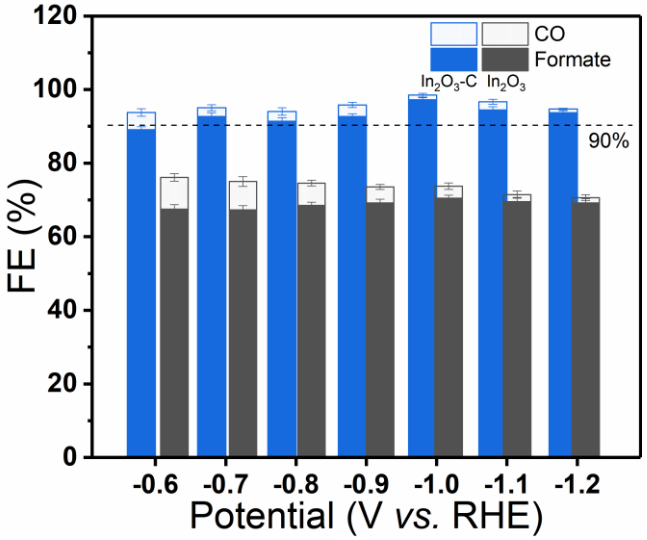

Fig. 2.8. Faradaic efficiency of formate and CO in an H cell at different potentials.

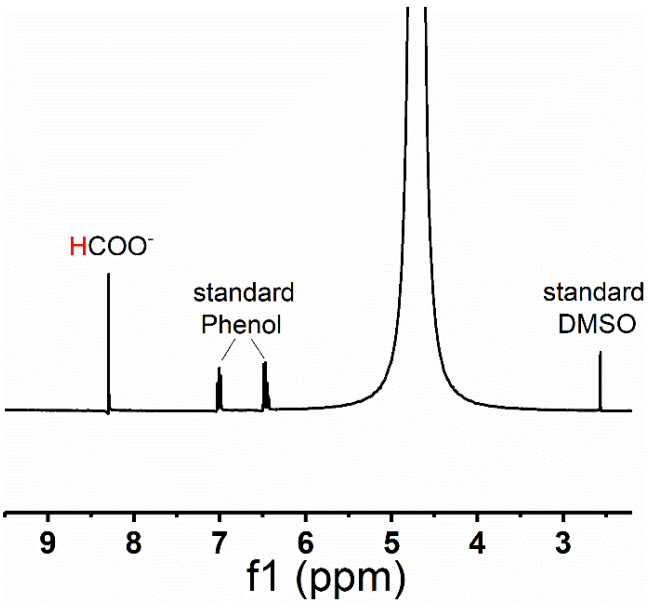

Fig. 2.9. A typical ^{1}H NMR spectrum of liquid products after electrolysis with In_2O_3-C catalyst.

After the catalysts are assembled into an electrode, the electrocatalysis reduction of CO_2 was firstly evaluated at different applied potentials in a typical H-type cell within 0.1 M $KHCO_3$ (Fig. 2.8). The products of formate, CO, and H_2 were all detected by GC and HPLC for In_2O_3 and In_2O_3-C. The only liquid product of formate was confirmed by NMR analysis (Fig. 2.9). Noticeably, the In_2O_3-C exhibited a higher

Faradaic efficiency (FE) of formate (above 90%) in a wide potential range of -0.7 V ~ -1.2 V *vs.* RHE, which is much higher than the In_2O_3 catalyst (about 70%). The FE_{H2} and FE_{CO} were less than 8% and 5% in In_2O_3-C, respectively (Fig. 2.10). The highest FE of formate is 97.2% at -1.0 V *vs.* RHE (Fig. 2.8), corresponding to energy efficiency (EE) of 62.3%. Compare with other In-based materials in the references, the In_2O_3-C has excellent selectivity and EE for CRR to formate (Fig. 2.11 and Table 2.1).

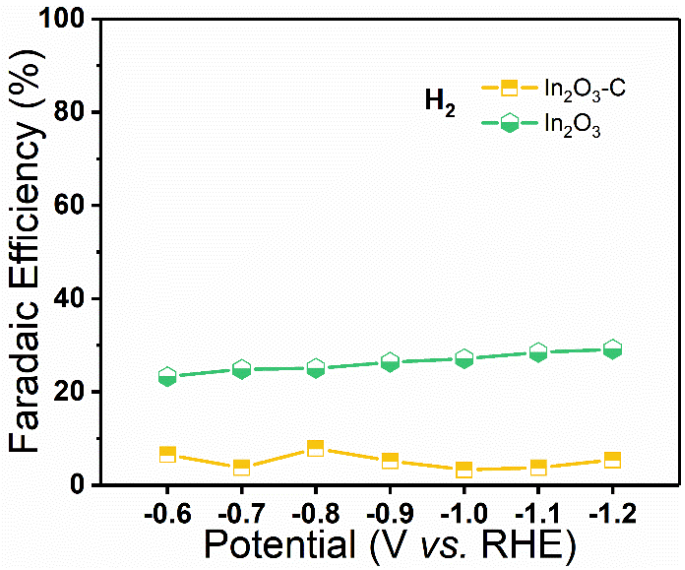

Fig. 2.10. FE for H_2 over In_2O_3-C and In_2O_3 at different potentials.

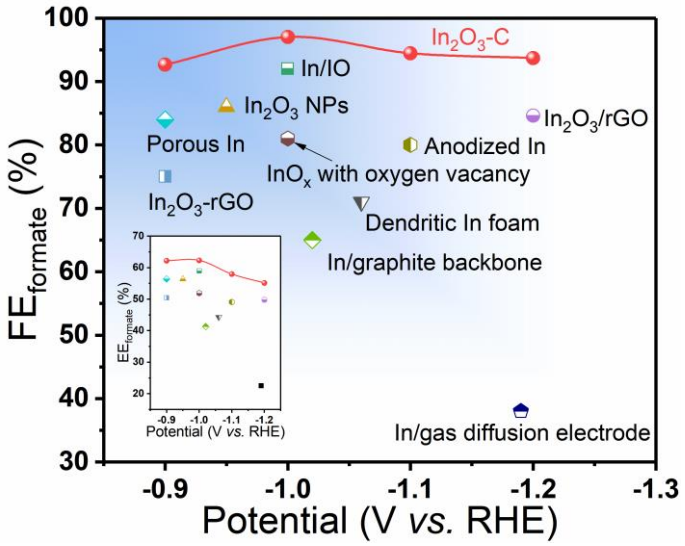

Fig. 2.11. Compare faradaic efficiency and energy efficiency with other In-based literature.

Table 2.1. Overview of In-based catalysts for the reduction of CO_2 to formate in an H cell.

Catalyst	Electrolyte	Potential	FE	j	EE	References
In_2O_3-C	**0.1M $KHCO_3$**	**-1**	**97%**	**5.5**	**62.3%**	**This work**
In/gas diffusion electrode	0.1 M Na_2SO_4	-1.19	38%	2.8	22.5%	[34]
In_2O_3/rGO	0.1 M $KHCO_3$	-1.2	85%	22.2	49.8%	[9]
In_2O_3 nanoparticles	0.5 M $KHCO_3$	-0.95	86%	7.0	56.4%	[35]
In_2O_3@C	0.5 M $NaHCO_3$	-0.9	88%	14.8	58.9%	[7]
In/graphite backbone	0.05 M $NaHCO_3$	-1.02	65%	1.0	41.3%	[36]
In/In_2O_{3-x}	0.5 M $NaHCO_3$	-0.82	89%	-	62.2%	[10]
Anodized In	0.5 M K_2SO_4	-1.1	80%	-	49.1%	[37]
Dendritic In foam	0.5 M $KHCO_3$	-1.06	71%	8.5	44.3%	[38]
InOx with oxygen vacancy	0.5 M $NaHCO_3$	-1	81%	13.0	51.9%	[8]
Porous In	0.1 M $KHCO_3$	-0.9	84%	12.6	56.4%	[39]
In/IO	0.5 M $KHCO_3$	-1	92%	23.8	59.0%	[11]

The electrochemically active surface area (ECSA) is adopted to compare the different activities of In_2O_3-C and In_2O_3. As shown in Fig. 2.12, the In_2O_3-C (11.07 mF cm^{-1}) had nearly twice the ECSA of In_2O_3 (5.22 mF cm^{-1}), which means more active sites can be supplied by In_2O_3-C. Besides, the In_2O_3-C exhibited a higher CO_2 adsorption capacity than pristine In_2O_3 (Fig. 2.13), indicating that the In_2O_3-C benefits CO_2 adsorption, thus accelerating the formation rate of formate [19].

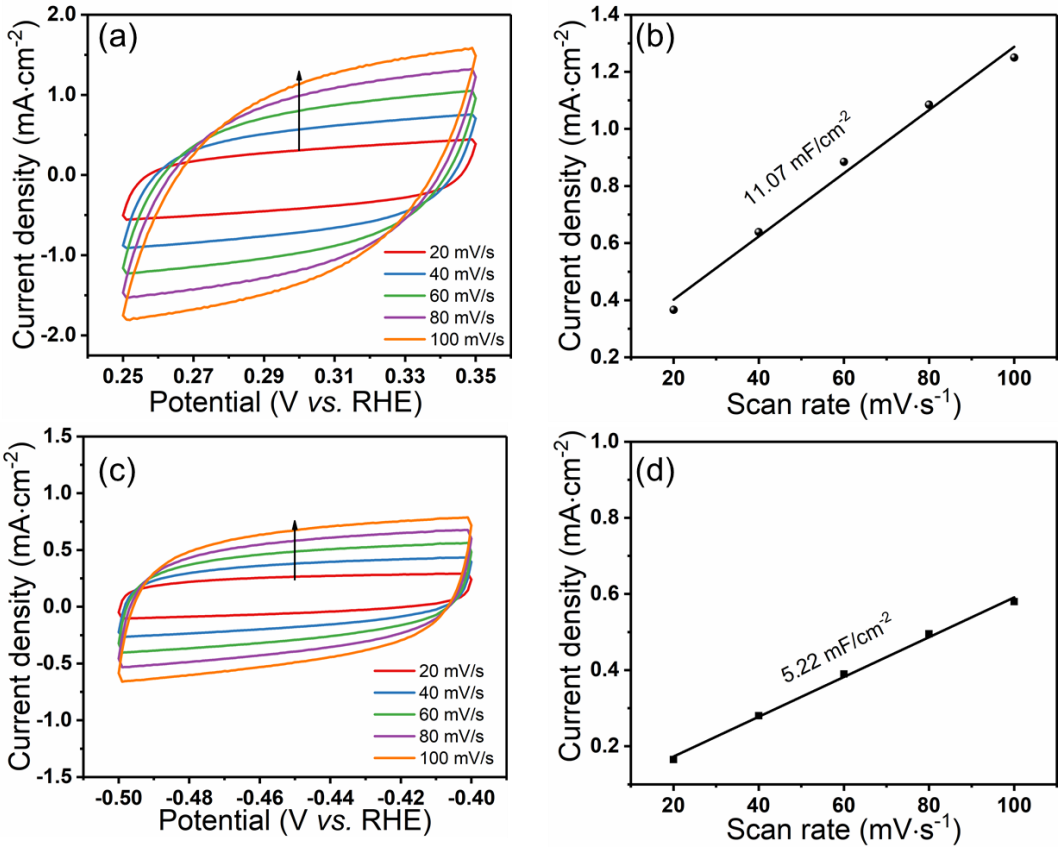

Fig. 2.12. (a)The cyclic voltammetry at different scan rates of In_2O_3-C; (b) Corresponding to the charging current density differences plotted against the scan rates. (c) The cyclic voltammetry at different scan rates of In_2O_3; (d) Corresponding to the charging current density differences plotted against the scan rates.

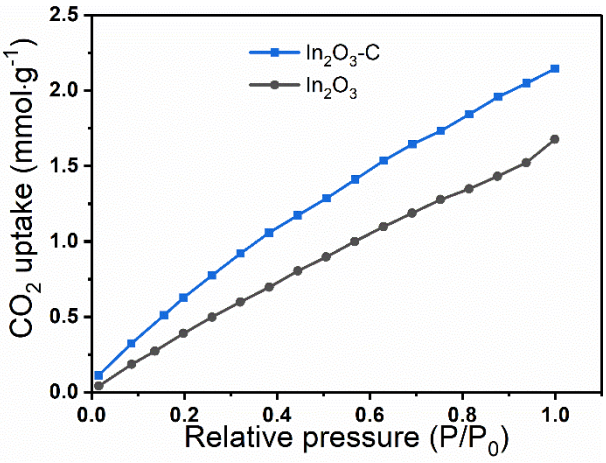

Fig. 2.13. CO_2 uptake isotherms of In_2O_3-C and In_2O_3 at 298.15K.

2.3.3 Electrocatalytic Performance of CRR in the Flow Cell

The CRR performances were also evaluated in a flow cell (Fig. 2.14) with 1 M KOH as electrolyte. The linear sweep voltammetry (LSV) curves (Fig. 2.15) showed a notable increase in current densities on In_2O_3-C compared with In_2O_3, which is consistent with its better activity for CRR. The $FE_{formate}$ is 80~95% during the whole applied potential on In_2O_3-C (Fig. 2.16a), indicating this material has excellent catalytic stability in a wide potential range. Especially, when the current density was boosted to -1 A cm^{-2}, the $FE_{formate}$ remains at 80.5%, corresponding to a partial current density of -805 mA cm^{-2} toward formate, which can rank among the top level compared to the reported catalysts in Table 2.2. In contrast, In_2O_3 only has a low $FE_{formate}$ of 60% at -800 mA cm^{-2} (Fig. 2.16b). Finally, the stability of In_2O_3-C was explored with an industrially relevant current density of -200 mA cm^{-1}. A high $FE_{formate}$ above 85% was maintained for more than 15 h on In_2O_3-C, which is much better than In_2O_3 (Fig. 2.16c). These extraordinary phenomena prompt us to conduct more in-depth mechanism research.

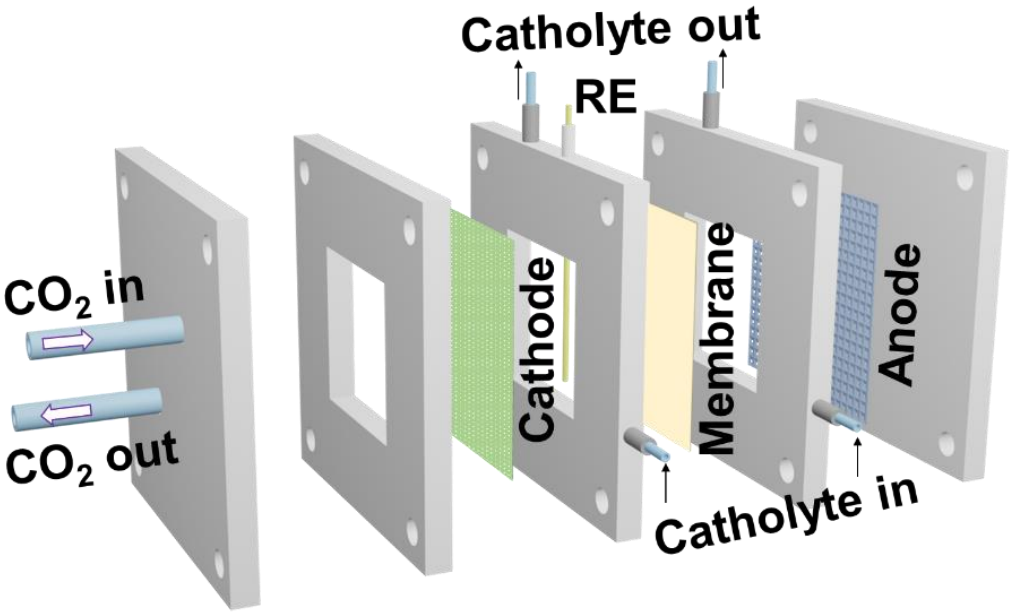

Fig. 2.14. The architecture of flow cell.

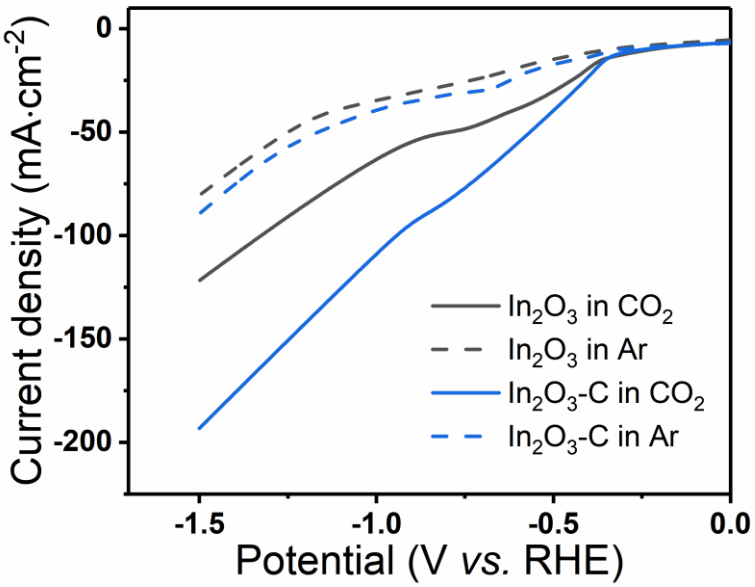

Fig. 2.15. LSV curves over In_2O_3-C and In_2O_3 in a flow cell.

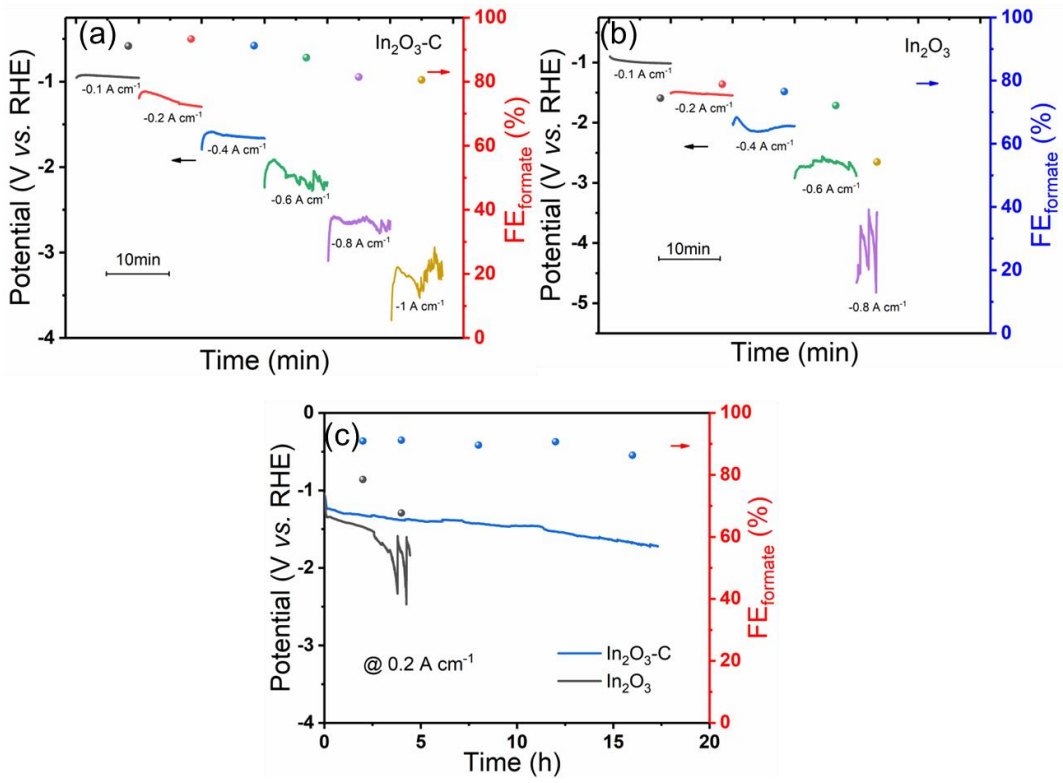

Fig. 2.16. Chronopotentiometry test of (a) In_2O_3-C and (b) In_2O_3 at a different current density from -0.1 to -1 A cm^{-2}; (c) Stability test of In_2O_3-C and In_2O_3 at -0.2 A cm^{-2}.

Table 2.2 Overview of In-based catalysts for the reduction of CO_2 to formate in a flow cell.

Catalyst	Electrolyte	Potential	FE	$j_{formate}$	References
In_2O_3-C	**1.0 M KOH**	**-3.4**	**80.5**	**~805**	**This work**
In_2O_3-C	**1.0 M KOH**	**-1.3**	**93.3**	**~187**	**This work**
In_2O_3@C	1.0 M KOH	-1.4	93.9	~185	[33]
In@CNR	1.0 M KOH	-0.62	90.5	~123	[40]
MIL-68(In)-NH_2	1.0 M KOH	-1.2	96.0	~140	[31]
$ZnIn_2S_4$ nanosheets	1.0 M KOH	-1.2	94.0	~245	[41]
Ni-In_2O_3@C NFs	1.0 M KOH	-1.0	90.5	~358	[12]

2.3.4 *In-situ* ATR-SEIRAS and SERS study for Electrocatalysis Mechanism

First of all, the *In-situ* ATR-SEIRAS was performed at different potentials to catch the key intermediates of CRR (Fig. 2.17). Consist with other reported works [42, 43], the HCOO* pathway was confirmed on the reaction path on In_2O_3-C for CRR. As shown in Fig. 2.17, the peak at ~2360 cm^{-1} corresponding to CO_2 asymmetrical stretching was found under all applied potentials, which is derived from the adsorption of CO_2 on the surface of the catalyst [43]. The two peaks at ~1339 cm^{-1} and ~1509 cm^{-1} were associated with the H_2CO_3 and HCO_3^-, respectively. These two characteristic peaks did not change with the applied potentials, indicating the CO_2 aqueous solution maintained saturation during the whole reaction [42]. Furthermore, the peaks at ~1654 cm^{-1} and ~1392cm^{-1} are attributed to the stretching vibration of HCOO*, while the stretching vibration of COOH* is located at 1573 cm^{-1}. Compare with COOH*, the signal of HCOO* was significantly increased with the applied potential growth, proving the HCOO* intermediates were dominant on the catalyst surface and the formate was produced from HCOO* rather than COOH* [44]. Furthermore, the by-product of CO was analyzed and the peaks between ~2000 cm^{-1} and ~2160 cm^{-1} corresponding to the adsorbed/dissociative CO were not obvious, indicating the CO was almost inhibited on

In_2O_3-C, which explains why the FE of formate is higher than that of CO on In_2O_3-C [19].

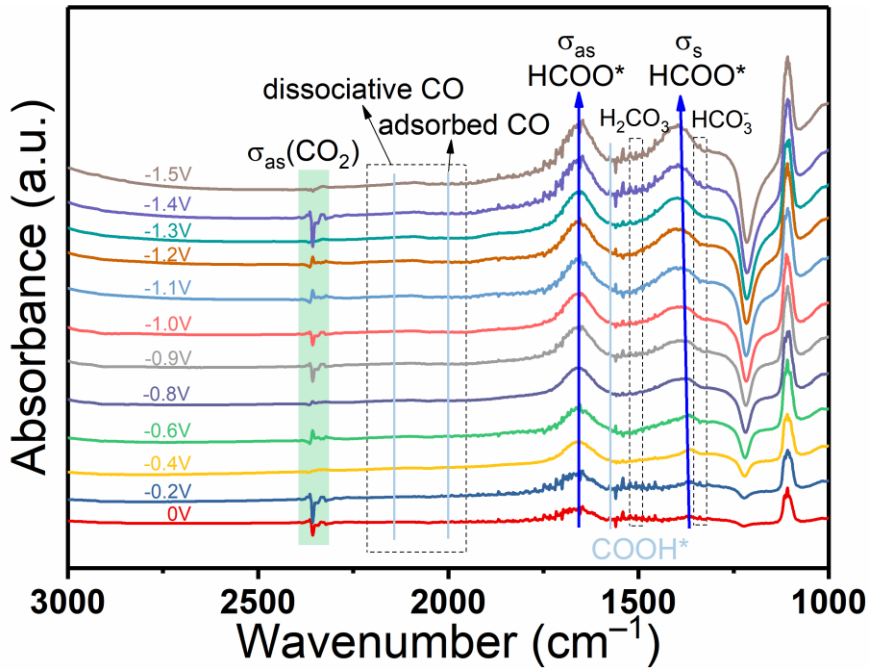

Fig. 2.17. *In-situ* ATR-SEIRAS spectra of In_2O_3-C at 0V ~ -1.5 V *vs.* RHE.

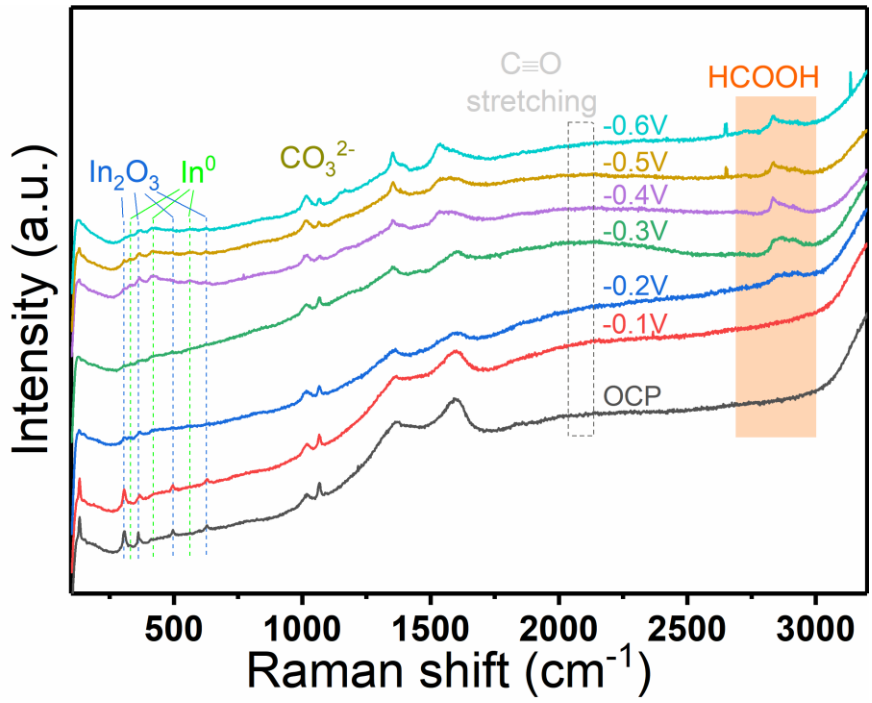

Fig. 2.18. The *in-situ* surface-enhanced Raman spectra of In_2O_3-C at 0 V ~ -0.6 V *vs.* RHE.

The *in-situ* surface-enhanced Raman spectroscopy (SERS) was performed to explore the relationship between the structure of In_2O_3-C and the change of products in the CRR process. As shown in Fig. 2.18, the characteristic peaks at 308.7 cm^{-1}, 366.0 cm^{-1}, 498.3 cm^{-1}, and 626.2 cm^{-1} were assigned to $\delta(InO_6)$, $\nu(InO_6)$, In−O−In, and $\nu(InO_6)$ [45]. Interestingly, several new characteristic peaks at 333.8 cm^{-1}, 419.3 cm^{-1}, and 561.9 cm^{-1} appeared at -0.2 V *vs.* RHE, which are ascribed to In^0. The XRD pattern and XPS spectrum analysis of In_2O_3-C after CRR was performed (Fig. 2.19), suggesting the coexistence of In_2O_3 and In^0 in In_2O_3-C were attributed to the partial reduction of In^{3+} during CRR, which is consistent with *in-situ* SERS. The HADDF-STEM image and corresponding EDS elemental mapping of In_2O_3-C after CRR was detected, suggesting the stable morphology of In_2O_3-C catalyst and the evenly distributed elements of In, O, and C on the surface of spent catalyst (Fig. 2.20). The Raman spectra analysis of In_2O_3-C before and after CRR was performed, suggesting the coexistence of In_2O_3 and In^0 in In_2O_3-C were attributed to the partial reduction of In^{3+} during CRR. However, the In_2O_3 was the main active sites (Fig. 2.21).

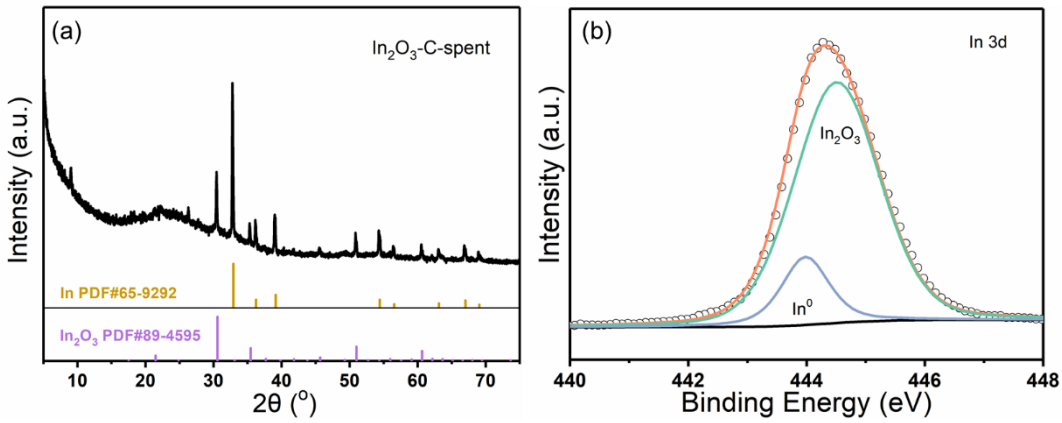

Fig. 2.19. (a) XRD pattern and (b) XPS spectrum of In_2O_3-C after CO_2 electroreduction.

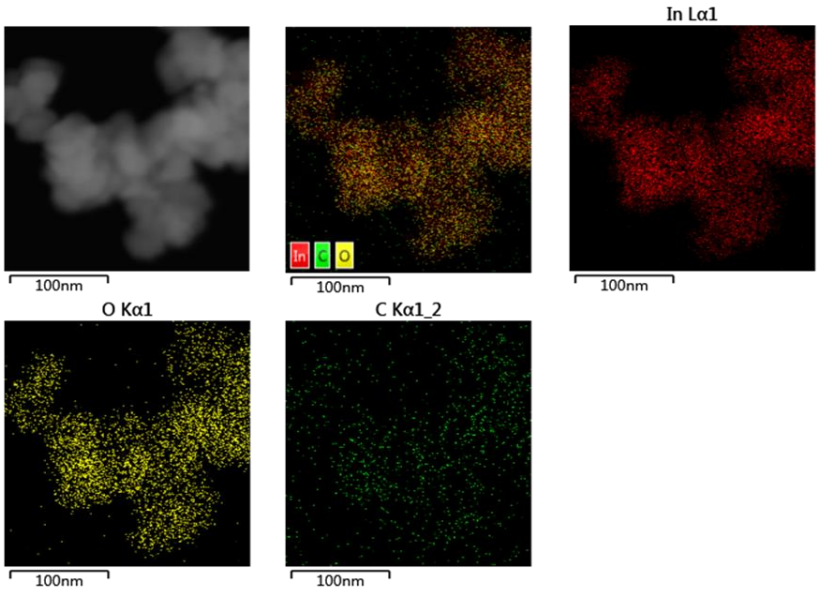

Fig. 2.20. HADDF-STEM image and corresponding EDS elemental mapping of In_2O_3-C after CO_2 electroreduction.

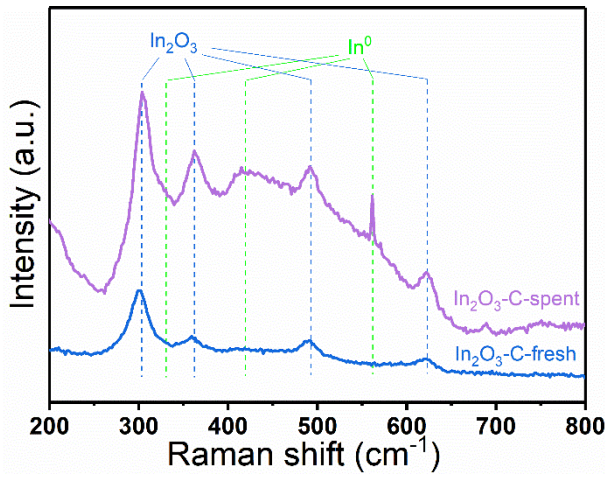

Fig. 2.21. Raman spectra of In_2O_3-C before and after CO_2 electroreduction.

The coexistence of In_2O_3 and In^0 in In_2O_3-C were attributed to the partial reduction of In^{3+} during CRR [11]. At the same time, the broad peak at ~2840 cm^{-1} associated with the C-H stretching of formate molecular was observed [46], proving the generation of formate in real-time. Furthermore, the formation of formate was *in-situ* detected by using SERS spectra in a 60 μm *60 μm area (Fig. 2.22a). It can be seen that the formate signals around ~2840 cm^{-1} appeared on every node at -0.2 V *vs.* RHE (Fig. 2.22b), indicating the active sites toward formate were uniformly distributed on the surface of

In_2O_3-C. Consistent with the *In-situ* ATR-SEIRAS, no signal of C≡O stretching was observed in the whole applied potential range, indicating the inert activity toward CO on In_2O_3-C [47]. These results can explain the ultra-low FE_{CO} (<5%, Fig. 2.8).

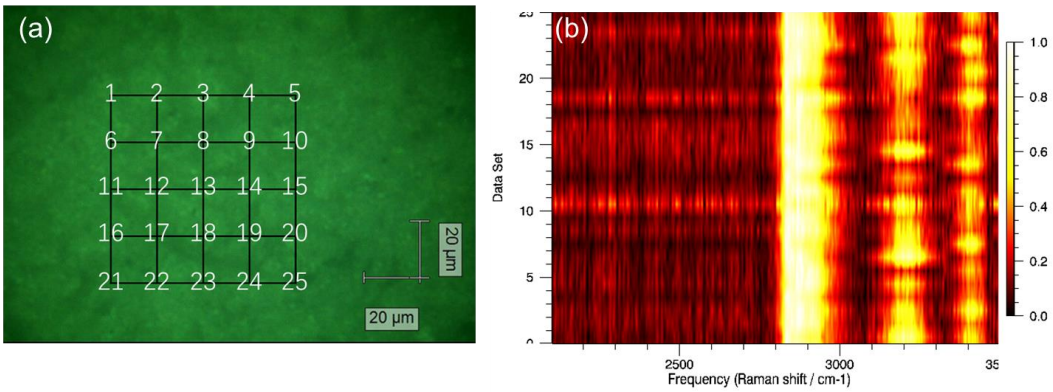

Fig. 2.22. (a) Optical digital photograph of In_2O_3-C by optical microscope on *In-situ* surface-enhanced Raman spectra; (b) *In-situ* surface-enhanced Raman spectra of In_2O_3-C to exploring the formation of formate.

2.3.5 DFT Calculations

Combined with *in-situ* measurements, the DFT calculations were conducted to elucidate the mechanism of formate generation on In_2O_3-C. To investigate the existential form of doped carbon and the relevant structural adjustment in In_2O_3, three models (Fig. 2.23) were constructed and calculated by Vienna Ab Initio Package (VASP).

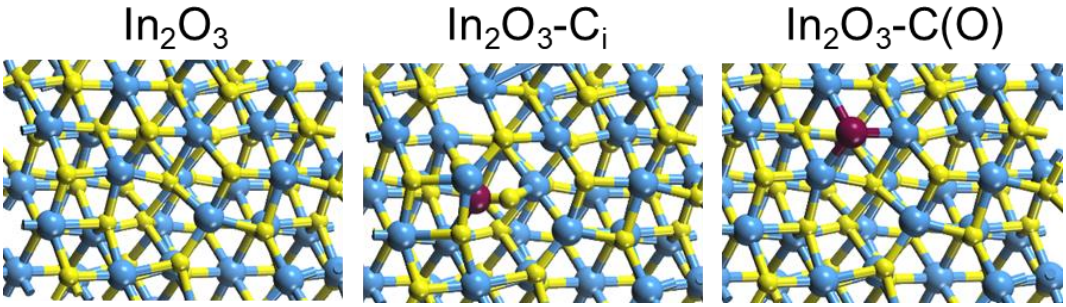

Fig. 2.23. The optimized calculation models of In_2O_3, In_2O_3-C_i, and In_2O_3-C(O). Colors: In, blue; O, yellow; C, brown.

Model 1 (In_2O_3) showed the initial In_2O_3(111) surface with p(1×1) periodicity in the x and y directions and one and a half stoichiometric layers in the z-direction were constructed with a vacuum layer in the depth of 15 Å to separate the surface slab from its periodic duplicates. Model 2 (In_2O_3-C_i), the interstitial carbon model, was built by placing a C atom at one interstitial site of the sublayer. Model 3 (In_2O_3-C(O)), the substitution carbon model, was built by replacing one O atom on the outmost layer with a C atom. These models were analyzed by the Bader charge to explain the electronic properties and Gibbs free energy, respectively [13]. As shown in Fig. 2.24, the Bader charge analysis revealed that the In atom around the C atom (dotted red circle) in the In_2O_3-C_i model obtained an electron transfer of 0.094, which was higher than that of In_2O_3-C(O) (0.070), suggesting more negative charge accumulated on the In atom for In_2O_3-C_i. The charge density difference plot exhibited the clear electron localization of In atoms around the C atom in the In_2O_3-C_i model (Fig. 2.25). The yellow and blue contours represent electron density accumulations and depressions, respectively. The yellow contour in violet rectangles represented the electron enrichment around In atom near the C atom. The green contour around the C atom (below the In atom) indicates its electron density depressions. Obviously, the yellow contour means the electron density of In atoms near the C atom increased, which is consistent with the negative shift of 0.17 eV in XPS spectra [13].

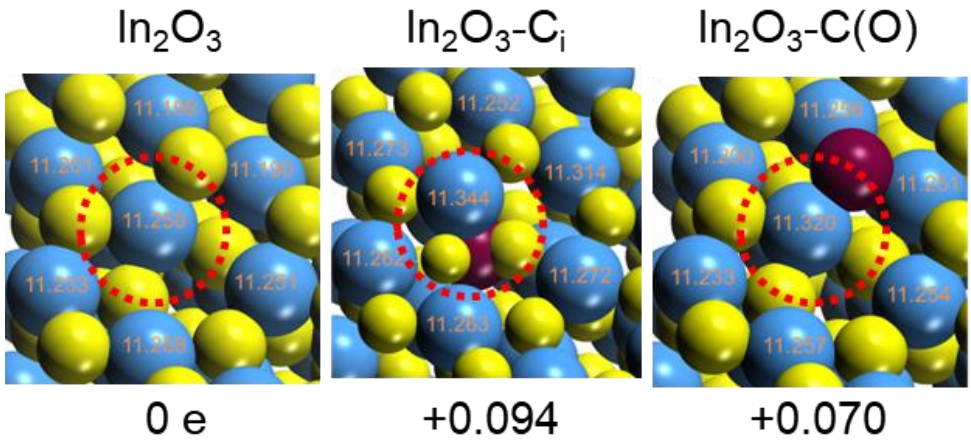

Fig. 2.24. Formal Bader charge values of the In atoms around C atom in the series In_2O_3 models. Colors: In, blue; O, yellow; C, brown.

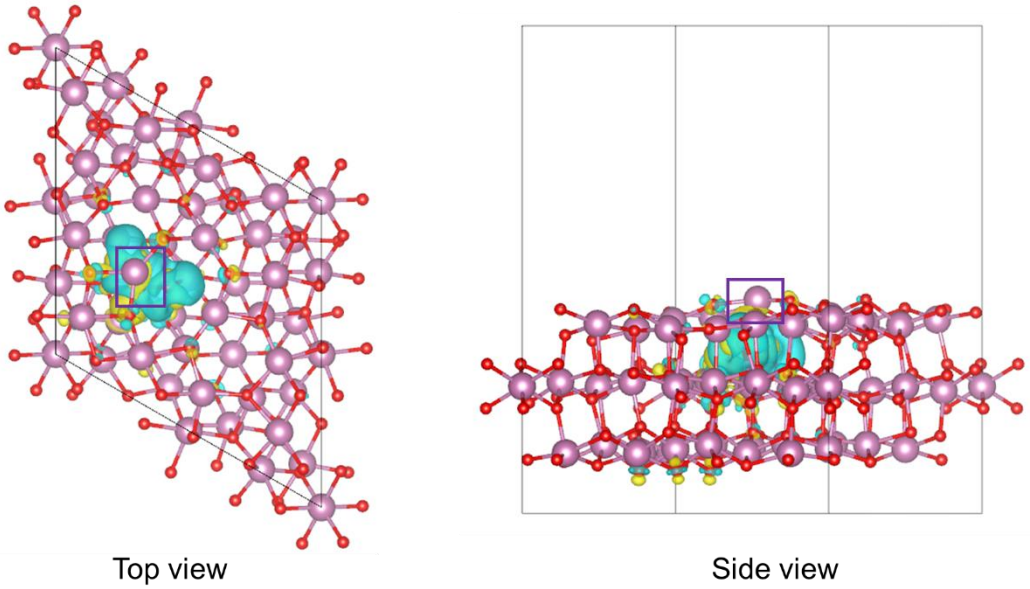

Fig. 2.25. Top view of electron density difference on the In_2O_3-C_i model. The yellow and green contours represent electron density accumulations and depressions, respectively. The violet rectangles (yellow contour) represent the electron enrichment around In near the C atom. The green contour around the C atom symbol its electron density depressions. Colors: In, violet; O, red; C, brown.

Moreover, the Gibbs free energy changes were calculated from CO_2 to HCOOH, including the reaction intermediate for three models (Fig. 2.26-2.28, Table 2.3-2.5). As shown in Fig. 2.29, the adsorption models of three In_2O_3 were exhibited. The minimum free energy barriers over the In_2O_3-C_i model were 0.47 eV for the elementary reaction path of HCOO* + 1/2 H_2(g) $\rightarrow$ HCOOH*, which is much lower than that of In_2O_3 (1.02eV) and In_2O_3-C(O) (1.99eV) [48]. Consequently, the In_2O_3-C_i model represents the optimization catalyst for CRR to formate, which is consistent with the experimental results and Bader charge analysis.

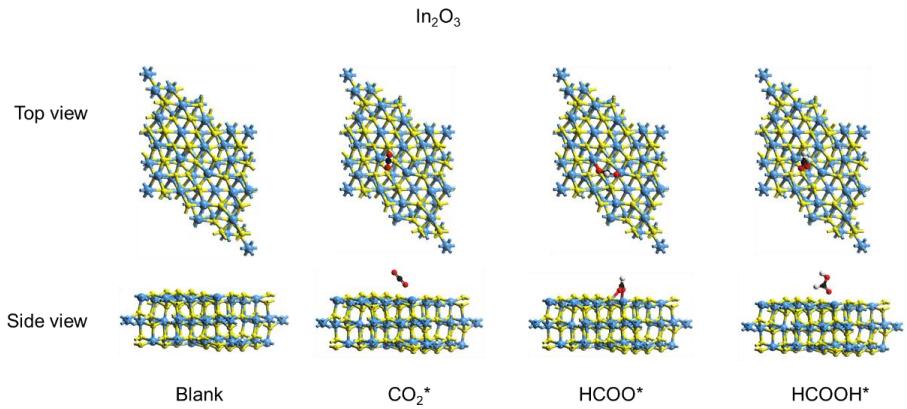

Fig. 2.26. Top- and side-view of the optimized configurations of the In_2O_3 models. Colors: In, blue; O, yellow; C, brown. Absorbent colors: C, black; O, red; H, white.

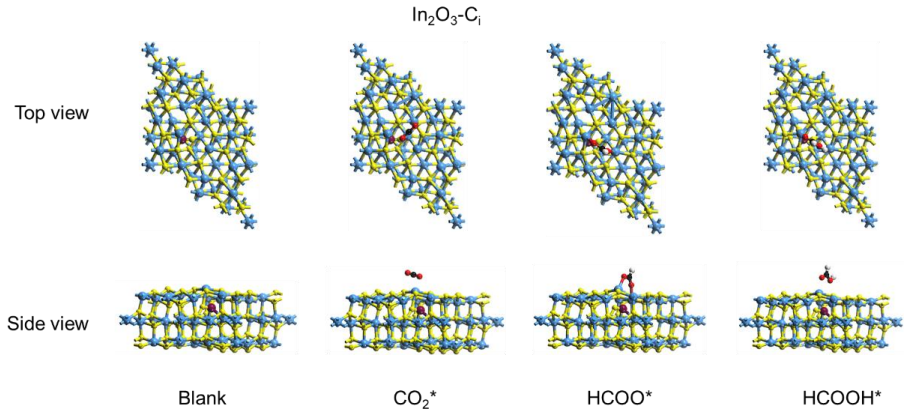

Fig. 2.27. Top- and side-view of the optimized configurations of the In_2O_3-C_i models. Colors: In, blue; O, yellow; C, brown. Absorbent colors: C, black; O, red; H, white.

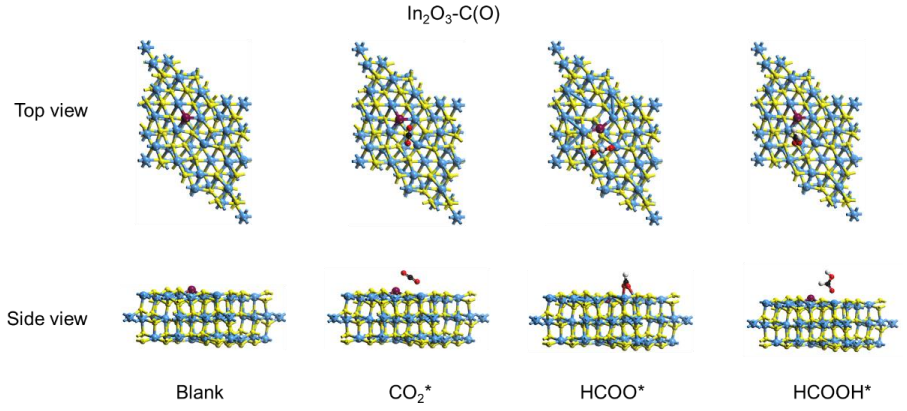

Fig. 2.28. Top- and side-view of the optimized configurations of the In_2O_3-C(O) models. Colors: In, blue; O, yellow; C, brown. Absorbent colors: C, black; O, red; H, white.

Table 2.3. The calculated energetic data for all gas molecules.

Molecule	E_{tot}/eV	$\Delta G_{correction}$/eV	Gibbs free energy/eV
CO_2(g)	-22.989	-0.258	-23.247
H_2(g)	-6.758	-0.046	-6.804
HCOOH(g)	-29.923	0.230	-29.693

Table 2.4. The calculated energetic data for all the surface species.

Model	Adsorbate	E_{tot}/eV	$\Delta G_{correction}$/eV	Gibbs free energy/eV
In_2O_3	*	-661.831	0.000	-661.831
	CO_2	-685.204	0.190	-685.014
	H	-667.046	0.298	-666.748
	HCOO	-687.966	0.504	-687.462
	HCOOH	-692.457	0.747	-691.710
In_2O_3-C_i	*	-668.249	0.000	-668.249
	CO_2	-691.524	0.191	-691.333
	H	-672.503	0.299	-672.204
	HCOO	-695.584	0.510	-695.074
	HCOOH	-698.607	0.772	-697.835
In_2O_3-C(O)	*	-660.273	0.000	-660.273
	CO_2	-682.086	0.147	-681.939
	H	-664.339	0.248	-664.091
	HCOO	-688.366	0.521	-687.845
	HCOOH	-689.082	0.750	-688.332

Table 2.5. The calculated free energy data for all models.

Model	No.	State	G (eV)	G_0 (eV)
In_2O_3	1	$CO_2(g) + H_2(g)$	-30.051	0.00
	2	$CO_2* + H_2(g)$	-29.987	0.06
	3	$HCOO* + H_2(g)/2$	-29.033	1.02
	4	HCOOH*	-29.879	0.17
	5	HCOOH(g)	-29.693	0.36
In_2O_3-C_i	1	$CO_2(g) + H_2(g)$	-30.051	0.00
	2	$CO_2* + H_2(g)$	-29.888	0.16
	3	$HCOO* + H_2(g)/2$	-30.227	-0.18
	4	HCOOH*	-29.586	0.47
	5	HCOOH(g)	-29.693	0.36
In_2O_3-C(O)	1	$CO_2(g) + H_2(g)$	-30.051	0.00
	2	$CO_2* + H_2(g)$	-28.470	1.58
	3	$HCOO* + H_2(g)/2$	-30.974	-0.92
	4	HCOOH*	-28.059	1.99
	5	HCOOH(g)	-29.693	0.36

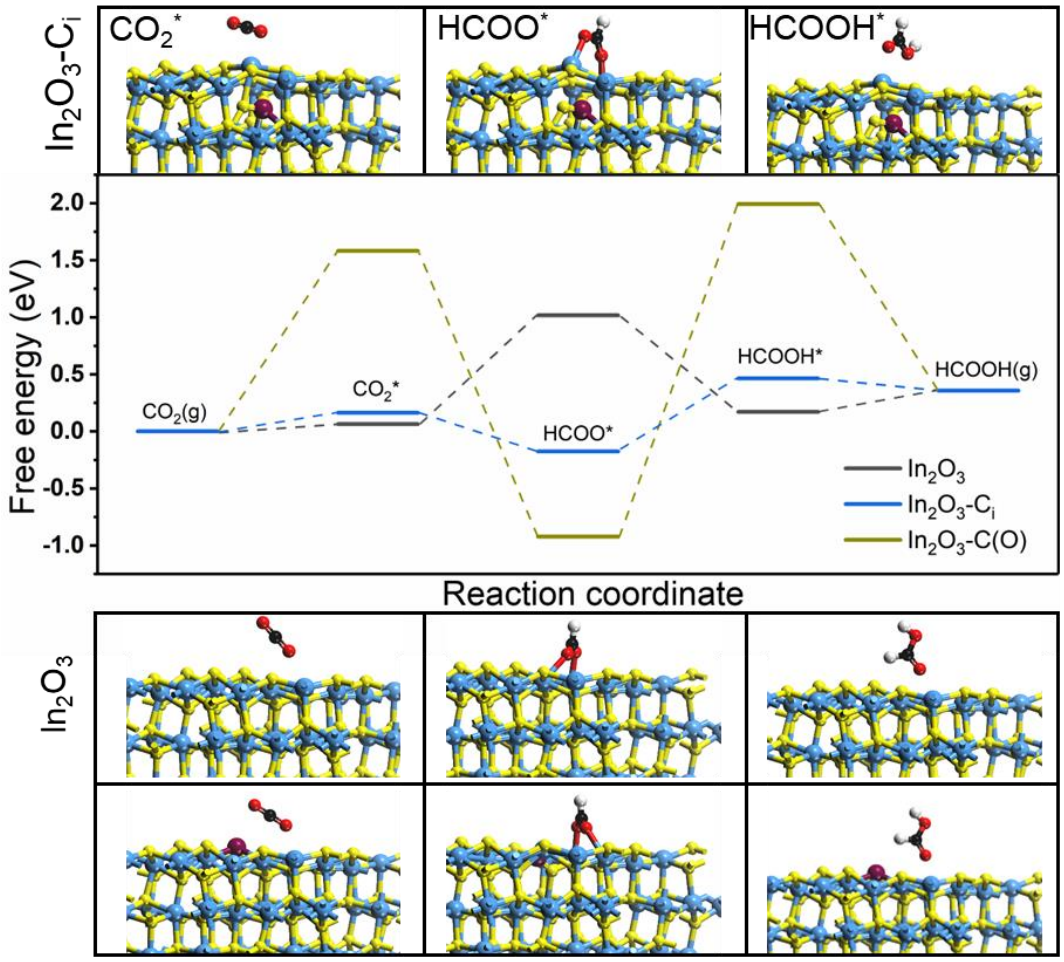

Fig. 2.29. Gibbs free energy diagrams of CO_2 reduction to HCOOH on In_2O_3 (grey curve), In_2O_3-Ci (blue curve), and In_2O_3-C(O) (green curve) and side-view of the optimized configurations of three In_2O_3 models. Substrate colors: In, blue; O, yellow; C, brown. Adsorption colors: C, black; H, white; O, red.

Based on the *in-situ* ATR-SEIRAS, *in-situ* SERS, and DFT calculations, we proposed the complete reaction way from CO_2 to formate on the In_2O_3-C catalyst as shown in Fig. 2.30. First, the CO_2 molecule gets one electron to form CO_2*, and then a proton is transferred to CO_2* to generate HCOO*. At last, the HCOOH was formed by getting another electron and proton or the formate was produced in an alkaline solution [44]. The interstitial carbon played a key role in regulating the electron density of In atom during CRR. Different from previous works on In_2O_3 and carbon composites [31, 33, 40], we found the carbon atoms embedded into the In_2O_3 lattice rather than forming

a carbon-coated structure on the outside of the In_2O_3 may have more significant regulatory effect on In atom, which realized the regulating of electron structure and the exposure of active sites at the same time, thus endowed the In_2O_3-C catalysts with both high selectivity and excellent activity.

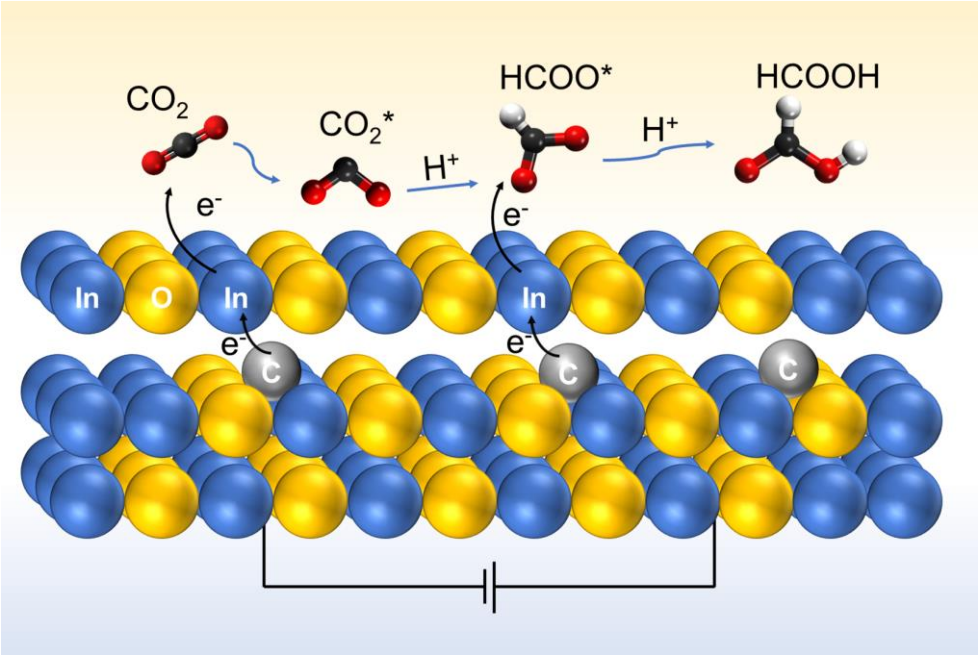

Fig. 2.30. Proposed reaction pathways of HCOOH formation over In_2O_3-C catalyst.

2.4 Conclusion

In summary, the carburized In_2O_3 nanorods were developed as high-performance catalysts for stable and efficient CO_2 electroreduction. In an H-cell, the In_2O_3-C afforded an excellent faradic efficiency above 90% toward formate at a wide potential range of 500 mV, while the highest value of FE reaches 97.2% at -1.0 V *vs.* RHE. The excellent performance could be sustained at a high current density of -1 A cm^{-2} with $FE_{formate}$ of 80.5% in a flow cell, outperforming the bare In_2O_3 catalysts. *In-situ* ATR-SEIRAS, *in-situ* SERS, and DFT calculations were combined to track and clarify the whole reaction process from CO_2 to formate. The carbon atoms embedded into the In_2O_3 lattice were able to regulate the electronic structure of In and increased the localization of negative charges on the surface of In_2O_3, resulting in enhanced activity and selectivity simultaneously for CRR to formate. This work gives new light on

developing high-performance CRR catalysts with high selectivity under large current density.

References

[1] M. He, Y. Sun, B. Han, Green carbon science: Efficient carbon resource processing, utilization, and recycling towards carbon neutrality, *Angew. Chem. Int. Ed.*, **2022**, *61*, e202112835.

[2] Q. Song, Z. Zhou, L. He, Efficient, selective and sustainable catalysis of carbon dioxide, *Green Chem.*, **2017**, *19*, 3707-3728.

[3] I. Grigioni, L.K. Sagar, Y.C. Li, G. Lee, Y. Yan, K. Bertens, R.K. Miao, X. Wang, J. Abed, D.H. Won, F.P. García de Arquer, A.H. Ip, D. Sinton, E.H. Sargent, CO_2 electroreduction to formate at a partial current density of 930 mA cm^{-2} with InP colloidal quantum dot derived catalysts, *ACS Energy Lett.*, **2020**, *6*, 79-84.

[4] D. Yang, Q. Zhu, X. Sun, C. Chen, L. Lu, W. Guo, Z. Liu, B. Han, Nanoporous Cu/Ni oxide composites: efficient catalysts for electrochemical reduction of CO_2 in aqueous electrolytes, *Green Chem.*, **2018**, *20*, 3705-3710.

[5] X. Sun, Q. Zhu, X. Kang, H. Liu, Q. Qian, J. Ma, Z. Zhang, G. Yang, B. Han, Design of a Cu(i)/C-doped boron nitride electrocatalyst for efficient conversion of CO_2 into acetic acid, *Green Chem.*, **2017**, *19*, 2086-2091.

[6] X. Wang, D. Wu, X. Kang, J. Zhang, X.-Z. Fu, J.-L. Luo, Densely packed ultrafine SnO_2 nanoparticles grown on carbon cloth for selective CO_2 reduction to formate, *J. Energy Chem.*, **2022**, *71*, 159-166.

[7] K. Mou, Z. Chen, S. Yao, L. Liu, Enhanced electrochemical reduction of carbon dioxide to formate with in-situ grown indium-based catalysts in an aqueous electrolyte, *Electrochim. Acta*, **2018**, *289*, 65-71.

[8] J. Zhang, R. Yin, Q. Shao, T. Zhu, X. Huang, Oxygen Vacancies in Amorphous InO_x Nanoribbons Enhance CO_2 Adsorption and Activation for CO_2 Electroreduction, *Angew. Chem. Int. Ed.*, **2019**, *58*, 5609-5613.

[9] Z. Zhang, F. Ahmad, W. Zhao, W. Yan, W. Zhang, H. Huang, C. Ma, J. Zeng,

Enhanced Electrocatalytic Reduction of CO_2 via Chemical Coupling between Indium Oxide and Reduced Graphene Oxide, *Nano Lett.*, **2019**, *19*, 4029-4034.

[10] Y. Liang, W. Zhou, Y. Shi, C. Liu, B. Zhang, Unveiling in situ evolved In/In_2O_3-heterostructure as the active phase of In_2O_3 toward efficient electroreduction of CO_2 to formate, *Sci. Bull.*, **2020**, *65*, 1547-1554.

[11] W. Yang, Y. Zhao, S. Chen, W. Ren, X. Chen, C. Jia, Z. Su, Y. Wang, C. Zhao, Defective Indium/Indium Oxide Heterostructures for Highly Selective Carbon Dioxide Electrocatalysis, *Inorg. Chem.*, **2020**, *59*, 12437-12444.

[12] Z. Chen, G. Yu, B. Li, X. Zhang, M. Jiao, N. Wang, X. Zhang, L. Liu, *In situ* carbon encapsulation confined nickel-doped indium oxide nanocrystals for boosting CO_2 electroreduction to the industrial level, *ACS Catal.*, **2021**, *11*, 14596-14604.

[13] S. Yan, C. Peng, C. Yang, Y. Chen, J. Zhang, A. Guan, X. Lv, H. Wang, Z. Wang, T.K. Sham, Q. Han, G. Zheng, Electron Localization and Lattice Strain Induced by Surface Lithium Doping Enable Ampere-Level Electrosynthesis of Formate from CO_2, *Angew. Chem. Int. Ed.*, **2021**, *60*, 25741-25745.

[14] W. Wang, H. Ning, Z. Yang, Z. Feng, J. Wang, X. Wang, Q. Mao, W. Wu, Q. Zhao, H. Hu, Y. Song, M. Wu, Interface-induced controllable synthesis of Cu_2O nanocubes for electroreduction CO_2 to C_2H_4, *Electrochim. Acta*, **2019**, *306*, 360-365.

[15] C. Gao, J. Feng, J. Dai, Y. Pan, Y. Zhu, W. Wang, Y. Dong, L. Cao, L. Guan, L. Pan, H. Hu, M. Wu, Manipulation of interlayer spacing and surface charge of carbon nanosheets for robust lithium/sodium storage, *Carbon*, **2019**, *153*, 372-380.

[16] H. Ning, D. Guo, X. Wang, Z. Tan, W. Wang, Z. Yang, L. Li, Q. Zhao, J. Hao, M. Wu, Efficient CO_2 electroreduction over N-doped hieratically porous carbon derived from petroleum pitch, *J. Energy Chem.*, **2021**, *56*, 113-120.

[17] H. Ning, Q. Mao, W. Wang, Z. Yang, X. Wang, Q. Zhao, Y. Song, M. Wu, N-doped reduced graphene oxide supported Cu_2O nanocubes as high active catalyst for CO_2 electroreduction to C_2H_4, *J. Alloys Compd.*, **2019**, *785*, 7-12.

[18] Y. Huang, L.W. Jiang, B.Y. Shi, K.M. Ryan, J.J. Wang, Highly efficient oxygen evolution reaction enabled by phosphorus doping of the Fe electronic structure in iron-

nickel selenide nanosheets, *Adv. Sci.*, **2021**, *8*, e2101775.

[19] S.-Q. Liu, M.-R. Gao, R.-F. Feng, L. Gong, H. Zeng, J.-L. Luo, Electronic delocalization of bismuth oxide induced by sulfur doping for efficient CO_2 electroreduction to formate, *ACS Catal.*, **2021**, *11*, 7604-7612.

[20] H. Ning, W. Wang, Q. Mao, S. Zheng, Z. Yang, Q. Zhao, M. Wu, Catalytic electroreduction of CO_2 to C_2H_4 using Cu_2O supported on 1-Octyl-3-methylimidazole functionalized graphite sheets, *Acta Phys. -Chim. Sin.*, **2018**, *34*, 938-944.

[21] J. Wang, H. Liu, Y. Liu, W. Wang, Q. Sun, X. Wang, X. Zhao, H. Hu, M. Wu, Sulfur bridges between Co_9S_8 nanoparticles and carbon nanotubes enabling robust oxygen electrocatalysis, *Carbon*, **2019**, *144*, 259-268.

[22] Q. Zhao, J. Liu, Y. Wang, W. Tian, J. Liu, J. Zang, H. Ning, C. Yang, M. Wu, Novel in-situ redox synthesis of Fe_3O_4/rGO composites with superior electrochemical performance for lithium-ion batteries, *Electrochim. Acta*, **2018**, *262*, 233-240.

[23] H. Ning, X. Wang, W. Wang, Q. Mao, Z. Yang, Q. Zhao, Y. Song, M. Wu, Cubic Cu_2O on nitrogen-doped carbon shells for electrocatalytic CO_2 reduction to C_2H_4, *Carbon*, **2019**, *146*, 218-223.

[24] J.F. G. Kresse, Efficiency of ab-Initio total energy calculations for metals and semiconductors using a plane-wave basis set, *Comp. Mater. Sci.*, **1996**, *6*, 15-50.

[25] J.F. G. Kresse, Efficient iterative schemes for ab initio total-energy calculations using a plane-wave basis set, *Phys. Rev. B*, **1996**, *54*, 11169-11186.

[26] K.B. John P. Perdew, Matthias Ernzerhof, Generalized gradient approximation made simple, *Phys. Rev. Lett.*, **1996**, *77*, 3865-3868.

[27] D.J. G. Kresse, From ultrasoft pseudopotentials to the projector augmented-wave method, *Phys. Rev. B*, **1999**, *59*, 1758-1775.

[28] P.E. Blochl, Projector augmented-wave method, *Phys. Rev. B*, **1994**, *50*, 17953-17979.

[29] S. Grimme, J. Antony, S. Ehrlich, H. Krieg, A consistent and accurate ab initio parametrization of density functional dispersion correction (DFT-D) for the 94 elements H-Pu, *The Journal of Chemical Physics*, **2010**, *132*, 154104.

[30] G.U. Henkelman, Blas P.; Jonsson, Hannes, Atom-centered symmetry functions for constructing high-dimensional neural network potentials, *The Journal of Chemical Physics*, **2000**, *134*, 074106.

[31] Z. Wang, Y. Zhou, C. Xia, W. Guo, B. You, B.Y. Xia, Efficient Electroconversion of Carbon Dioxide to Formate by a Reconstructed Amino-Functionalized Indium-Organic Framework Electrocatalyst, *Angew. Chem. Int. Ed.*, **2021**, *60*, 19107-19112.

[32] Y. Qi, J. Jiang, X. Liang, S. Ouyang, W. Mi, S. Ning, L. Zhao, J. Ye, Fabrication of black In_2O_3 with dense oxygen vacancy through dual functional carbon doping for enhancing photothermal CO_2 hydrogenation, *Adv. Funct. Mater.*, **2021**, *31*, 2100908.

[33] Z. Wang, Y. Zhou, D. Liu, R. Qi, C. Xia, M. Li, B. You, B.Y. Xia, Carbon-Confined Indium Oxides for Efficient Carbon Dioxide Reduction in a Solid-State Electrolyte Flow Cell, *Angew. Chem. Int. Ed.*, **2022**, *61*, e202200552.

[34] Z. Bitar, A. Fecant, E. Trela-Baudot, S. Chardon-Noblat, D. Pasquier, Electrocatalytic reduction of carbon dioxide on indium coated gas diffusion electrodes-Comparison with indium foil, *Appl. Catal. B: Environ.*, **2016**, *189*, 172-180.

[35] J.L. White, A.B. Bocarsly, Enhanced Carbon Dioxide Reduction Activity on Indium-Based Nanoparticles, *J. Electrochem. Soc.*, **2016**, *163*, H410-H416.

[36] R. Hegner, L.F.M. Rosa, F. Harnisch, Electrochemical CO_2 reduction to formate at indium electrodes with high efficiency and selectivity in pH neutral electrolytes, *Appl. Catal. B: Environ.*, **2018**, *238*, 546-556.

[37] Z.M. Detweiler, J.L. White, S.L. Bernasek, A.B. Bocarsly, Anodized indium metal electrodes for enhanced carbon dioxide reduction in aqueous electrolyte, *Langmuir*, **2014**, *30*, 7593-7600.

[38] Z. Xia, M. Freeman, D. Zhang, B. Yang, L. Lei, Z. Li, Y. Hou, Highly Selective Electrochemical Conversion of CO_2 to HCOOH on Dendritic Indium Foams, *ChemElectroChem*, **2018**, *5*, 253-259.

[39] W. Luo, W. Xie, M. Li, J. Zhang, A. Züttel, 3D hierarchical porous indium catalyst for highly efficient electroreduction of CO_2, *J. Mater. Chem. A*, **2019**, *7*, 4505-4515.

[40] B. Pan, G. Yuan, X. Zhao, N. Han, Y. Huang, K. Feng, C. Cheng, J. Zhong, L.

Zhang, Y. Wang, Y. Li, Highly Dispersed Indium Oxide Nanoparticles Supported on Carbon Nanorods Enabling Efficient Electrochemical CO_2 Reduction, *Small Science*, **2021**, *1*, 2100029.

[41] Z. Wang, R. Qi, D. Liu, X. Zhao, L. Huang, S. Chen, Z. Chen, M. Li, B. You, Y. Pang, B. Yu Xia, Exfoliated Ultrathin $ZnIn_2S_4$ Nanosheets with Abundant Zinc Vacancies for Enhanced CO_2 Electroreduction to Formate, *ChemSusChem*, **2021**, *14*, 852-859.

[42] Z. Yang, H. Wang, X. Fei, W. Wang, Y. Zhao, X. Wang, X. Tan, Q. Zhao, H. Wang, J. Zhu, L. Zhou, H. Ning, M. Wu, MOF derived bimetallic CuBi catalysts with ultra-wide potential window for high-efficient electrochemical reduction of CO_2 to formate, *Appl. Catal. B: Environ.*, **2021**, *298*, 120571.

[43] X. Wang, W. Wang, J. Zhang, H. Wang, Z. Yang, H. Ning, J. Zhu, Y. Zhang, L. Guan, X. Teng, Q. Zhao, M. Wu, Carbon sustained SnO_2-Bi_2O_3 hollow nanofibers as Janus catalyst for high-efficiency CO_2 electroreduction, *Chem. Eng. J.*, **2021**, *426*, 131867.

[44] W. Deng, L. Zhang, L. Li, S. Chen, C. Hu, Z.J. Zhao, T. Wang, J. Gong, Crucial role of surface hydroxyls on the activity and stability in electrochemical CO_2 reduction, *J. Am. Chem. Soc.*, **2019**, *141*, 2911-2915.

[45] M. Ziemba, L. Schumacher, C. Hess, Reduction Behavior of Cubic In_2O_3 Nanoparticles by Combined Multiple *In Situ* Spectroscopy and DFT, *J. Phys. Chem. Lett.*, **2021**, *12*, 3749-3754.

[46] Y. Yang, L. Ohnoutek, S. Ajmal, X. Zheng, Y. Feng, K. Li, T. Wang, Y. Deng, Y. Liu, D. Xu, V.K. Valev, L. Zhang, "Hot edges" in an inverse opal structure enable efficient CO_2 electrochemical reduction and sensitive *in situ* Raman characterization, *J. Mater. Chem. A*, **2019**, *7*, 11836-11846.

[47] W. Wang, Z. Ma, X. Fei, X. Wang, Z. Yang, Y. Wang, J. Zhang, H. Ning, N. Tsubaki, M. Wu, Joint tuning the morphology and oxygen vacancy of Cu_2O by ionic liquid enables high-efficient CO_2 reduction to C_2 products, *Chem. Eng. J.*, **2022**, *436*, 135029.

[48] Y. Shi, Y. Ji, J. Long, Y. Liang, Y. Liu, Y. Yu, J. Xiao, B. Zhang, Unveiling

hydrocerussite as an electrochemically stable active phase for efficient carbon dioxide electroreduction to formate, *Nat. Commun.*, **2020**, *11*, 3415.

Summary

With the large amount of carbon dioxide (CO_2) emission, many climate and environmental problems, such as global warming and ocean acidification, are getting more and more attention, which damage the sustainable development of human society. The CO_2 electroreduction reaction (CRR) is promising from CO_2 into high value-added chemicals or fuels. However, the CRR for practical applications is still limited by its low CO_2 conversion and current density. In this thesis, we concentrated on the innovative design strategies for the CRR system, and systematically considered the various challenges for CRR electrocatalyst. The electrocatalysts were developed for CRR to high value-added products. The reaction mechanism were clarified by *in-situ* analysis and density functional theory (DFT) computations.

Multi-carbon products are more attention due to high value-added, such ethylene and ethanol. However, copper is still the main metal that can effectively catalyze CRR to C_2 products, owing to the specific binding energy of *CO intermediate. In Chapter 1, the quasi-spherical Cu_2O with rough surface and abundant oxygen vacancies were simply prepared by a wet chemical method in assistant with [Omim]Cl assisting. On the one hand, $[Omim]^+$ played a key role as like-surfactant in inhibiting the growth of crystal planes, thus getting a special quasi-spherical morphology of Cu_2O with rough surfaces. On the other hand, due to the hydrogen bonding between $[Omim]^+$ and Cl^-, more Cl^- were adsorbed on the surface of Cu_2O, thus promoting the formation of oxygen vacancies by coordinating with Cu^+. Under the synergistic effects of $[Omim]^+$ and Cl^-, the novel quasi-spherical Cu_2O with abundant oxygen vacancies were prepared and in-situ dispersed on a home-made graphite nanosheets to form a series of Cu_2O/ILGS-*x* composites, which behaved excellent catalytic performance towards CO_2 electroreduction to C_2 products (ethylene and ethanol). By adjusting the content of [Omim]Cl, the optimum catalyst of Cu_2O/ILGS-*400* performed the best performance with a faradic efficiency (FE) of 62.4% for C_2 products at -1.15 V (*vs.* RHE) in an H-cell with 0.1 M $KHCO_3$ as electrolyte. By using 1 M KOH as electrolyte in a flow cell,

the FE of C_2 products was raised to 78.5% ± 2% with current density of 123.1 mA cm^{-2} at −1.1 V (*vs.* RHE). In a long durability test for 100 hours, the catalytic performance of C_2 had no obvious degradation. *In situ* surface-enhanced Raman spectroscopy and DFT computations proved the special structure of Cu_2O strengthened the adsorption of intermediates ($CO_2^{\bullet-}$, CO*) and the following C–C coupling reaction, thus remarkably promoting the formation of C_2 products. This work may open a new horizon towards controllable synthesis of metal oxides using ionic liquids as bifunctional structure-directing agent for CO_2 reduction and other electrocatalysis process.

Formate is an important feedstock chemical due to nontoxicity, safety, and broad applications, which is also a hydrogen carrier for transportation. In Chapter 2, the carburized In_2O_3 nanorods were developed as high-performance catalysts for stable and efficient CO_2 electroreduction to formate. In an H-cell, the In_2O_3-C afforded an excellent FE above 90% toward formate at a wide potential range of 500 mV, while the highest value of FE reaches 97.2% at -1.0 V *vs.* RHE. The excellent performance could be sustained at a high current density of -1 A cm^{-2} with $FE_{formate}$ of 80.5% in a flow cell, outperforming the bare In_2O_3 catalysts. *In-situ* ATR-SEIRAS, *in-situ* SERS, and DFT calculations were combined to track and clarify the whole reaction process from CO_2 to formate. The carbon atoms embedded into the In_2O_3 lattice were able to regulate the electronic structure of In and increased the localization of negative charges on the surface of In_2O_3, resulting in enhanced activity and selectivity simultaneously for CRR to formate. This work gives new light on developing high-performance CRR catalysts with high selectivity under large current density.

We believe that the findings of this thesis provide useful knowledge for designing other efficient electrocatalysts for CRR. At the same time, although realizing the superior selectivity and activity for CRR by a flow cell, the long-term stability is still a challenging issue, which still need to further develop in the future.

List of publications

[1] **Wenhang Wang,** Zhengguang Ma, Xiang Fei, Xiaoshan Wang, ZhongxueYang, Yang Wang, Jinqiang Zhang, Hui Ning, Noritatsu Tsubaki, Mingbo Wu. Joint tuning the morphology and oxygen vacancy of Cu_2O by ionic liquid enables high-efficient CO_2 reduction to C_2 products, *Chemical Engineering Journal*, **2022**, 436, 135029. **(IF = 16.744, Chapter 1)**

[2] **Wenhang Wang,** Xiaoshan Wang, Zhengguang Ma, Yang Wang, Zhongxue Yang, Jiexin Zhu, Lei Lv, Hui Ning, Noritatsu Tsubaki, Mingbo Wu. Carburized In_2O_3 nanorods endow CO_2 electroreduction to formate at 1 A cm^{-2}, *ACS Catalysis*, **2023**, 13, 796-802. **(IF = 13.700, Chapter 2)**

[3] **Wenhang Wang,** Hui Ning, Xiang Fei, Xiaoshan Wang, Zhengguang Ma, Zhenmei Jiao, Yani Wang, Noritatsu Tsubaki, Mingbo Wu. Trace ionic liquid−assisted orientational growth of Cu_2O (110) facets promote CO_2 electroreduction to C_2 products, *ChemSusChem*, **2023**, 16, e202300418. **(IF = 9.140)**

[4] **Wenhang Wang,** Ruosong He, Yang Wang, Meng Li, Jianxin Liu, Jiaming Liang, Shuhei Yasuda, Qiang Liu, Mingbo Wu, Noritatsu Tsubaki. Boosting methanol-mediated CO_2 hydrogenation into aromatics by synergistically tailoring oxygen vacancy and acid site properties of multifunctional catalyst, *Chemistry-A European Journal*, **2023**, 29, e202301135. **(IF = 5.020, Hot paper)**

[5] **Wenhang Wang,** Hui Ning, Zhongxue Yang, Zhaoxuan Feng, Jialin Wang, Xiaoshan Wang, Qinhu Mao, Wenting Wu, Qingshan Zhao, Han Hu, Yan Song, Mingbo Wu. Interface-induced controllable synthesis of Cu_2O nanocubes for electroreduction CO_2 to C_2H_4, *Electrochimica Acta*, **2019**, 306, 360-365. **(IF = 7.336)**

[6] Xu Sun, Jiayuan Wang, Yujia Jiang, Elton Maturura, **Wenhang Wang,** Ruiqin Yang, Chuang Xing, Jiangang Chen, Noritatsu Tsubaki. Facile synthesis of zeolites under an atmospheric reflux system, *Microporous and Mesoporous Materials,* **2022**, 331, 111646. **(IF = 5.876)**

[7] Hui Ning, **Wenhang Wang,** Qinhu Mao, Shirui Zheng, Zhongxue Yang, Qingshan Zhao, Mingbo Wu. Catalytic electroreduction of CO_2 to C_2H_4 using Cu_2O supported on 1-Octyl-3-methylimidazole functionalized graphite sheets, *Acta Physico-Chimica Sinica* **2018**, 34, 938-944. **(IF = 6.253)**

[8] Xiaoshan Wang, **Wenhang Wang,** Jinqiang Zhang, Hongzhi Wang, Zhongxue Yang, Hui Ning, Jiexin Zhu, Yunlong Zhang, Lu Guan, Xiaoling Teng, Qingshan Zhao, Mingbo Wu. Carbon sustained SnO_2-Bi_2O_3 hollow nanofibers as janus catalyst for high-efficiency CO_2 electroreduction, *Chemical Energineering Journal* **2021**, 426, 131867. **(IF = 16.744)**

[9] Hui Ning, Xiaoshan Wang, **Wenhang Wang,** Qinhu Mao, Zhongxue Yang, Qingshan Zhao, Yan Song, Mingbo Wu. Cubic Cu_2O on nitrogen-doped carbon shell for electrocatalytic CO_2 reduction to C_2H_4, *Carbon,* **2019**, 146, 218-223. **(IF = 11.307)**

[10] Hui Ning, Qinhu Mao, **Wenhang Wang,** Zhongxue Yang, Xiaoshan Wang, Qingshan Zhao, Yan Song, Mingbo Wu. N-doped reduced graphene oxide supported Cu_2O nanocubes as high active catalyst for CO_2 electroreduction to C_2H_4, *Journal of Alloys and Compounds,* **2019**, 785, 7-12. **(IF = 6.371)**

[11] Hui Ning, Zhihao Guo, **Wenhang Wang,** Xiaoshan Wang, Zhongxue Yang, Zhengguang Ma, Yangming Tian, Chenghao Wu, Jian Hao, Mingbo Wu. Ammonia etched petroleum pitch-based porous carbon as efficient catalysts for CO_2 electroreduction, *Carbon Letters,* **2022**, 32, 807-814. **(IF = 3.117)**

[12] Xiaoshan Wang, Xiang Fei, Mingwang Wang, **Wenhang Wang,** Zhongxue Yang, Hui Ning, Yunlong Zhang, Li Wang, Xin Jin, Mingbo Wu. Regular hexagonal CuBi nanosheets boost highly efficient CO_2 reduction to HCOOH in a solid-electrolyte cell, *Journal of Materials Chemistry A*, **2022**, 10, 23542-23550. **(IF = 14.511)**

[13] Zhongxue Yang, Hongzhi Wang, Xiang Fei, **Wenhang Wang,** Yuezhu Zhao, Xiaoshan Wang, Xiaojie Tan, Qingshan Zhao, Huaiping Wang, Jiexin Zhu, Liang Zhou, Hui Ning, Mingbo Wu. MOF derived bimetallic CuBi catalysts with ultra-

wide potential window for high-efficient electrochemical reduction of CO_2 to formate, *Applied Catalysis B: Environmental,* **2021**, 298, 120571. **(IF = 24.319)**

[14] Zhonghao Tan, Tingyue Peng, Xiaojie Tan, **Wenhang Wang,** Xiaoshan Wang, Zhongxue Yang, Hui Ning, Qingshan Zhao, Mingbo Wu. Controllable synthesis of leaf-like CuO nanosheets for selective CO_2 electroreduction to ethylene, *ChemElectroChem,* **2020**, 7, 2020-2025. **(IF = 4.782)**

[15] Hui Ning, Xiang Fei, Zhonghao Tan, **Wenhang Wang,** Zhongxue Yang, Mingbo Wu. In situ-fabricated In_2S_3-reduced graphene oxide nanosheet composites for enhanced CO_2 electroreduction to formate, *ACS Applied Nano Materials,* **2022**, 5, 2335-2342. **(IF = 6.140)**

[16] Yangming Tian, Xiang Fei, Hui Ning, **Wenhang Wang,** Xiaojie Tan, Xiaoshan Wang, Zhengguang Ma, Zhihao Guo and Mingbo Wu. Membrane-free electrocatalysis of CO_2 to C_2 on CuO/CeO_2 nanocomposites, *Frontiers in Chemistry,* **2022**, 10, 915759. **(IF = 5.545)**

[17] Dianliang Guo, Xiaoshan Wang, Zhongxue Yang, **Wenhang Wang,** Hui Ning, andMingbo Wu. Thermal driven high crystallinity of bismuth as robust catalyst for CO_2 electroreduction to formate, *ChemistrySelect*, **2021**, 6, 1870-1873. **(IF = 2.307)**

[18] Hui Ning, Dianliang Guo, Xiaoshan Wang, Zhonghao Tan, **Wenhang Wang,** Zhongxue Yang, Linqing Li, Qingshan Zhao, Jian Hao, Mingbo Wu. Efficient CO_2 electroreduction over N-doped hieratically porous carbon derived from petroleum pitch, *Journal of Energy Chemistry*, **2020**, 56, 113-120. **(IF = 13.599)**

[19] Zhinian Cheng, Yang Wang, Daokuan Jin, Jianxin Liu, **Wenghang Wang,** Yongqiang Gua, Wanxin Ni, Zhaoxuan Feng, MingboWu. Petroleum pitch-derived porous carbon as a metal-free catalyst for direct propane dehydrogenation to propylene, *Catalysis Today*, **2023**, 410, 164-174. **(IF = 6.562)**

[20] Zhongxue Yang, Hongzhi Wang, Xinze Bi, Xiaojie Tan, Yuezhu Zhao, **Wenhang Wang,** Yecheng Zou, Huaiping Wang, Hui Ning, Mingbo Wu. Bimetallic In_2O_3/Bi_2O_3 catalysts enable highly selective CO_2 electroreduction to formate

within ultra-broad potential windows, *Energy & Environmental Materials,* 2023, e12508. **(IF = 15.122)**

[21] Xiaoshan Wang, Yuanyuan Pan, Hui Ning, Hongmei Wang, Dianliang Guo, **Wenhang Wang,** Zhongxue Yang, Qingshan Zhao, Bingxing Zhang, Lirong Zheng, Jianling Zhang, Mingbo Wu. Hierarchically micro- and meso-porous Fe-N_4O-doped carbon as robust electrocatalyst for CO_2 reduction, *Applied Catalysis B: Environmental,* **2020**, 266, 118630. **(IF = 24.319)**

List of conferences

[1] **Wenhang Wang,** Guohui Yang, Noritatsu Tsubaki. Direct synthesis of ethanol from syngas and DME via copper-based capsule catalyst, *4th International Conference on Separation Technology*, **2023**, Johor Bahru, Malaysia. **(Oral)**

[2] **Wenhang Wang,** Yingluo He, Guohui Yang, Noritatsu Tsubaki. Electrochemical reduction of CO_2 to multi-carbon products using copper-based catalysts, *52nd Petroleum-Petrochemical Symposium of JPI*, **2022**, Nagano, Japan. **(Oral)**

[3] **Wenhang Wang,** Guohui Yang, Hui Ning, Mingbo Wu, Noritatsu Tsubaki. Electroreduction carbon dioxide to multi-carbon products on ionic liquid assisted abundant oxygen vacancy oxide-derived copper catalysts, *2021 International Chemical Congress of Pacific Basin Societies*, **2021**, Honolulu, America. **(Poster)**

[4] **Wenhang Wang,** Yang Wang, Hui Ning, Noritatsu Tsubaki, Mingbo Wu. Joint Tuning the morphology and oxygen vacancy of Cu_2O by ionic liquid enables high-efficient CO_2 reduction to C_2 products, *18th National Youth Conference on Catalysis*, **2021**, Taiyuan, China. **(Poster)**

Acknowledgments

Upon the completion of this thesis, I am grateful to those who have offered me guidance and help during the course of my study.

First of all, I would like to express my sincere thanks to my supervisor, Professor Noritatsu Tsubaki, as well as his hard work and help for me in my whole process of doctoral. I admire his rigorous academic attitude, generous and kind-hearted mind, and positive and optimistic attitude towards life. My supervisor has set a superior example, which I will learn from all my life. His teaching and encouragement will encourage me to make great efforts and pioneering innovation on the future.

At the same time, I want to express my sincere thanks to Associate Professor Guohui Yang for his help and valuable guidance in my scientific research. His horizon inspired not only my study during the Ph.D., but also future study and life.

My sincere thanks also go to members in Tsubaki lab for offering me a lot of help in my experiment and life. They are Dr. Yingluo He, Dr. Xiaoyu Guo, Dr. Weizhe Gao, Dr. Jie Yao, Dr. Zhao Heng, Dr. Fei Chen, Dr. Xu Sun, Dr. Jiaming Liang, Dr. Yongqiang Gu, Dr. Lijun Zhang, Dr. Yanbing Li, Dr. Caixia Zhu, Dr. Chenwei Wang, Dr. Fan Wang, Dr. Jiaqi Fan, Dr. Shuhei Yasuda, Mr. Haozhe Feng, Mr. Yugo Kawabata, Mr. Yasuharu Kugue, Ms. Hanyao Song, Ms. Hitomi Ito, Ms. Mika Watanabe, Ms. Mayumi Izumi and so on. Meanwhile, I also would like to thank cooperators including Professor Mingbo Wu, Professor Kostya S. Novoselov, Associate Professor Yang Wang, Associate Professor Hui Ning, Associate Professor Xinhua Gao, Dr. Xiangyu Guo and many other teachers and students for their assistance in my study and life.

Finally, thanks to my parents, wife, and daughter for their continued encouragement and spiritual support during my PhD period. I would like to express my sincere thanks to the financial support of the scholarship from China Scholarship Council.